Università
Ca'Foscari
Venezia

Master's Degree
in Sustainable Chemistry
and Technologies

Final Thesis

Synthesis of inorganic optical thermometers based on Cr^{3+} within the pores of mesoporous silica nanoparticles

Supervisors
Prof. Alvise Benedetti
Dr. Michele Back

Graduand
Michele Crozzolin
Matriculation number
848732

Academic Year
2020 / 2021

Index

1. Introduction

1.1 Luminescent systems

Luminescence is the phenomenon of light being emitted by any material after it has been excited by an energy source. Depending on the type of energy supplied by the source, the luminescence is classified in different types: sonoluminescence: (excitation given by an ultrasonic wave), photoluminescence (produced by photon excitation), cathodoluminescence (excitation produced by an electron beam), chemiluminescence (generation of light following a chemical reaction) to name a few [1,2].
Typically, luminescence processes involve a transition between the ground state and an excited state, with the emission of light occurring after the luminescent species return to the ground state. The emission process can take place via fluorescence or phosphorescence: fluorescence is the fast radiative decay from the singlet state to the fundamental state (with typical lifetime of about 10^{-8} s); phosphorescence is, instead, the radiative decay from the triplet state and it is characterized by a longer lifetime (from about 10^{-7} s to minutes and hours in the case of long persistence phosphors).

Luminescent materials are called phosphors and they generally consist of a crystalline host and a luminescence centre called activator, typically a transition or f-block metal.
The configuration coordinate diagram (CCD) is used to describe the luminescent behaviour of these materials. In this model the parabolic curves represent the different energy levels of the luminescent ions and are related to the vibrational motion of the atoms in the lattice (or molecules). The y-axis represents the energy (E) and the x-axis is the coordination coordinate, usually expressed as Q, that represents the oscillating inter-atomic distance Δr.

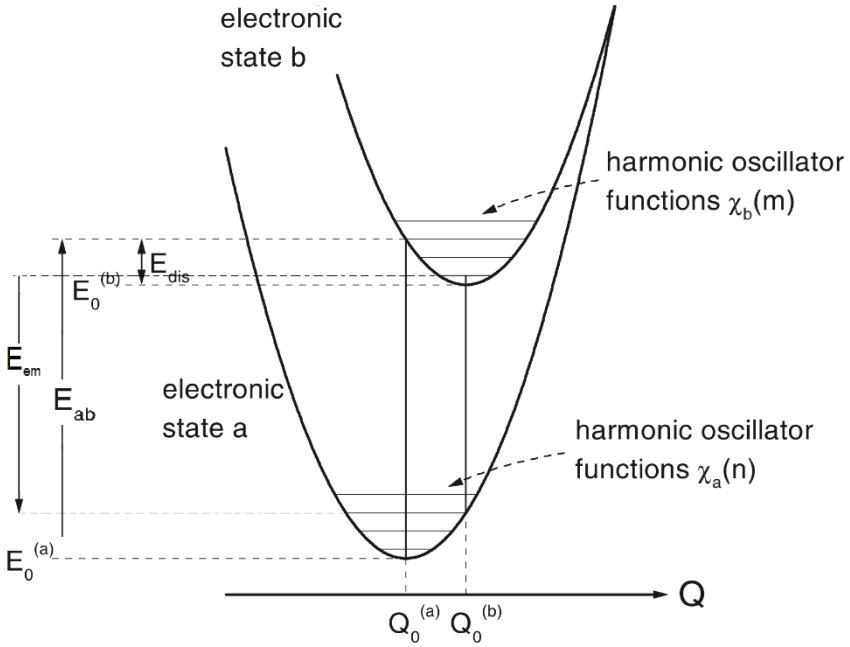

Figure 1.1: A schematic example of a configurational coordinate diagram [3].

This motion, approximated to a harmonic oscillator, is expressed by Hooke's law [4]. CCD emphasizes the dislocation of ions from equilibrium. The rearrangement of the ions during excitation induces small changes in Δr and this value of Δr strongly depends on the size and

charge of the host lattice and the activator [5], so it is used to describe the transition and rearrangement of the luminescence centres. In particular, it is used to describe the effect of temperature on the optical properties of ions.
The concept of Stokes shift can be easily illustrated with the CCD: the Stokes shift is the difference between the position of the maximum of an electronic absorption transition and the corresponding emission. This difference can be expressed in wavelength, wavenumber, frequency or energy. In this thesis the wavenumber difference is adopted as shown in equation (1):

$$Stokes\ shift\ [cm^{-1}] = E_{ex} - E_{em} \qquad (1)$$

As an example, in Figure 1.1 the Stokes shift corresponds to the difference between E_{ab} and E_{em}. When the emitted photon has less energy than the absorbed photon (as in the example shown) it is called Stokes shift; if, on the other hand, the emitted photon has more energy than the absorbed photon, it is called anti-Stokes shift [6].

CCD however is only one of the various models used to describe a luminescent system. Another model widely used for transition metal ions and adopted in our research is the Tanabe Sugano diagram. They are qualitatively useful and can be used to approximate the value of 10*Dq*, the ligand field splitting energy.
In order to characterize the energy levels of the electronic configurations of a metal centre and consequently describe its crystal field, Tanabe-Sugano diagrams can be used. These graphs take into account the parameters introduced by Giulio Racah as a linear combination of Slater's integrals: the Racah parameters *A, B* and *C* [7]. These diagrams were created by Yukito Tanabe and Satoru Sugano starting from their first work "on the absorption spectra of complex ions", showing the energies calculated for the electronic states of each electronic configuration as the intensity of the crystal field varies [8]. With their theory, Tanabe and Sugano were able to quantitatively explain the absorption spectra of octahedral complex ions. [8-9]

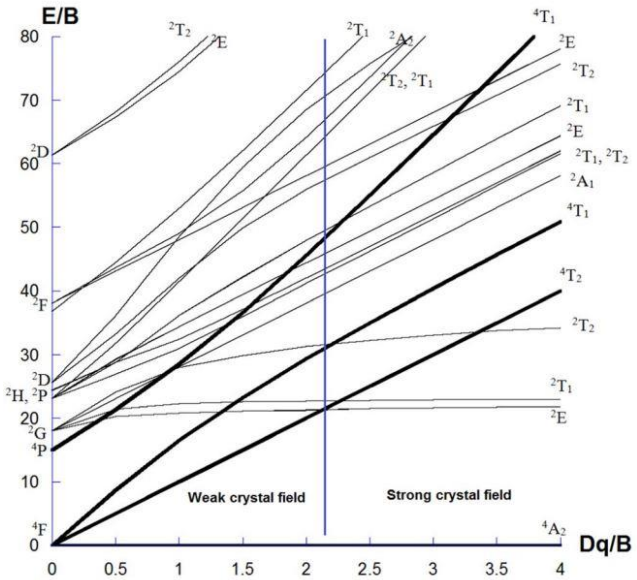

Figure 1.2: A general d^3 transition metal Tanabe-Sugano diagram. [10]

The x-axis of a Tanabe–Sugano diagram is expressed in terms of the ligand field splitting parameter, Δ, or *Dq*, divided by the Racah parameter *B*. The y-axis is in terms of energy, E, also scaled by *B*. Three Racah parameters exist: *A, B*, and *C*, which describe various aspects of interelectronic repulsion. *A* is an average total interelectron repulsion. *B* and *C* correspond with individual d-electron repulsions. *B* is the most important of Racah's parameters for studying d-electron configuration [11]. One line corresponds to each electronic state. Although electronic transitions are only "allowed" if the spin multiplicity remains the same, energy levels for "spin-forbidden" electronic states are included in the diagrams [12]. Each state is given its molecular-symmetry label (e.g. A_{1g}, T_{2g}, etc.), but "g" and "u" subscripts are usually left off because it is understood that all the states are *gerade*. Term symbols (e.g. ^3P, ^1S, etc.) for a specific d^n free ion are listed, in order of increasing energy, on the y-axis of the diagram. The relative order of energies is determined using Hund's rules.

So, thanks to these models, since crystalline structures and optical properties are related and describable, it is possible to extract structural information from optical spectroscopy.

1.2 Cr^{3+}-doped phosphor

Since Maiman [13] created the first ruby-based laser, the interest in chromium optical properties has grown over time, and currently transition metal ions doped luminescent materials have attracted considerable interests for their potential application in a lot of new modern technologies: non-invasive temperature sensors [14-19], high temperature sensors [20,21], tunable solid-state lasers [22], high-pressure calibrants [23]. Their main characteristic of being phosphors with emission band ranges in the near-infrared (NIR) I (650−900 nm) and NIR II (1000−1450 nm) [24-28] regions have led to a great development of research in the fields of bioimaging, photovoltaics, sensors, and so on. Among all these applications, bioimaging has gained much attention, covering a wide observation range from subcellular structures, cells, and tissues to entire multicellular organisms [31-37]. Some of these phosphors show a near-infrared persistent luminescence [38-41]: long persistence luminescence (LPL) is the occurrence of luminescence which can last for several minutes or hours after the stoppage of excitation. Long persistent phosphors (LPPs) have received more attention being interesting in applications such as safety signage, displays, optical energy media, thermal sensors and in-vivo bioimaging [42-47], but especially for the application in-vivo, since their emission lifetime is sufficiently long to permit late time-gated imaging [48-50]. Cr^{3+} is a favourable choice of activation centre in designing NIR phosphors, since it meets the requirement of LPL for in vivo bioimaging; in particular, Cr^{3+}, with $3d^3$ electron configuration, is a suitable active ion for temperature sensing for its highly temperature-sensitive fluorescence lifetime [51-53].
So far, significant efforts have been devoted by several research groups on the synthesis and characterization of various Cr^{3+}-doped host materials [54-57] and among these, gallates have shown excellent NIR luminescence.

Due to the ability of Cr^{3+} to substitute Ga^{3+} in octahedral coordination exhibiting an excellent NIR luminescence, gallates were widely investigated as systems for the development of Cr^{3+}-activated NIR LPP [58-60]. From X-ray diffraction [61], optical [62-64], and EPR [65] data, it is

now well established that the Cr^{3+} ions substitute Ga^{3+} ions in octahedral sites. This knowledge led to the choice of studying the Ga_2O_3:Cr^{3+} system in this thesis.

Cr^{3+} possesses an incompletely filled d shell and it usually exhibits a narrow emission band near 700 nm due to its spin forbidden transition $^2E \rightarrow {}^4A_2$ or a broadband emission (600−1000 nm) due to the spin allowed transition $^4T_2 \rightarrow {}^4A_2$ depending on the crystal field environment of the host [66, 67]. Trivalent chromium is also the most stable oxidation state of chromium, therefore widely used as a luminescent dopant in various materials. Chromium is a low cost activator that can provide deep colour and bright luminescence: the colour of many natural and synthetic gemstones like ruby, emerald, alexandrite, etc., is caused by Cr^{3+} ions. On this account, Cr^{3+} spectroscopy is the subject of numerous investigations [68].

The lowest Cr^{3+} emitting level can be either the $^4T_2$ or the ^2E state, depending on the crystal-field strength (Figure 1.3) [69].

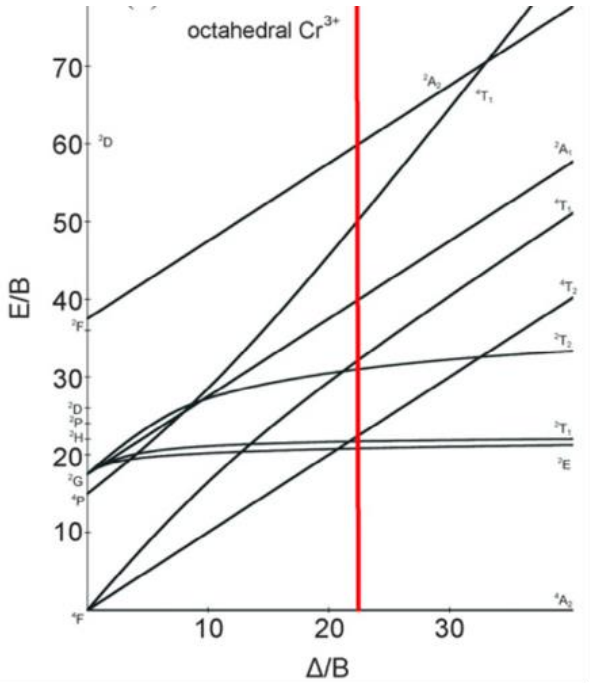

Figure 1.3: Tanabe-Sugano diagram for the $3d^3$ electronic configuration of Cr^{3+} in octahedral symmetry. The red line centred at 22 Δ/B represents an intermediate crystal field strength. [70]

Typical emission features for the weak crystal-field case are a fast decay and broad emission band due to the spin-allowed $^4T_2 \rightarrow {}^4A_2$ transition, which is strongly coupled to the lattice. In contrast, the narrow R-line emission with a long lifetime is associated with the weakly-coupled spin-forbidden $^2E \rightarrow {}^4A_2$ transition as expected in the strong crystal-field regime. An interesting situation arises for intermediate cases, where the crystal-field strength on Cr^{3+} is near the $^4T_2$–^2E excited-state crossover, and the energy separation between the two states is small ($Dq/B \approx 22$). In this case, the $^4T_2$ state interacts with the ^2E state through spin–orbit coupling [71]. Oxide garnets provide intermediate crystal fields around Cr^{3+}, which are close to the $^4T_2$–^2E crossing point, resulting in a strong spin–orbit mixing of the excited states [72].
In order to describe the crystal field acting on the Cr^{3+} ions, in this work the crystal field strength $10Dq$ and the Racah parameters B and C, describing the inter-electron repulsion effects, will be reported. These parameters can be directly estimated from the excitation and emission

bands positions [73]. The 10*Dq* corresponds to the $^4A_2 \rightarrow {}^4T_2$ energy while the Racah parameters *B* and *C* can be estimated as:

$$\frac{B}{Dq} = \frac{\left(\frac{\Delta E_{4T}}{Dq}\right)^2 - 10\left(\frac{\Delta E_{4T}}{Dq}\right)}{15\left(\frac{\Delta E_{4T}}{Dq} - 8\right)} \quad (2)$$

$$C \cong \frac{E(^2E)}{3.05} - \frac{7.9B}{3.05} + \frac{1.8}{3.08}\left(\frac{B^2}{Dq}\right) \quad (3)$$

where $\Delta E_{4T} = E(^4T_1) - E(^4T_2)$.

In the framework of the Tanabe-Sugano theory, a reliable comparison between the energy levels of the excited states of Cr^{3+} in various polymorphs can be done only by calculating the diagrams for the different *C/B* ratio. In fact, the conventional $3d^3$ Tanabe–Sugano diagram was originally calculated for a fixed *C/B* = 4.5, an average value that allows to fairly compare the properties of many Cr^{3+}-activated materials. However, when the *C/B* ratio diverges too much from each other, the comparison between the relative energy level positions for different materials in the same diagram becomes unreliable.

1.3 Cr^{3+} Optical Thermometers

In many biological and technological processes, a fundamental role is played by the temperature.

Ratiometric optical thermometry based on the luminescence intensity ratio (LIR) method has recently emerged as an effective contactless technique characterized by great advantages, such as high spatial resolution and detection sensitivity to rapid response [74-78]. In addition, this method allows to overcome the ambiguity of the optical thermometry based on single emission bands. Therefore, the design of new materials with suitable luminescent properties for this detection method has become a thriving area of research.

Among the wide variety of optical thermometers recently developed, the most reliable ones are still those which are characterized by two excited states in thermal equilibrium (strongly thermodynamically coupled), since they are described by a simple and clear physics such as the Boltzmann distribution and a high reliability is ensured by a rapid population renormalization [75].

In the case of Cr^{3+}-based thermometry, the thermometric parameter LIR can be described as [79]:

$$\frac{I_{4T2}}{I_{2E}} = C * exp\left(\frac{-\Delta E}{kT}\right) \quad (4)$$

With:

I_{4T2}/I_{2E} = LIR of the integrated PL intensities ($^4T_2 \rightarrow {}^4A_2$) / ($^2E \rightarrow {}^4A_2$)

C = probability ratio of the radiative transitions $^4T_2 \rightarrow {}^4A_2$ to $^2E \rightarrow {}^4A_2$

ΔE = activation energy, the energy distance between the $^4T_2$ and ^2E states

k = Boltzmann constant

This same equation is valid for any optical thermometer based on thermally coupled energy levels (Boltzmann thermometers) unless the I_{4T2}/I_{2E} ratio would be substituted with the proper transitions employed.

The possibility of designing position and relative intensity of the sharp $^2E \rightarrow {}^4A_2$ and the broadband $^4T_2 \rightarrow {}^4A_2$ transitions in Cr^{3+}-doped materials have attracted the interest of the scientific community. A critical parameter is played by the energy gap between ^2E and $^4T_2$. In this view, as a first approximation, the control of the energy gap between these two excited states can be achieved through the tuning of the energy level $^4T_2$. In fact, it is strongly dependent on the intensity of the crystal field 10*Dq*, while the level ^2E is practically independent from it, as shown in the Tanabe-Sugano diagram for the $3d^3$ electronic configuration.

The mullite $Bi_2Ga_4O_9:Cr^{3+}$ system was the first non-lanthanide-based material proposed as ratiometric luminescent thermometer characterized by the possibility of both absorbing and emitting in the first optical window of biological tissue [80]. Since then, Cr^{3+}-based systems have been further investigated with the same purpose [79,83-86].

It is known that the electronic states due to the 3d electrons of the outer shell of the transition metal ions are strongly influenced by the nearest environment. To reliably estimate the parameters describing the Cr^{3+} properties (10*Dq*, *B* and *C*) and then to analyze the effect of the crystal field by designing the Tanabe-Sugano diagram, the emission spectra are converted into the energy scale, passing from the photon flux per constant wavelength interval to the photon flux per constant energy interval, according to the conversion formula [87]:

$$\frac{d\varphi(E)}{dE} \propto \frac{d\varphi(\lambda)}{d\lambda}\lambda^2 \qquad (5)$$

Among the Boltzmann thermometers, Cr^{3+}-doped materials are particularly intriguing, combining the flexibility of the relative energy gap between the $^4T_2$–^2E couple with high sensitivities and remarkable thermal resolutions [79,80,84-86]. The thermometric properties of luminescent ratiometric thermometers are influenced by many factors. This is particularly critical in the case of Boltzmann thermometers based on transition metal 3+ ions such as Cr for which the electronic configuration and consequently the relative energy levels of the emitting states $^4T_2$ and ^2E are simultaneously affected by parameters such as the bond lengths, the covalency, and the ionic radii of the substitutional site. The understanding of the role of a single parameter such as the CF in the thermometric properties of Cr^{3+} thermometers is critical to construct a set of guiding principles to explain and predict the performance of this class of materials.

To the best of our knowledge, no attempts have been made so far to investigate the properties of $Ga_2O_3:Cr^{3+}$ of different nanometric sizes. With this aim, we chose to exploit mesoporous silica nanoparticles as nano/micro-reactors, using their pores to confine the oxide nanoparticles (NPs) inside them.

1.4 Mesoporous Silica Nanoparticles (MSNs)

Since the first reports about the synthesis of silica nanoparticles (SNs) by Stöber [88], many new and different synthetic strategies have been developed to prepare SNs of different and tunable morphologies, sizes and properties (Figure 1.4a). Among them, mesoporous silica nanoparticles (MSNs) have been intensively studied for their excellent physical and chemical properties, such as high surface area, tunable pore size, large pore volume and high biocompatibility [89, 90]. Thanks to these great features, MSNs have found a wide range of practical applications in biomedicine [91, 92], catalysis [93] and absorption of pollutants [94] or to protect, grow and transport nanoparticles [95].

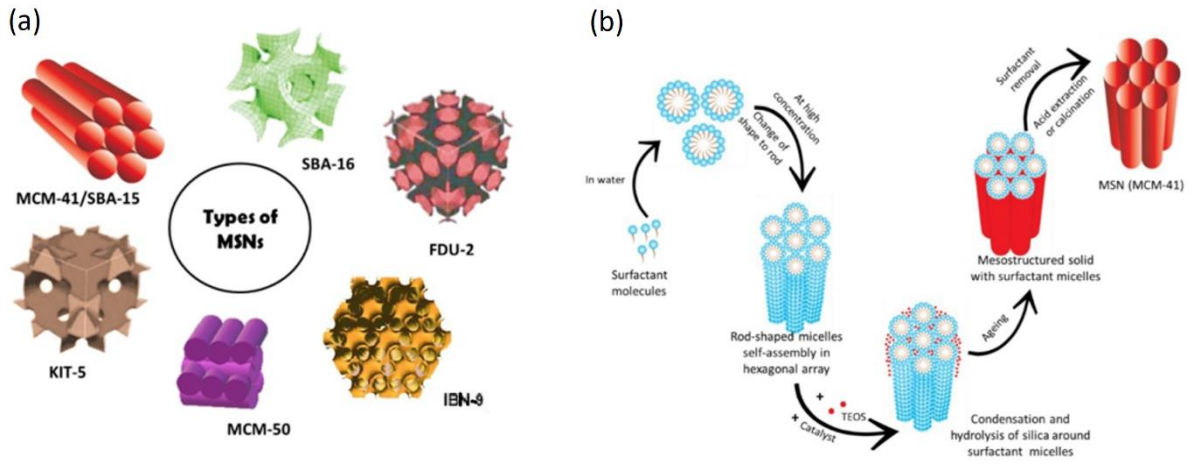

Figure 1.4: (a) Different types of mesoporous silica. (b) Steps for the synthesis of mesoporous silica (MCM-41 type): (i) micelles formation in water solution, (ii) micelles organisation, (iii) TEOS aggregation on the micelles with the help of a catalyst which (iv) after an aging period creates a shell around the surfactant, (v) the surfactant agent is eliminated through calcination or reaction with a solvent [96].

In the first synthetic method to prepare SNs introduced by Stöber in 1968 [88], a silica precursor (tetraethyl orthosilicate, TEOS) hydrolysed in a water-alcoholic solution with ammonia as catalyst. Nowadays, the Stöber modified methods, also known as the sol-gel methods, are the most used [96].

The major breakthrough in the synthesis of MSNs was made by Grün *et al.* in the '90s, adding to the Stöber synthesis a cationic surfactant [97]. The Grün synthesis has led to spherical MSNs named MCM-41 characterized by hexagonal pore symmetry.

Most of the synthetic strategies to grow MSNs based on the sol-gel method, can be described in three steps:

1) Micelles organization of surfactant agents added to a water-alcoholic solution.
2) Addition of a silica precursor (typically TEOS) along with a catalyst to promote the hydrolysis and condensation of silica around the micelles.
3) Elimination of the surfactant agent through calcination or reaction with a solvent.

The catalyst could be acidic or basic, but usually the basic ones are preferred giving higher reaction rates [98]. An example of this synthetic path is reported on Figure 1.4b.

The isoelectric point (IEP) of silica plays an important role in controlling the condensation rate. At pH below the isoelectric point of silica (IEP = 2.0), the silica species are positively charged and the charge density increases as the pH decreases. When the pH is above silica's IEP, the silica species become negative, and the charge density of the negatively charged silica species increases along with the pH [99].

The three basic steps for the synthesis of mesoporous silica can be modified to obtain particles of different size, structure, and a wide range of pores morphologies.
The characteristics of the MSNs can be widely tuned and controlled by modulating the quantity of alcohol or of the catalyst, changing TEOS concentration, changing surfactant agent or modifying the reaction time [100].
Surfactant agents can be non-ionic, cationic and anionic. The non-ionic surfactants are used especially in acidic conditions and they are usually alkyl-polyethylene oxides [101]. Concerning cationic surfactants, the most common are cetyl-trimethylammonium bromide and chloride [97] (CTAB and CTAC) but there are also fluorocarbon surfactants. Examples of anionic surfactants [102] are palmitic acid, oleic acid and N-palmitoyl-alanine and they work with co-structure directing agents such as 3-aminopropyl-triethoxysilane. Non surfactant molecules such as tannic acid were also used as template [103].
Finally, many synthetic routes use non-ionic triblock copolymers as template, mesostructural directing agent or steric stabilizer. The most common are Pluronic triblock copolymers with a different hydrophobicity (EO/PO ratio) and a general formula EOxPOyEOx (EO = ethylene oxide and PO = propylene oxide) [99][104]. The amphiphilic nature induces the formation of micelles in water, therefore, these polymers substitute surfactant agents to obtain nanoparticles with larger pores [104-106].

For the aim of this thesis, three specific kinds of MSNs were synthesized.

MCM-41 NPs.

Grün *et al.* [97] firstly introduced the modification of the Stöber process to create MSNs, obtaining the well-known MCM-41 NPs. Grün synthesis is also known as modified Stöber synthesis, because it consists in the addition of the surfactant to the original procedure. A schematic representation of the synthetic path can be seen on Figure 1.4b. In water the surfactants create micelles which, at high concentration, are organized in rods. Then TEOS condenses on the micelles and hydrolyses, with ammonia as catalyst. The so obtained nanoparticles are spherical and with worm-like pores.

Qiao et al. variation of MCM-41 NPs.

Qiao *et al.* [98] tested the effect of many parameters on particles size and morphology. For example, if the ammonia or basic inorganic salt is too high compared to TEOS, particles will not be spherical but elongated. The MSNs synthesis followed for this thesis led to small, spherical particles with narrow pore distribution, but without the characteristic MCM-41 feature of 2D hexagonal symmetry.

SBA-15 NPs.

Another type of MSNs widely used is the so-called SBA-15 [105]. These NPs are synthesized by means of a triblock copolymer (EO_x-PO_y-EO_x) and sometimes a swelling agent to better control the pore size. The reaction proceeds in an acidic solution pH<1, with the addition of the silica precursor. The as synthetized particles are characterized by bigger pores then the MCM-41 but with the same 2D hexagonal symmetry. The particle size, shape and the pore dimensions can be controlled in many ways: using different copolymers or changing their

concentration, adding cosolvent or also changing the reaction conditions such as temperatures and reaction rates.

Silica has been generally recognized as safe by the FDA, Food and Drug Administration, therefore it can be used for biomedical purposes: it is compatible with biological structures, not causing damage to the growth or development of cells. In addition to this, the siliceous structures are very versatile, in fact they are able to integrate in their matrix different functionalizations or nanomaterials even very different from each other, thus obtaining lab-on-the-particle systems.
These two characteristics led to the idea of studying the synthesis of the $Ga_2O_3:Cr^{3+}$ system in nanometric dimensions inside the mesopores: obtaining an optical thermometer dimensionally confined in the silica gives the possibility to insert it safely between cells of tissues and carry out temperature studies. Optical thermometers would remain active in the first optical window (650-900 nm) of biological systems without suffering interference from silica.

1.5 Gallium oxide polymorphism

Gallium oxide (Ga_2O_3) is a semiconductor that can adopt different crystallographic structures, existing in six different polymorphs: the stable β-phase and four metastable phases α, γ, δ and ε. A further κ transient phase was observed following the oxidation of metallic Ga without ever being able to isolate it [107]. This system has been attracting attention for years for its optoelectronic [108, 109], mechanical [110, 111], and catalytic properties [112, 113].
Up to now many different ways of synthesis have been investigated, demonstrating that even small variations on the reaction parameters, methods and precursors can determine changes on the stabilized phase. Two distinct schemes (Figure 1.5 and Figure 1.6) are reported below which summarize some synthetic routes studied.

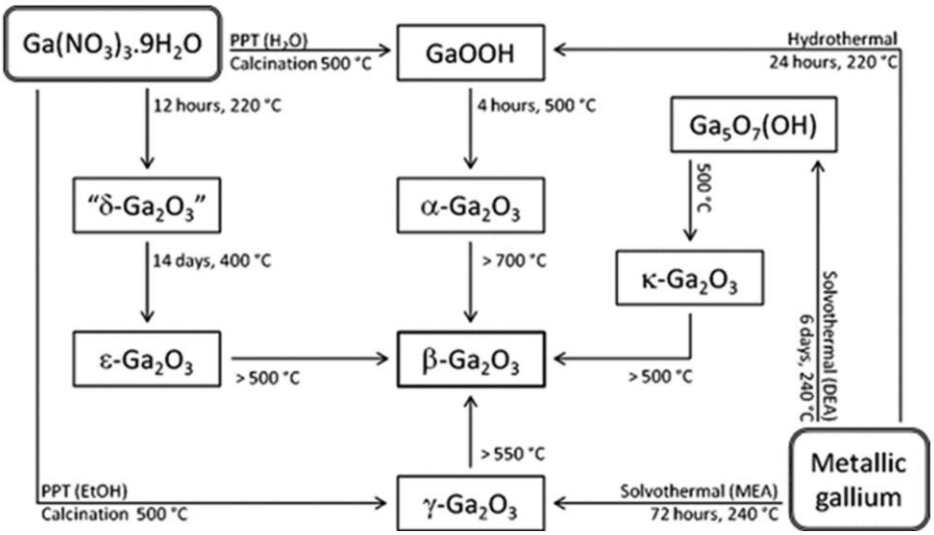

Figure 1.5: Summary of the synthesis and interconversion of the polymorphs of Ga2O3 (PPT ¼ precipitate, DEA ¼ diethanolamine and MEA ¼ monoethanolamine). [114-A]

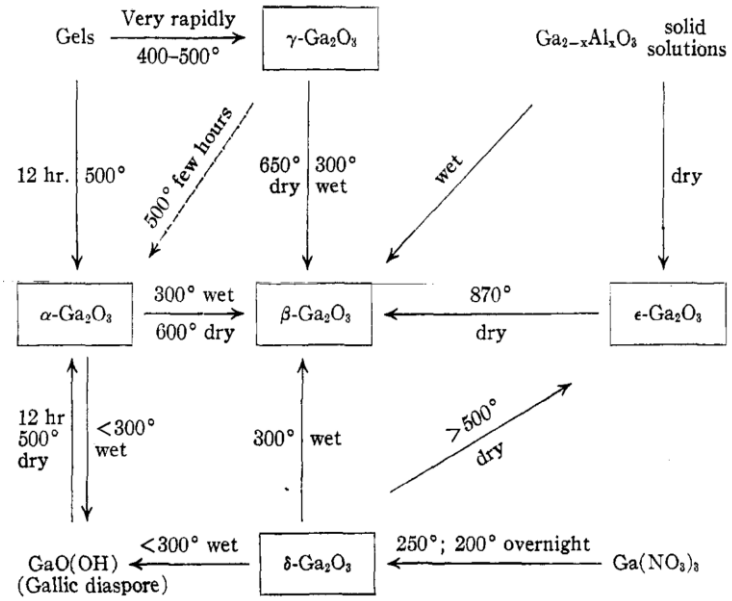

Figure 1.6: Chart illustrating transformation relationships among the forms of gallia and its hydrates. [115]

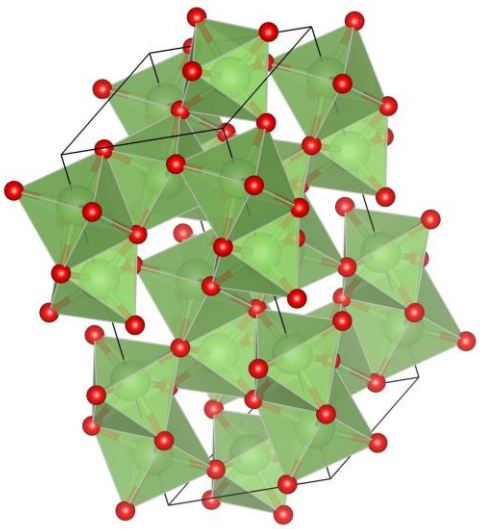

Figure 1.7: α-phase unit cell. This polymorph has only one octahedral coordination site. [116]

The trigonal α-phase [117, 118] is a semiconductor with a band gap of about 5.6 eV [119] easily obtainable by heat treatment from the precursor GaOOH [114-A, 115, 117, 118]. The mean values of the bond distances <Ga-O> for the octahedral site of α-phase, is 1.999 Å (ICSD #27431).

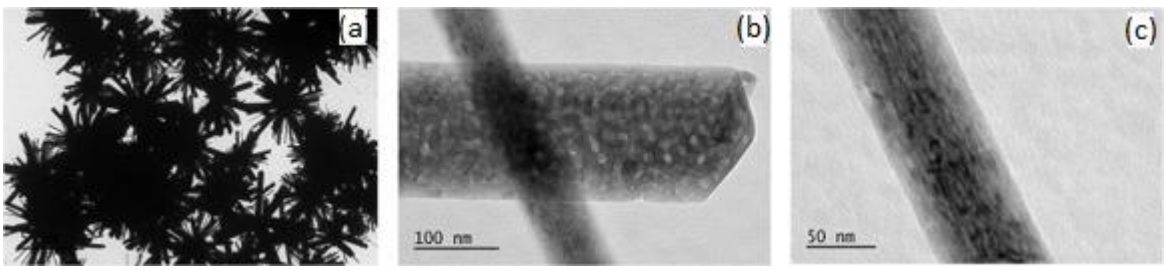

Figure 1.8 (a), (b) and (c): TEM images of α-Ga_2O_3 microcrystals obtained by calcination of α-GaOOH microcrystals. [117]

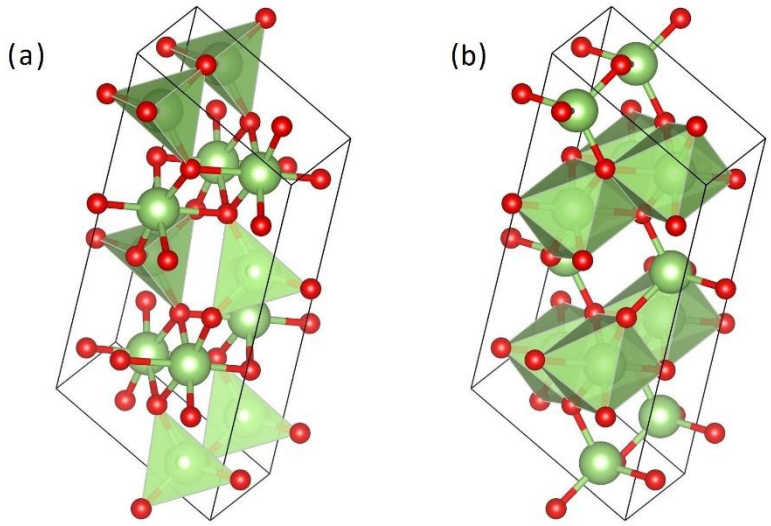

Figure 1.9: β-phase unit cell. (a) Tetrahedral site and (b) Octahedral site. [116]

The β-phase is universally considered the most thermodynamically stable phase. All other phases converge to this through calcination [107]. β-phase belongs to the monoclinic system, in which Ga^{3+} occupies distorted tetrahedral sites and octahedral sites (Figure 1.9) [120]. The mean values of the bond distances <Ga-O> for the octahedral site of β-phase, is 2.012 Å (ICSD #83645).

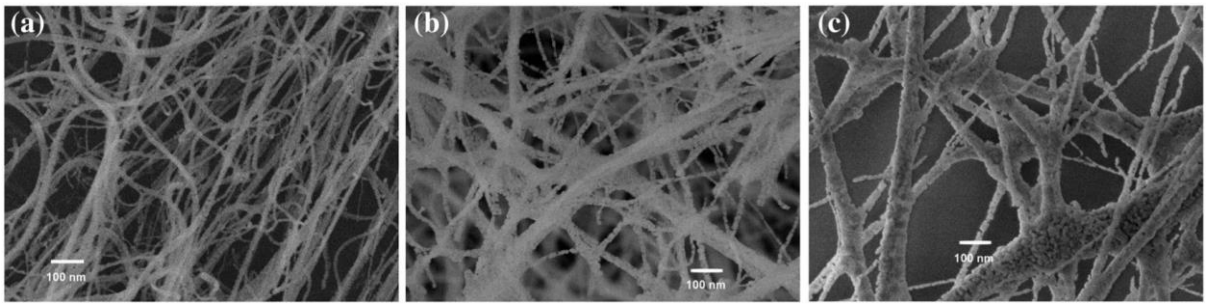

Figure 1.10: FEG-SEM images of the nanofibers synthesized at 1°C/min (a), 5°C/min (b), 10°C/min (c) and subsequently calcined at 900°C. [120]

Large β-phase single crystals can be synthesized by bulk methods such as the floating zone and edge-defined film-fed growth [121].

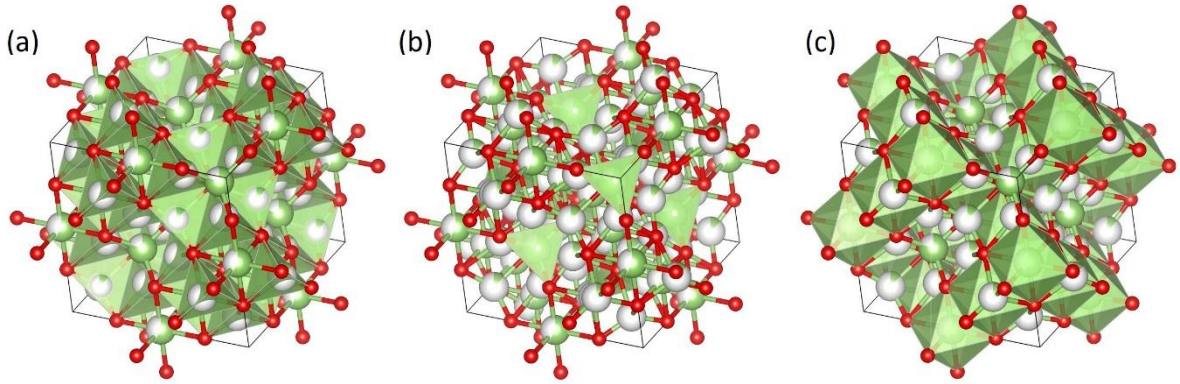

Figure 1.11: γ-phase unit cell. (a) and (b) tetrahedral sites; (c) octahedral site [116].

γ-phase belongs to the cubic system and is easily obtainable via a colloidal synthesis route. The cations occupy tetrahedral and octahedral sites in a ratio $Ga^{3+}(T_d)/Ga^{3+}(O_h) \approx 0,6$ [122].

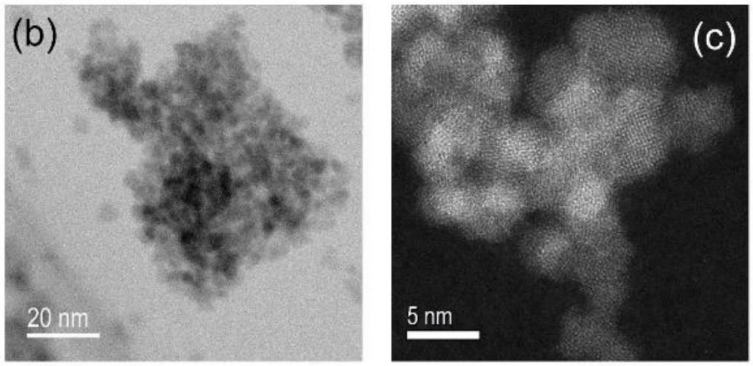

Figure 1.12 (b) and (c): HR-TEM images of γ-Ga_2O_3 obtained from Acetylacetonate Precursors via Solvothermal Synthesis [123]

In a metastable colloidal system, nanocrystals are luminescent in the near-UV and in the blue spectral range, with a luminescence adjustable through the control of the dimensions [122] and a quantum yield of 23%.
The dimensions of the nanocrystals increase with increasing synthesis temperature [124]. The mean values of the bond distances <Ga-O> for the octahedral site of γ-phase, is 2.060 Å (ICSD #152085).

δ-phase belongs to the cubic system. First reported by Roy et al. [115], was recently suggested to be a mixture of ε and β phases [114-A].
Penner et al. [107] stabilized δ-phase nanocrystals by prolonged heating of $Ga(NO_3)_3 \cdot xH_2O$ at 493 K for 12 hours in air.

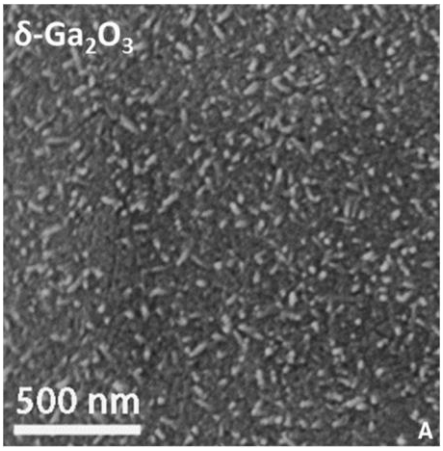

Figure 1.13: SEM image of δ-Ga_2O_3 nanocrystals synthesized with the method described by Penner et al. [107].

ε-phase is one of the least discovered polymorphs.
Penner et al. [107], following a dedicated study, give it a hexagonal structure; Zinkevich et al. [118], instead, suggest a trigonal structure.

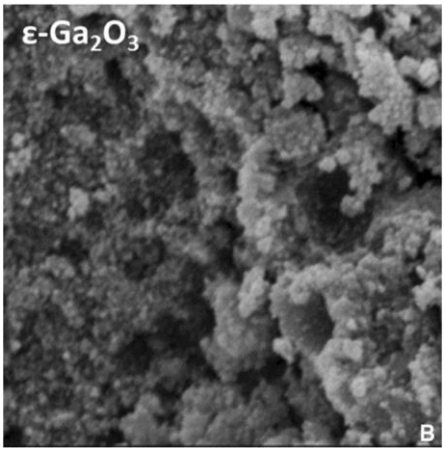

Figure 1.14: SEM image of ε-Ga_2O_3 nanocrystals synthesized with the method described by Penner et al. [107].

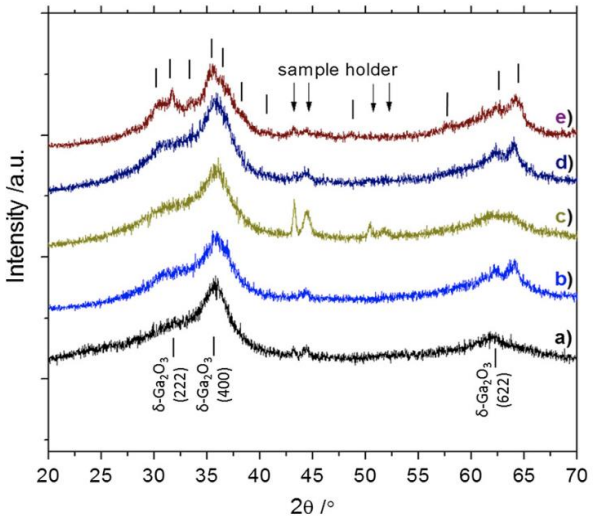

Figure 1.15: X-ray diffractograms following the various heat treatments of the precursor $Ga(NO_3)_3 \cdot xH_2O$ in air and hydrogen, from δ-phase (a) to ε-phase (e), in which the peaks include those of the β-phase [107].

Despite the difficulties in identifying this phase, all the studies in which it was observed claim to have obtained it by annealing the δ-phase at temperatures higher than 773 K.
A humid environment appears to play an important role in the formation of the ε-phase.
Penner et al. [107] also report a synthesis in the form of nanorod via microwave-assisted synthesis with urea, L-cysteine and EDTA as additives.

1.6 Gallium oxide-aluminium oxide systems

Aluminium is the element n° 13 of the periodic table, immediately above gallium in group 13. This proximity makes the two elements similar and among the aspects in common they have the ability to form the oxide of the same brute formula Ga_2O_3 and Al_2O_3. Alumina has, unlike gallia, seven different allotropic forms [125], studied in depth for years, among which corundum, sapphire (whose colour is due to the impurities of Fe^{2+} and Ti^{4+}) and ruby, in which the chromium impurities replace the octahedral aluminium in the lattice.
There are still controversial reports on the solubility and polymorphs in Al_2O_3-Ga_2O_3 solid solution [126-128] due to the lack of understanding of the phase competition in the alloying process. The most stable crystal structures of Ga_2O_3 and Al_2O_3 are respectively the monoclinic (β-Ga_2O_3) and corundum (α- Al_2O_3) and their alloying process is always heterostructural [129].

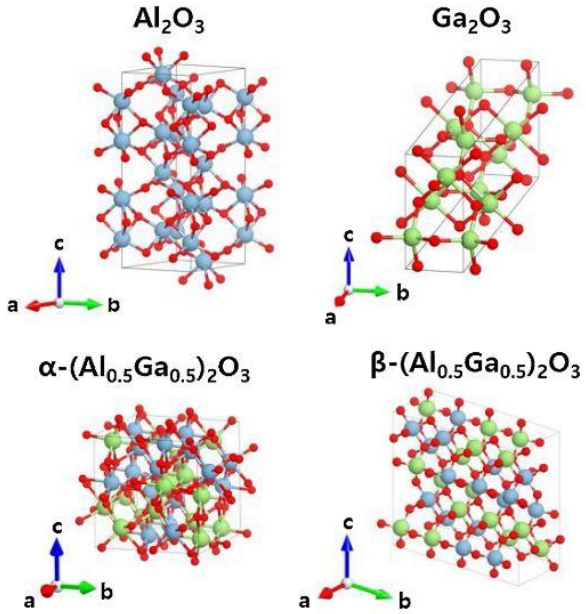

Figure 1.16: Atomic structures of Al_2O_3 for corundum, Ga_2O_3 for monoclinic, and $(Al_{0.5}Ga_{0.5})_2O_3$ for both structures [129].

1.7 Aim of the thesis

The purpose of this thesis is to investigate and describe the effects of quantum confinement on the Ga_2O_3:Cr^{3+} system, with the aim of evaluating its luminescent properties for the purpose of creating ratiometric optical thermometers or chromophores. With this aim, the effect on the crystal field by chromium concentration, temperature of the thermal treatment and particles size, were studied through photoluminescence measurements, X-ray powder diffraction and SEM observations.
In addition, the ability to replace gallium with aluminium and the effects of this substitution are investigated, following the confirmation of the stabilization conditions for the γ-phase of Ga_2O_3.

2. Experimental section

2.1 Materials and methods

2.1.1 Synthesis of MSNs

Different kinds of MSNs were prepared to obtain a set of particles with different pore sizes to be used as reactors. The samples are labelled as MSN_X, where X represents the average pore size.

MSN_3.1. For the first type of MSNs, the procedure described by Back *et al.* [81] was followed on the basis of the original studies reported by Quiao *et al.* [98]. In this work they are labeled as MSN_3.1. These MSNs were synthesized in a flask thermostated at 60°C using an ionic surfactant for the formation of micelles. 145.2 ml of milliQ water, 5.73 g of cetyltrimethylammonium bromide (CTABr) and 22.8 ml of ethanol are dissolved under vigorous stirring; then 1.25 ml of ammonium hydroxide are added. After about 30 minutes of waiting, 14.6 ml of tetraethoxysilane (TEOS) are added with sustained dripping, then all is left to react for two hours, always with vigorous stirring. Once the synthesis is completed, the MSNs undergo centrifugal deposition cycles at 9000 rpm, elimination of solvent, washing and redispersion by ultrasound in milliQ water until total neutralization of pH. The last washing is carried out in ethanol. After washing, they are placed in an oven at 60°C overnight to evaporate all the solvent, then they are ground in a mortar and calcined at 550°C, with a rate of 2°C/min for 6 hours.

MSN_4.2. To create MSNs with pores a little larger than MSN_3.1, the procedure described by Ma et al. [130] was followed. In this work they are labeled as MSN_4.2. After solubilization of 0.8 g of CTABr and 3 ml of NaOH 2M in 400 ml of MilliQ water at room temperature, 60 ml of the swelling agent n-hexane was added. After 15 minutes of stirring, the mixture was stopped; then, 4 ml of TEOS were added after separation of phases. The mixture was stirred again for 5 hours, filtered, washed several times with MeOH and dried at 60°C overnight. MSNs were then ground in a mortar and calcined at 550°C, with a rate of 2°C/min for 5 hours.

MSN_7.5/13.5/22.4. All subsequent silica particles, with progressively larger pore sizes and the characteristic of a two-dimensional *p6mm* hexagonal structure, with a well-ordered hexagonal array and one-dimensional channel structure, were synthesized following the procedures described in Zhao et al. [105] [131] and Cao [132]. In this work, this kind of MSNs synthesized without swelling agent are labeled as MSN_7.5. This synthesis was carried out in a 250 ml jacketed flask thermostat at 35°C. The preparation takes place by placing 4 g of Pluronic P123 block copolymer (polyethylene oxide (EO) - polypropylene oxide (PO) - polyethylene oxide (EO) of formula $EO_{20}PO_{70}EO_{20}$) in the reaction environment together with 30 ml of milliQ water and 116.5 ml of HCl 2M. The copolymer was first dissolved under vigorous stirring at room temperature. After dissolution, the temperature was stabilized at 35°C. At this point, for MSN_13.5 and MSN_22.4, the swelling agent trimethylbenzene (TMB) was added in 0.3:1 (MSN_13.5) and 0.5:1 (MSN_22.4) w/w rate. After 30 minutes, 9 ml of TEOS were added with sustained dripping; then the whole mixture was left to react for 20 hours, always under vigorous stirring. The suspension was then placed in hermetically sealed Teflon containers in autoclaves for an aging process in oven at 100°C for 24 hours. After cooling to

room temperature, the MSNs are washed with deionized water until the pH is neutralized. The last washing is carried out in ethanol. They are then placed in oven at 100°C for 6 hours in order to evaporate all the solvent and then calcined in a muffle at 550°C with a ramp of 2°C/min for 6 hours.

2.1.2 Impregnation method

The precipitation of $Ga_2O_3:Cr^{3+}$ NPs into the MSN mesopores was conducted by incipient wetness impregnation at room temperature. The bare MSNs were dispersed in H_2O, keeping the mixture under stirring. After 30 minutes, the aqueous solutions (0.2 M for gallium and aluminium, 0.05 M for chromium) of the precursor nitrate salts, were added to the dispersion with continuous stirring for 2 h. The powder was recovered through the removal of the solvent by means of a rotary evaporator and treated at the selected temperatures for 4 h, with a heating rate of 3°C/min.

2.1.3 Silica etching

Silica etching was performed by placing the samples under stirring in a 2M NaOH solution for 2 h, following the reaction $2NaOH + SiO_2 \rightarrow Na_2SiO_3 + H_2O$. After precipitation, the solvent was eliminated and the $Ga_2O_3:Cr^{3+}$ NPs dried at 60°C overnight.

2.1.4 Chemical reagents

Reagent	Formula	Supplier
Chromium nitrate nonahydrate (99%)	$Cr(NO_3)_3 * 9H_2O$	Sigma-Aldrich
Aluminium nitrate nonahydrate (≥98%)	$Al(NO_3)_3 * 9H_2O$	Fluka
Gallium nitrate hydrate (98.9%)	$Ga(NO_3)_3 * xH_2O$	Alfa Aesar
Cetyltrimethylammonium bromide (≥98%)	$C_{16}H_{33}N(CH_3)_3Br$	Aldrich
Ethanol (≥99.97%)	EtOH	Sigma-Aldrich
Methanol (≥99.9%)	MeOH	Sigma-Aldrich
Ammonium hydroxide (28-30%)	NH_4OH	Applichem
Tetraethyl orthosilicate (98%)	$Si(OC_2H_5)_4$	Aldrich
n-hexane (≥99%)	C_6H_{12}	Aldrich
Pluronic P-123	$EO_{20}PO_{70}EO_{20}$	Aldrich
1,3,5-trimethylbenzene (98%)	C_9H_{12}	Sigma-Aldrich
Sodium hydroxide (98%)	NaOH	Applichem

2.2 Characterizations

2.2.1 BET/BJH analysis

Nitrogen adsorption–desorption isotherms were measured at liquid nitrogen temperature using a Micrometrics ASAP 2010 system. Each sample was degassed at 130°C overnight before the measurements. The Brunauer–Emmett–Teller (BET) equation was used to calculate the specific surface area from the adsorption data and the Barrett–Joyner–Halenda (BJH) model was used to estimate the pore-size distribution from the adsorption branches of the isotherms.

2.2.2 X-ray Diffraction Powder (XRPD) analysis

XRPD measurements were performed by means of a Philips diffractometer with a PW 1319 goniometer with Bragg–Brentano geometry, equipped with a focusing graphite monochromator and a proportional counter with a pulse-height discriminator. Nickel-filtered Cu Kα radiation and a step-by-step technique were employed (steps of 0.05° in 2θ), with a collection time of 30s per step.

2.2.3 Photoluminescence (PL) and photoluminescence excitation (PLE) analysis

PL emission and PLE excitation spectra were carried out using a Horiba-Jobin Yvon Fluorolog 3–21 spectrofluorometer. The photoluminescence spectra were collected by exciting the samples by means of a xenon arc lamp (450 W), selecting the excitation wavelength using a double Czerny–Turner monochromator. All spectra were recorded at RT under the same conditions.

2.2.4 Morphology SEM images

Size and morphology determination of the nanoparticles and EDS analysis were carried out with a Carl Zeiss Sigma VP Field Emission Scanning Electron Microscope (FE-SEM) equipped with a Bruker Quantax 200 microanalysis detector. The EDS spectra were recorded under the same conditions (20 keV) for all the samples.

3. Results and discussions

3.1 Synthesis of mesoporous silica nanoparticles

With the aim to create the nano/micro-reactors within which synthesizing Ga_2O_3 nanoparticles, MSNs with different pore size were synthesized. To obtain different pore sizes, we explored different types of MSNs. Their characteristics were investigated by means of BET/BJH and SEM analysis.

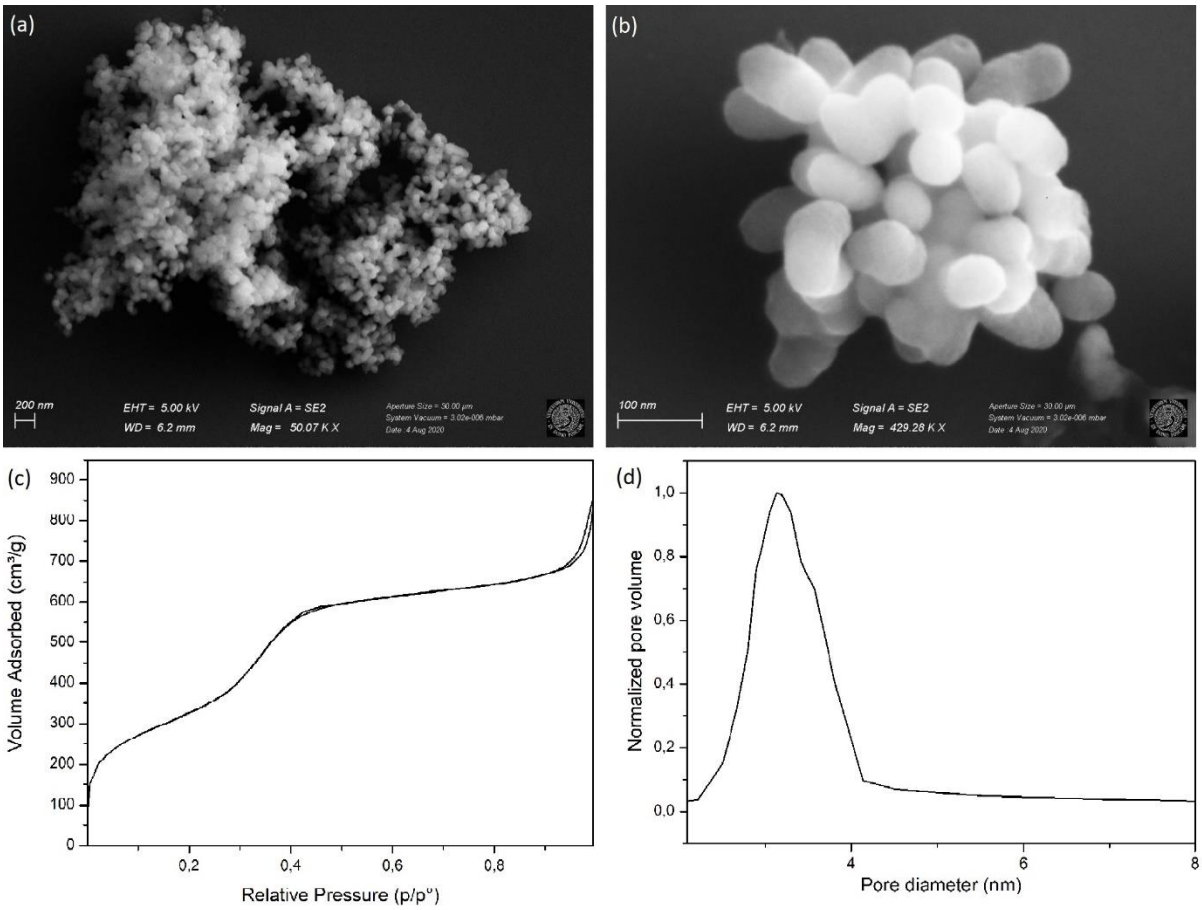

Figures 3.1: (a) and (b) SEM images of MSN_3.1; (c) BET isotherm linear plot of MSN_3.1; (d) MSN_3.1 pore distribution graph.

In Figure 3.1 the SEM images, the BET isotherm linear plot and the pore distribution graph of the first sample MCM-41-type MSNs, labelled MSN_3.1, are reported.
According to the IUPAC classification [136], the mesoporosity of the MSNs, assessed by N_2 adsorption/desorption measurements, follows an isothermal curve with a typical IV profile (Figure 3.1 (c)). From BET/BJH analysis they showed the highest surface area, of about 1236 m^2/g, and a pore volume of 1.035 cm^3/g. Figure 3.1 (d) shows a very narrow pore size distribution centred at 3.1 nm. These MSNs represent the smallest pore size nano-reactors.

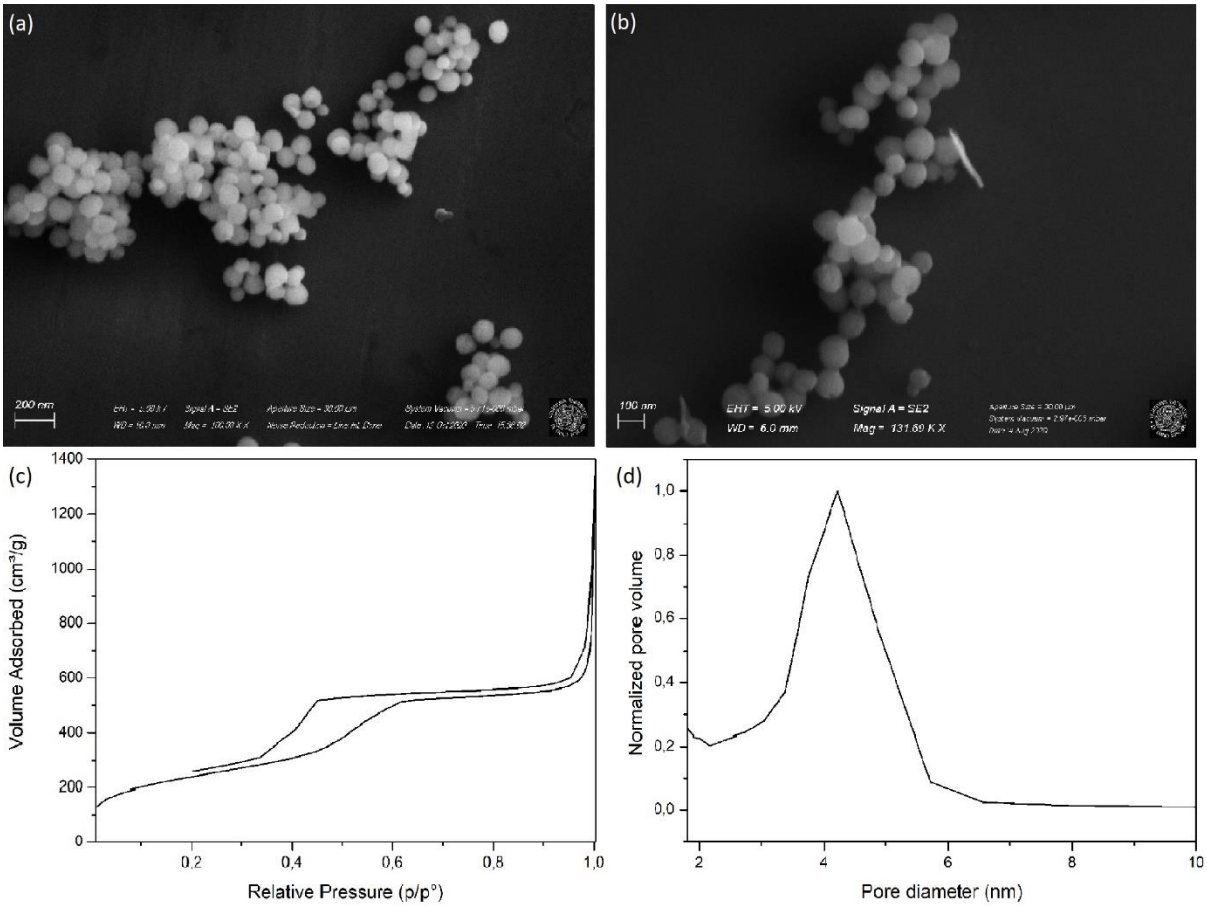

Figures 3.2: (a) and (b) SEM images of MSN_4.2; (c) BET isotherm linear plot of MSN_4.2; (d) MSN_4.2 pore distribution graph.

Figure 3.2 summarized the SEM images, the BET isotherm linear plot and the pore distribution graph of the second sample MCM-41-type MSNs, labelled MSN_4.2.
This sample still follows an isothermal curve with a typical IV profile with a H_2 hysteresis loop due to the capillary condensation steps typical of ordered and mesoporous materials with two-dimensional cylindrical pores. From BET/BJH analysis they showed a surface area of about 853 m^2/g, and a pore volume of 0.955 cm^3/g. The plot showing the diameter pore size distribution (Figure 3.2 (d)) shows a narrow size distribution centred at 4.2 nm.

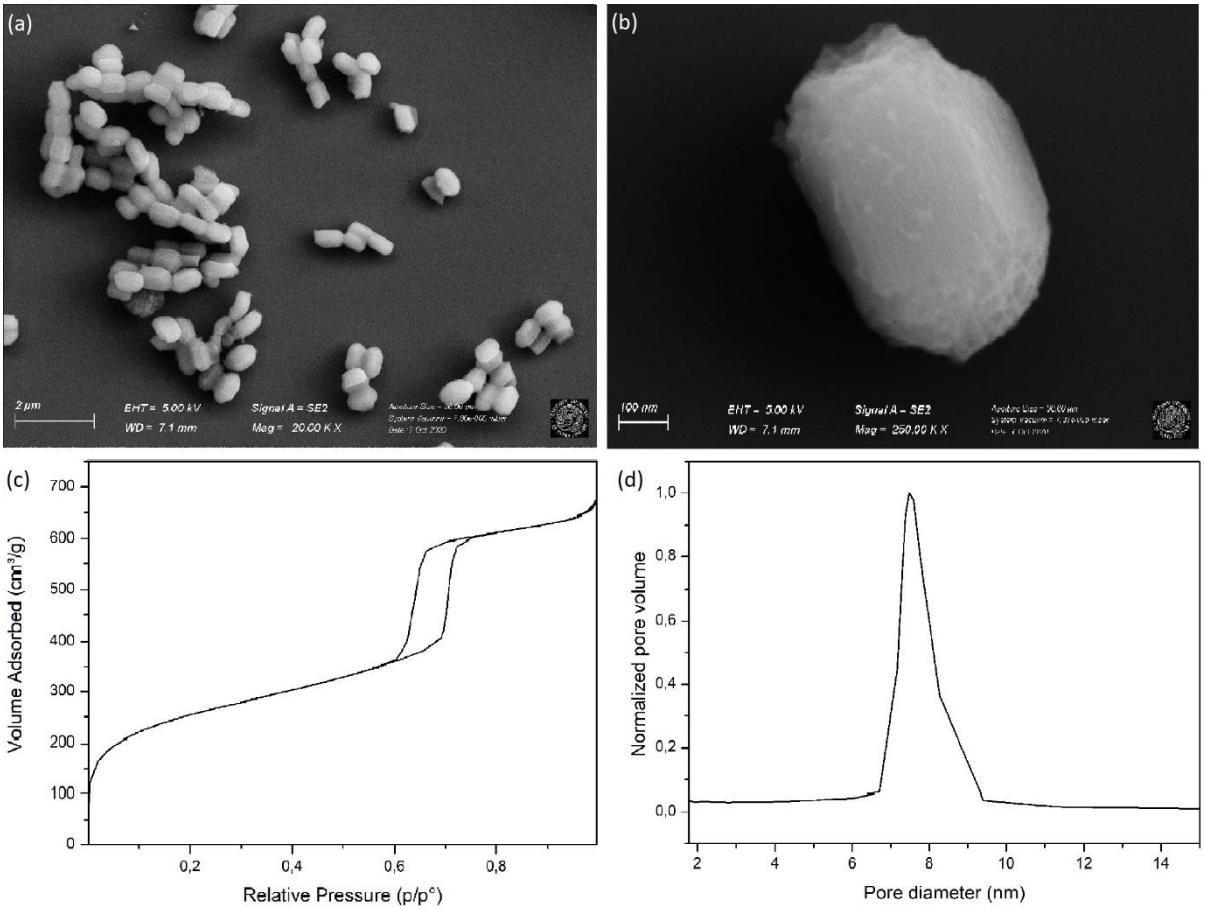

Figures 3.3: (a) and (b) SEM images of MSN_7.5; (c) BET isotherm linear plot of MSN_7.5; (d) MSN_7.5 pore distribution graph.

In Figures 3.3 the SEM images, the BET isotherm linear plot and the pore distribution graph of the first sample SBA-15-type MSNs (synthesized without swelling agent), labelled MSN_7.5, are reported.

BET/BJH analysis showed a surface area of about 873 m^2/g and a pore volume of 0.976 cm^3/g, both values not significantly different from the previous sample. However, Figure 3.3 (d) shows a narrow size distribution centred at 7.5 nm. Looking at the SEM images of Figures 3.3 (a) and (b), it is evident that these MSNs have a completely different shape with respect to the previous MCM-41 MSNs. Figure 3.3 (b) allows also to see the ordered porous long channels. The isotherm shown in Figure 3.3 (c) still follows the type IV shape, despite the evident difference with Figure 3.2 (c) relative to MSN_4.2.

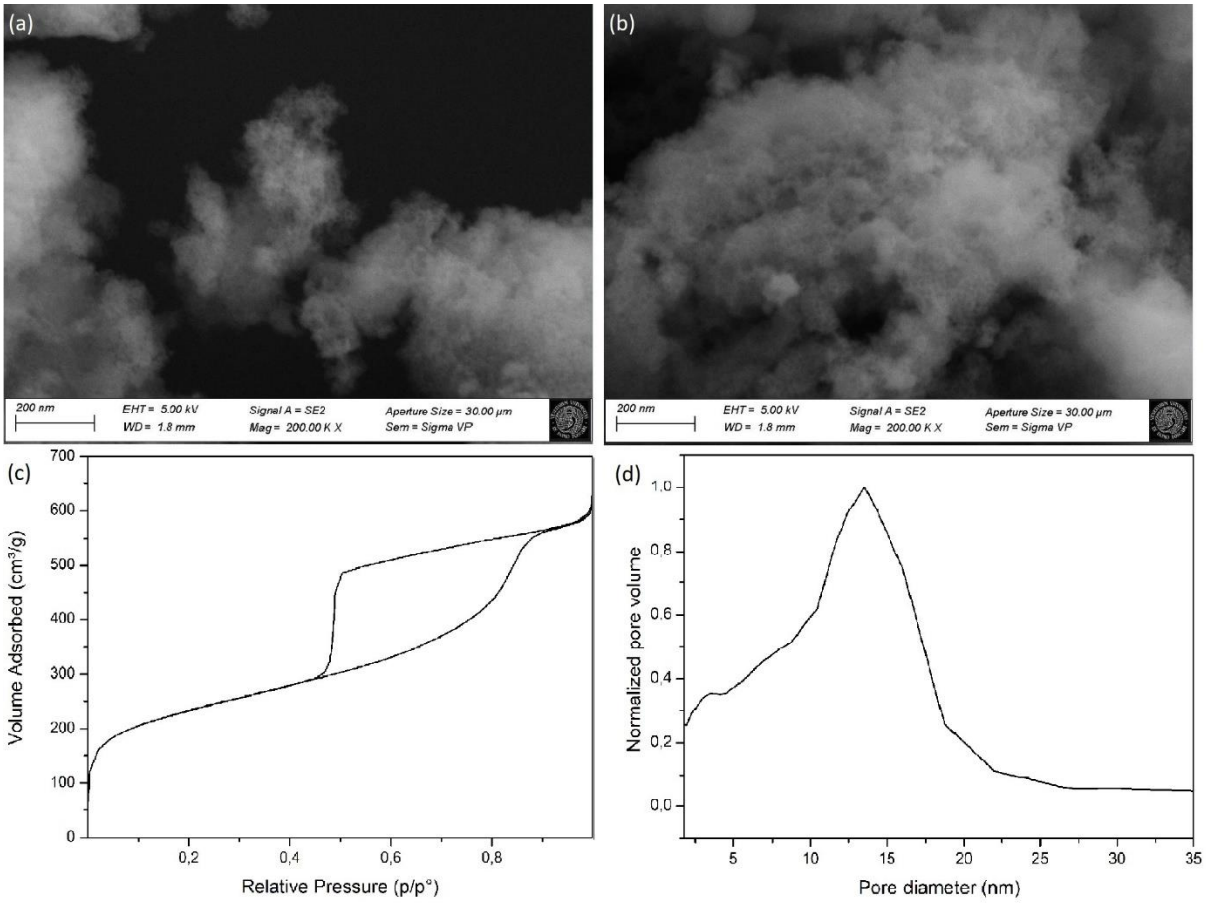

Figures 3.4: (a) and (b) SEM images of MSN_13.5; (c) BET isotherm linear plot of MSN_13.5; (d) MSN_13.5 pore distribution graph.

Results of BET/BJH analyses, together with the SEM images, of the second sample SBA-15-type MSNs are reported in figure 3.4. This sample was synthesized with swelling agent/copolymer ratio of 0.3:1 and labelled MSN_13.5.

The SEM images 3.4 (a) and (b) show immediately the transition to an aspect without a well-defined shape, with respect to the SBA-15 synthesized without swelling agent.

BET/BJH analysis showed the smallest surface area of about 809 m^2/g and the smallest pore volume of 0.875 cm^3/g. Despite this, the plot showing the diameter pore size distribution (Figure 3.4 (d)) shows a size distribution centred at 13.5 nm. The isotherm shown in Figure 3.4 (c) is still identified with the type IV shape.

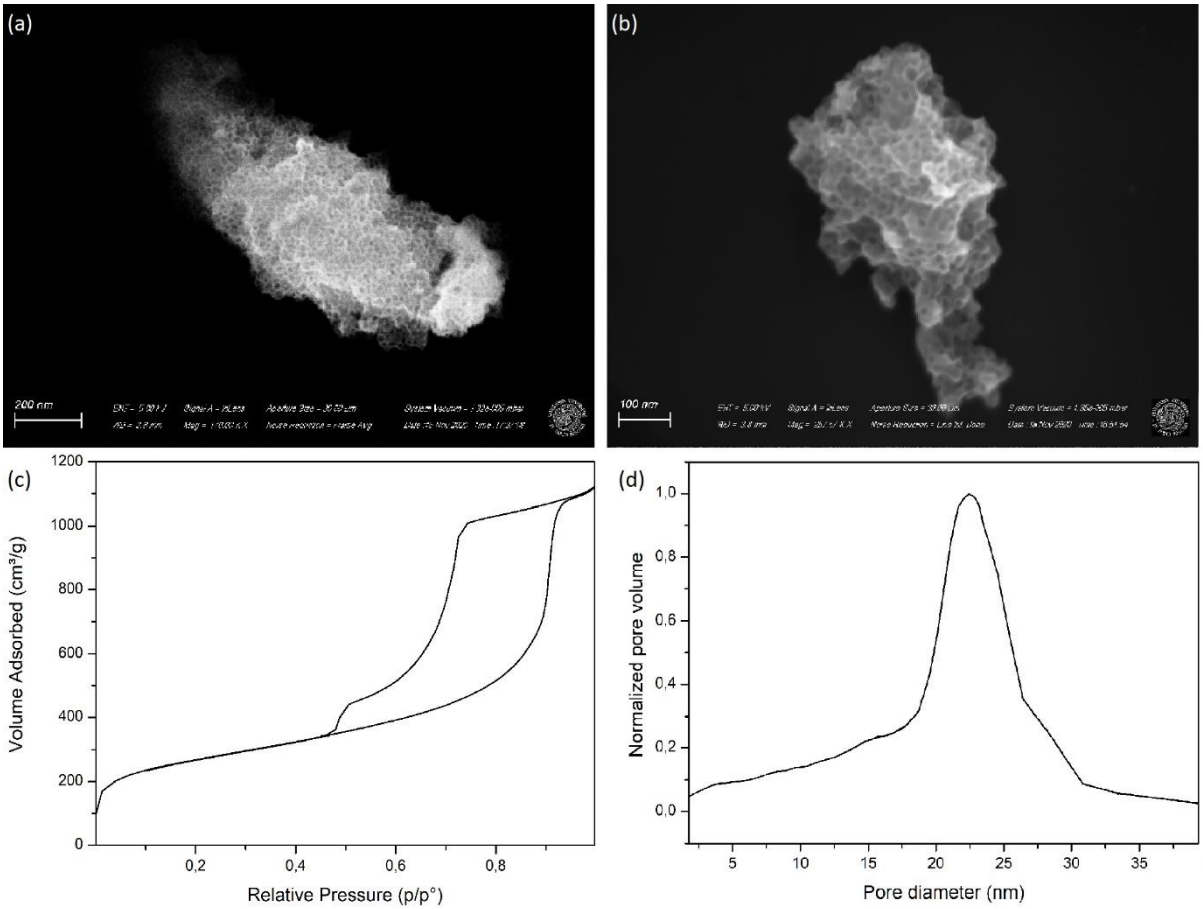

Figures 3.5: (a) and (b) SEM images of MSN_22.4; (c) BET isotherm linear plot of MSN_22.4; (d) MSN_22.4 pore distribution graph.

In figures 3.5 are reported the SEM images, the BET isotherm linear plot and the pore distribution graph of the last sample SBA-15-type MSNs (synthesized with swelling agent/copolymer ratio of 0.5:1), labelled MSN_22.4.
The SEM images 3.5 (a) and (b) still reveal an aspect without a particular form, in addition to clearly visible pores.
From BET/BJH analysis they showed a surface area of about 932 m^2/g, and the highest pore volume of 1.653 cm^3/g. Figure 3.5 shows a size distribution centred at 22.4 nm, representing our biggest pore size nano-reactors. The isotherm shown in figure 3.5 (c) is still identified with the type IV shape.

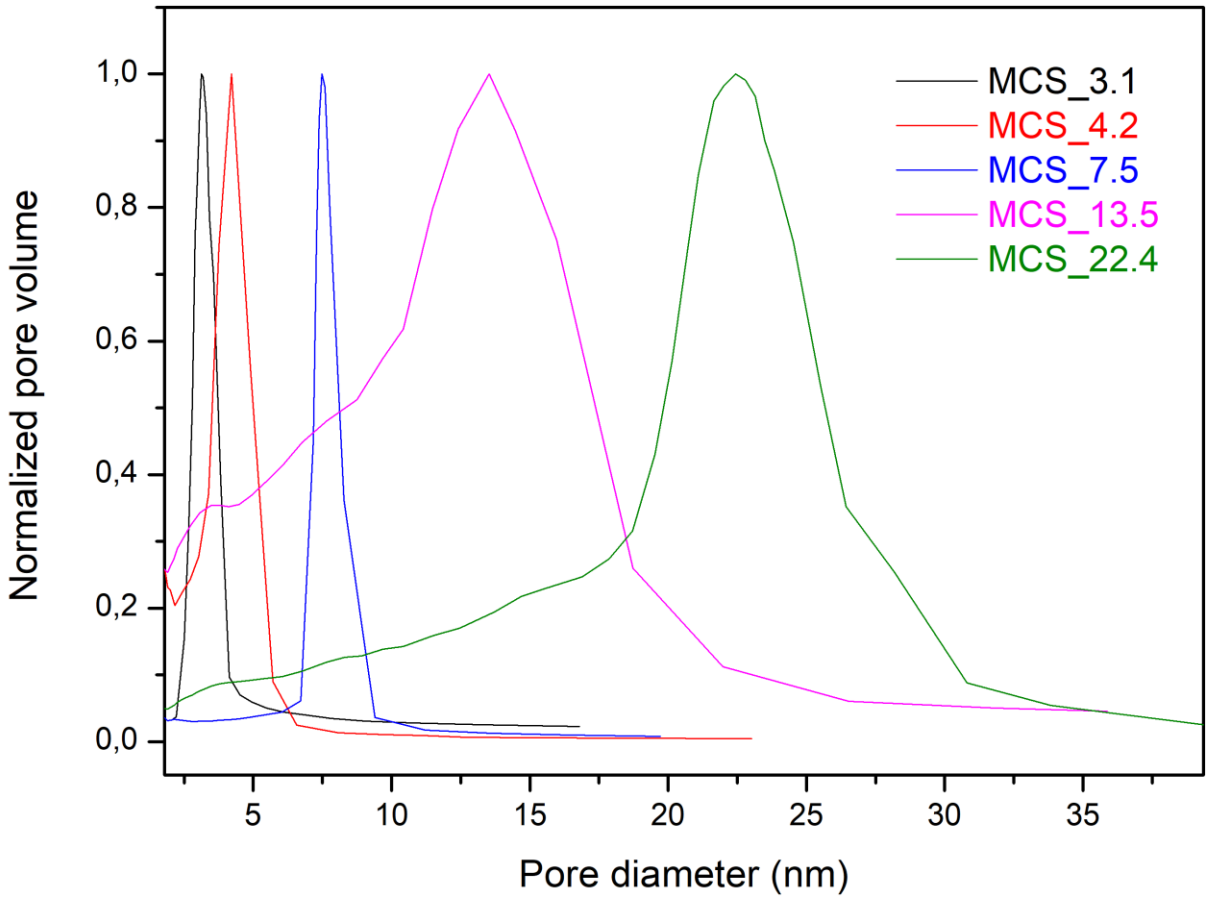

Figure 3.6: pore distribution graphs of MSNs synthesized.

Table 3.1: BET/BJH analysis results

Sample name	BET surface area [m^2/g]	BJH pore volume [cm^3/g]	Pore diameter [nm]
MSN_3.1	1236	1.035	3.1
MSN_4.2	853	0.955	4.2
MSN_7.5	873	0.976	7.5
MSN_13.5	809	0.875	13.5
MSN_22.4	932	1.653	22.4

** : An error of 20% is estimated for all samples*

Table 3.1 and Figure 3.6 summarize the most important characteristics of all synthesized silicas. As evident from Figure 3.6, all syntheses were successful: the main purpose of maintaining good control over pore size is confirmed by the monodisperse pore distributions for each particle type.

3.2 Effect of loading in $Ga_2O_3:Cr^{3+}$@MSN_3.1

As a first step, the effect of the pore loading percentage was investigated. MSN_3.1 were firstly employed. Calculations were performed on the reagent's filling volume considering gallium and chromium salts with respect to the pore volume available and five different percentages of filling volume were tested (12.5, 25, 50, 75 and 100 %). This choice was adopted taking into account the decrease in volume that occurs following the heat treatment necessary to synthesize the oxide. The heat treatment temperature was firstly fixed at 700°C to stabilize the well known β-phase, as confirmed by literature [114-A, 115].
XRPD analyses do not reveal the presence of evident diffraction peaks, as can be seen in Figure 3.7. This is due to the small particle size, as expected by considering the pore size of about 3.1 nm of the MSNs. A broad band between 30° and 40° begins to be visible at the higher loading rates (blue, pink and green lines in Figure 3.7). This could be assigned to the Ga_2O_3 beta phase. However, a clear assignment is not possible. The small differences between the various patterns are due to the greater intensity ratio, in the most loaded samples, between the loaded phase and the amorphous silica host.

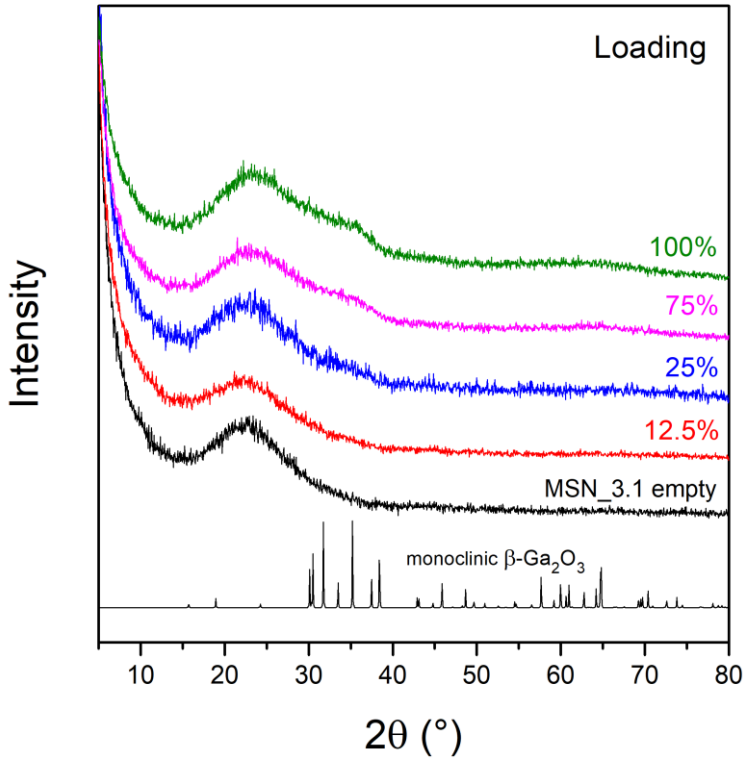

Figure 3.7: XRPD graphs of MSN_3.1 at various loading filling volume of $Ga_2O_3:Cr^{3+}$, treated at 700°C. The diffraction peaks of bulk β-phase are put as a reference (ICSD #83645).

Based on the results, a value of 75% of filling volume of the pores was chosen as a constant parameter for all the syntheses performed in the following. This choice is to be sure of synthesizing nanoparticles confined within the pores, avoiding the growth of Ga_2O_3 NCs outside the MSNs.
Preliminary photoluminescence (PL) analysis does not allow to obtain clear signals.

The next step was to increase the size of the MSNs with the aim of obtaining PL spectra easier to analyse.

3.3 Effect of chromium on $Ga_2O_3:Cr^{3+}$@MSN_4.2

With the aim of studying the effect of different chromium concentrations and being able to collect PL spectra with greater intensity, larger NPs were synthesized within the pores of MSN_4.2, treated at 700°C.

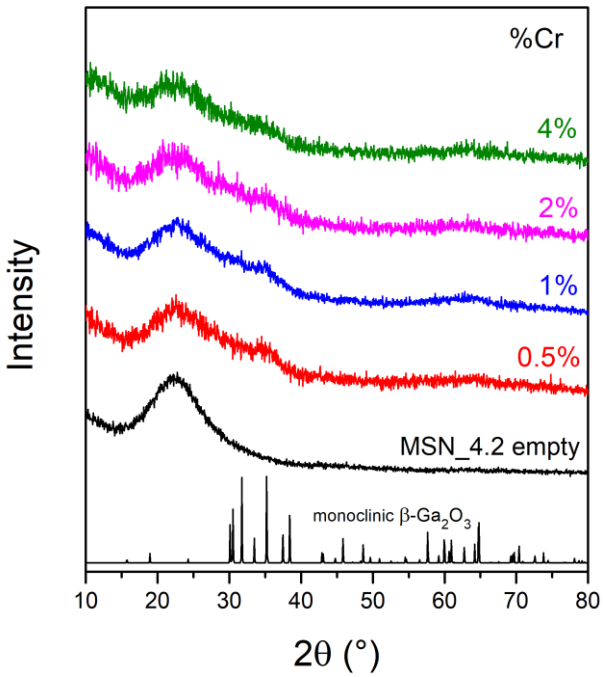

Figure 3.8: XRPD graphs of MSN_4.2 at various Cr^{3+} doping percentages, treated at 700°C.

The first observations made on the XRPD spectra shown in Figure 3.8 do not show particular differences with the XRPD patterns collected for the smaller NPs grown within the pore of MSN_3.1. Not even changing the chromium content a substantial change can be obtained in the XRD patterns, suggesting very small particles grown inside the pores.
The optical properties were investigated collecting the emission (PL) and excitation (PLE) photoluminescence spectra. The spectra of all the samples at the various chromium contents were collected (Figure 3.9), but for Cr at 4% the sample turned out to be completely quenched (not shown).
It is interesting to note that the spectroscopic features of Cr^{3+} can be used as a probe to identify the synthesized phase. In fact, the d-orbitals involved are strongly affected by the local crystal field as well-known from the Tanabe-Sugano diagrams for transition metal ions. In this view it is possible to compare the PL spectra with the spectra obtained from a sample prepared by conventional solid state synthesis. In fact, as a reference, a β-$Ga_2O_3:Cr^{3+}$ solid state (SS) synthesized sample was prepared by treating at 1000°C a mixed stoichiometric amount of oxides, with chromium content of 0.25% ($Cr_{0.005}Ga_{1.995}O_3$). In all successive figures, the SS reference in PL/PLE normalized spectra will be indicated by a gold line.

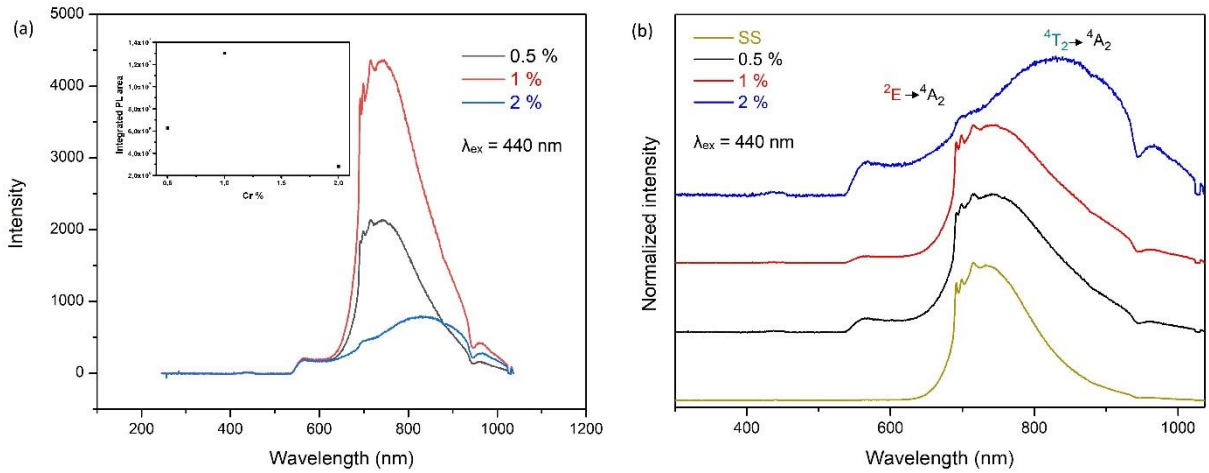

Figure 3.9: (a) PL emission spectra of MSN_4.2 at various Cr^{3+} doping percentages, treated at 700°C. The insight shows the integrated PL areas calculated between 650 nm and 1000 nm. (B): The previous spectra normalized, with transitions signed.

For 4 nm size particles, increasing chromium content from 0.5% to 1%, there is a growing intensity due to the higher amount of luminescent centres and the spectral shape (Figure 3.9 (b)) remains almost identical, easily identifiable as a β-phase. At 2%, instead, in addition to the occurrence of the concentration quenching phenomenon, a marked shift of the emission centre occurs. The spectral shape is radically different and could be interpreted as the result of higher concentration of chromium inducing a shift of the broad band towards higher wavelengths (red-shift), weakening the crystal field, and together with the tendency to disappear of the $^2E \rightarrow {}^4A_2$. This could be interpreted as a phase mixing effect occurring in this sample. Another hypothesis is the possibility that chromium perceives a different crystal field induced by the increase of chromium atoms in the lattice. Another possibility is that, as the quantity of chromium increases, all the preferential positioning sites in the unit cell are occupied by the chromium itself and therefore it occupy other different sites. Consequently, this leads to chromium atoms that perceive different crystal fields affecting the PL. Another possibility for the presence of several phases is that the synthesis of gallia took place not totally inside the silica pores. Although there was no clear information in the X-ray patterns that could lead to suspect this, there is no certain evidence that this could not have happened.

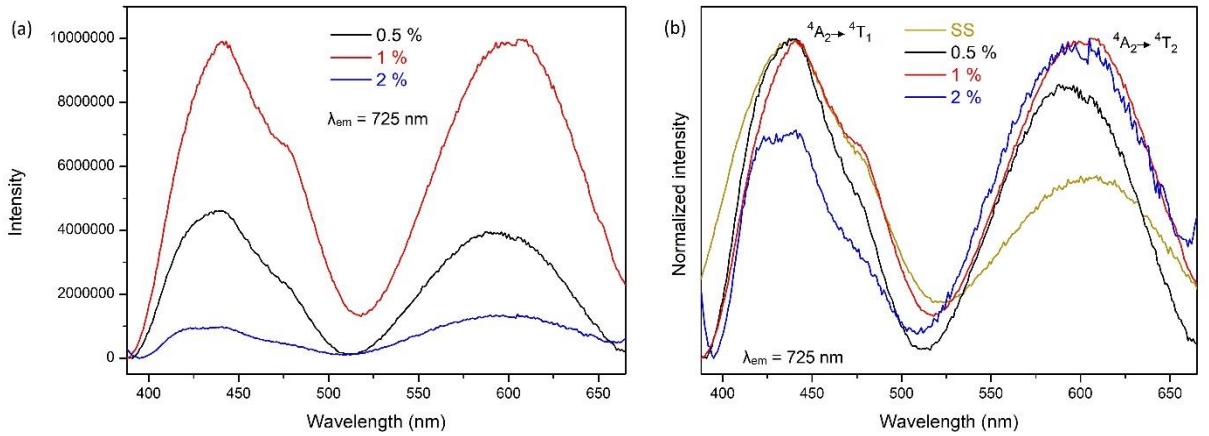

Figure 3.10: (a) PLE spectra of MSN_4.2 at various Cr^{3+} doping percentages, treated at 700°C. (b): The previous spectra normalized, with transitions signed.

As can be seen in Figure 3.10, the trend of the excitation intensities consistently follows the same shown in emission: there is an increase in intensity up to 1% of doping and then, after a further increase in chromium concentration, the intensity decreases. The low intensities of the PLE spectra does not allow a clear interpretation of the spectral shapes, due to the high background noise. However, for Cr 1% and 2%, no clear differences are detected between the centres of the various bands and this is particularly important with regard to the $^4A_2 \rightarrow {}^4T_2$ absorption, related to the strength of the crystal field 10*Dq*. The 2% chromium sample, which in the PL graph shows a shift of the $^4T_2 \rightarrow {}^4A_2$ emission band position, is positioned substantially at the same wavelength as the 1% sample. This behaviour supports the hypothesis that chromium is always in the same crystallographic phase, but there could be multiple octahedral coordination sites as recently suggested [114-B].
The composition at 0.5% is instead different: the centre of the $^4A_2 \rightarrow {}^4T_2$ excitation band shows a blue shift compared to the other two samples, corresponding to a stronger crystalline field. Despite this, the PL spectra is identical to that of the 1% chromium sample and to that of the SS β-phase reference, as can be clearly seen in figure 3.9.

Table 3.2: 10Dq parameter for NCs@MSN_4.2 at various Cr^{3+} doping percentages, treated at 700°C.

Sample (Cr %)	0.25 (SS)	0.5	1	2
10*Dq* (cm^{-1})	16611	16892	16694	16750

Despite the non-monotonous trend of the crystal field energies showed in Table 3.2, going from 0.5% Cr to 2%, the effect of the chromium concentration on the field strength is evident. The origin of such decrease of the strength moving from 0.5% to 1% of Cr and then increasing at 2% is difficult to define with certainty due to the wide number of factors contributing: the possible arrangement of Cr^{3+} in sites other than octahedral (as shown in Figure 1.9), the presence of crystalline defects, the size of the NPs.

In addition to the band position and, therefore, the 10*Dq*, the chromium concentration also affects the ratio between their intensities: as the chromium concentration increases, the $(^4A_2 \rightarrow {}^4T_2)/(^4A_2 \rightarrow {}^4T_1)$ ratio progressively increases. The plot of these ratios is shown in Figure 3.11.

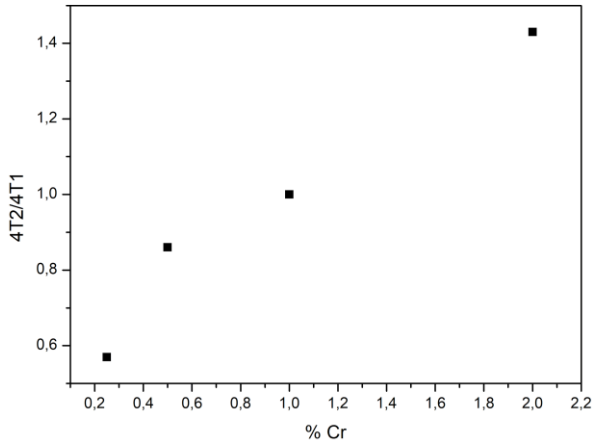

Figure 3.11: ratio ($^4A_2 \rightarrow {}^4T_2$)/($^4A_2 \rightarrow {}^4T_1$) of MSN_4.2 at various Cr^{3+} doping percentages, treated at 700°C (with reference at 0.25% of Cr).

Table 3.3: ratio ($^4A_2 \rightarrow {}^4T_2$)/($^4A_2 \rightarrow {}^4T_1$) of MSN_4.2 at various Cr^{3+} doping percentages, treated at 700°C.

% Cr	($^4A_2 \rightarrow {}^4T_2$)/($^4A_2 \rightarrow {}^4T_1$)
0.25 (SS)	0.57
0.5	0.86
1	1
2	1.43

This effect of ratio variation between the PLE bands can be attributed to the variation of the Racah parameter *B*: given the nanometric size of particles, the ratio between surface atoms and bulk atoms influence the crystallinity and consequently the values of ionic and covalent components of bonds. By varying the chromium quantity, it is possible that chromium is preferentially distributed in certain sites, at surface or the core, influencing this parameter.
Moving from 3.1 to 4.2 nm, the increase in particle size improves the signals keeping the same β-phase shape.

3.4 Effect of temperature in $Ga_2O_3:Cr^{3+}$@MSN_4.2

According to literature [114-A, 115], the α-Ga_2O_3 phase can be stabilized by treating hydroxides at 500°C, while the β-phase can be reached from various precursors at over 600-650°C. With the aim of investigating the temperature effect on the different polymorphs stabilization, 500°C, 700°C and 900°C were selected.
XRPD analysis was performed on a series of NPs synthesized in MSNs with pores of 4.2 nm diameter, obtained from the same batch and subsequently divided into three samples to be treated at these temperatures. The chromium content was kept at 0.5%.

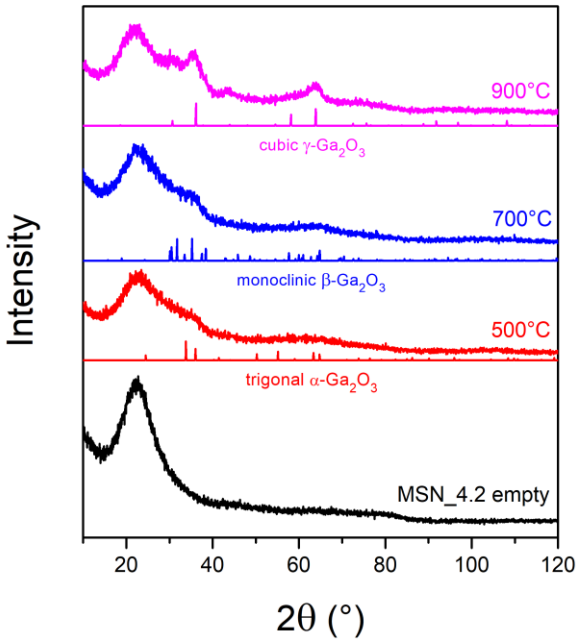

Figure 3.12: XRPD graphs of MSN_4.2 at various temperatures, with constant chromium content fixed at 0.5%. The diffraction peaks of bulk α β and γ phases are put as a reference. (ICSD #27431) (ICSD #83645) (ICSD #152085)

Observing Figure 3.12, the lack of sharp diffraction peaks is in agreement with the synthesis inside the pores.
As we approach 900°C, diffraction peaks around 31°, 36°, 44°, 58° and 64° gradually emerge. These characteristic angles are not sufficient to assign the γ-phase rather than β-phase unambiguously, but the progressive increase in intensity at these angles suggests the presence of the γ-phase especially at 900°C. A better definition of peaks at 900°C is also due to a better crystallization at the higher temperature.

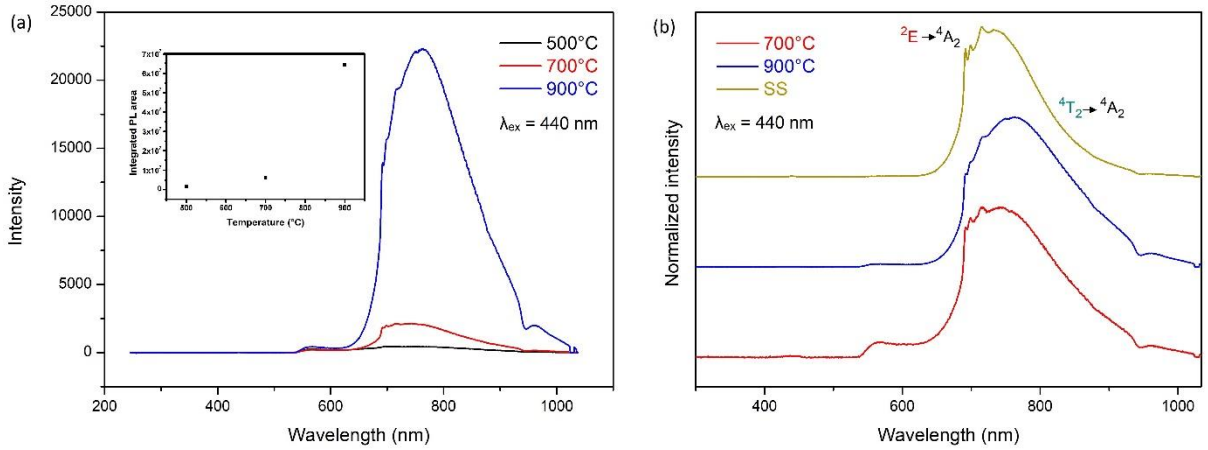

Figure 3.13: (a) PL emission spectra of MSN_4.2 at various temperatures, with constant chromium content fixed at 0.5%. The insight shows the integrated PL areas calculated between 650 nm and 1000 nm. (b): The previous spectra normalized, except for the 500°C, with transitions signed.

The sample treated at 500°C was omitted from figures 3.13 (b) and 3.14 (b) due to its signal, too low to be distinguished from background noise (as can be clearly seen from figures 3.13 (a) and 3.14 (a)).

The PL emission in figure 3.13 shows a dramatic increase in emitted radiation intensity moving from lower to higher treatment temperatures: this effect can be due to the better crystallization of the particles which occurs at higher temperatures. A smaller presence of defects leads to a greater capacity to absorb, and then to emit, radiation. However, the normalized PL graph reveals more information about the spectral shape: the characteristic sharp $^2E \rightarrow {}^4A_2$ transition (*R*-lines) are clearly visible, and the centre of the broadband due to the $^4T_2 \rightarrow {}^4A_2$ transition moves from 740 nm at 700°C, to 763 nm at 900°C. This variation of the spectral shape shifts the system to weaker crystal fields, allowing to hypothesize a phase change, from the β-phase stabilized at 700°C to the γ-phase at 900°C.
The NPs@MSN_4.2 treated at 700°C are surely β-phase, and it could however still be present at 900°C, as the $^2E \rightarrow {}^4A_2$ transition is still visible.

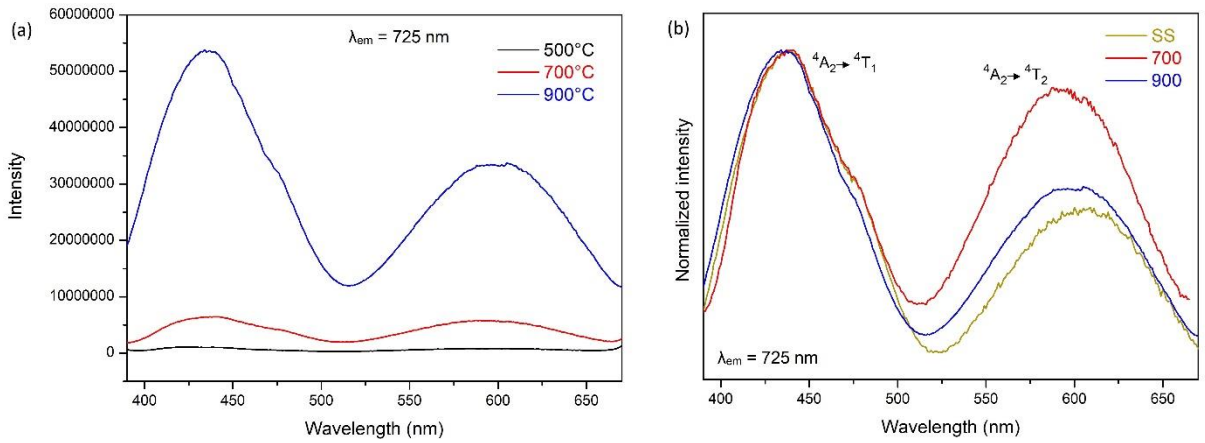

Figure 3.14: (a) PLE spectra of MSN_4.2 at various temperatures, with chromium content fixed at 0.5%. (b): The previous spectra normalized, except for the 500°C, with transitions signed.

The PLE spectra as a function of temperatures shown in Figure 3.14 confirm the increase in the radiation emitted at the highest temperature, but they do not allow to confirm the hypotheses formulated by the emission spectra. As it is possible to see more clearly from table 3.4, by comparing the two samples at the two different temperatures it is noted that the sample treated at 700°C, which is certainly β-phase, has a completely different crystal field strength from that of the SS reference. Based on the observations of the 10*Dq* parameter reported in Table 3.4, the progressive decrease in energy passing from the sample stabilized at 700°C to that at 900°C is consistent with the progressive, even if perhaps not complete, passage from the β-phase to the γ-phase. The latter, characterized by greater bond distances than β-phase as seen in chapter 1.5, will be characterized by weaker fields and therefore by 10*Dq* lower energy.

Table 3.4: 10Dq parameter for NCs@MSN_4.2 at various temperatures, with chromium content fixed at 0.5%.

Sample (°C)	1000 (SS)	700	900
10*Dq* (cm^{-1})	16611	16892	16750

There is also a change in the intensity ratios between the $^4A_2 \rightarrow {}^4T_1$ and $^4A_2 \rightarrow {}^4T_2$ bands: at 900°C the first band absorbs much more, proportionally, than the other treatment temperature. As mentioned above, this variation can be consistently attributed to the different degree of ionic and covalent components of the bonds, since changing the treatment temperature greatly influences the crystallinity degree of particles and therefore the quantity of defects.

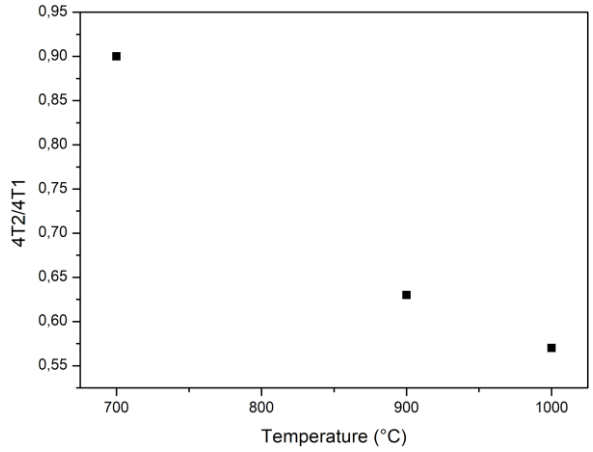

Figure 3.15: ratio ($^4A_2 \rightarrow {}^4T_2$)/($^4A_2 \rightarrow {}^4T_1$) of MSN_4.2 at various temperatures, with chromium content fixed at 0.5% (with reference at 1000°C).

Table 3.5: ratio ($^4A_2 \rightarrow {}^4T_2$)/($^4A_2 \rightarrow {}^4T_1$) of MSN_4.2 at various temperatures, with chromium content fixed at 0.5%.

Temperature	($^4A_2 \rightarrow {}^4T_2$)/($^4A_2 \rightarrow {}^4T_1$)
700	0.90
900	0.63
1000 (SS)	0.57

After having ascertained 900°C as the optimal temperature to have the most intense photoluminescence signals, the next step was to study the effect of temperature and chromium percentage on even larger particles.

3.5 Effect of temperature in $Ga_2O_3:Cr^{3+}$@MSN_7.5

With the aim of investigating larger $Ga_2O_3:Cr^{3+}$ NCs, MSNs with larger pores were employed. In particular, the synthesis was conducted into the pores of about 7.5 nm of diameter, then the batch was divided for three different thermal treatments: at 500°C, 700°C and 900°C. The thermal treatment at 900°C was carried out on four different chromium percentages (Chapter 3.6).
To compare the effect of different temperatures, the same 0.5% of chromium was fixed for all the samples.

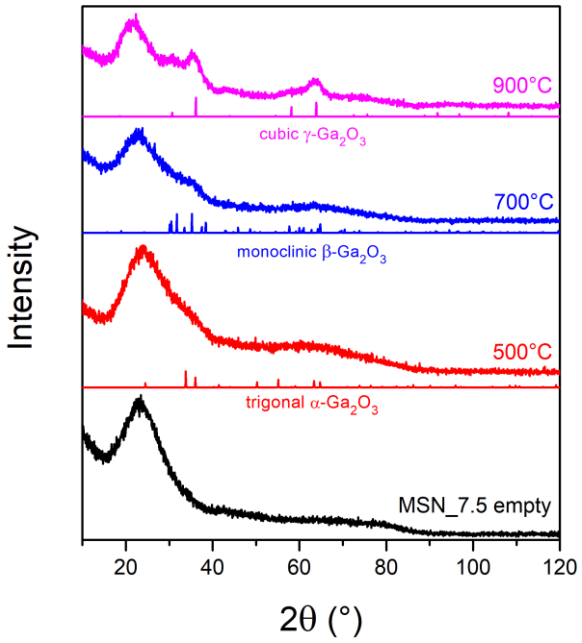

Figure 3.16: XRPD graphs of MSN_7.5 at various temperatures, with constant chromium content fixed at 0.5%.

X-ray diffraction analysis shown in Figure 3.16 does not show particular differences from that made with smaller particles, but still the sample treated at 900°C looks very different from the others. The spectroscopic analysis was employed to get information about phase stabilisation. Even though the spectra were collected for all the temperatures, the NCs synthesized at 500°C and 700°C are characterized by very weak PL signals (as can be seen in figure 3.17 (a)), making it difficult to distinguish the sample signal from the background noise.

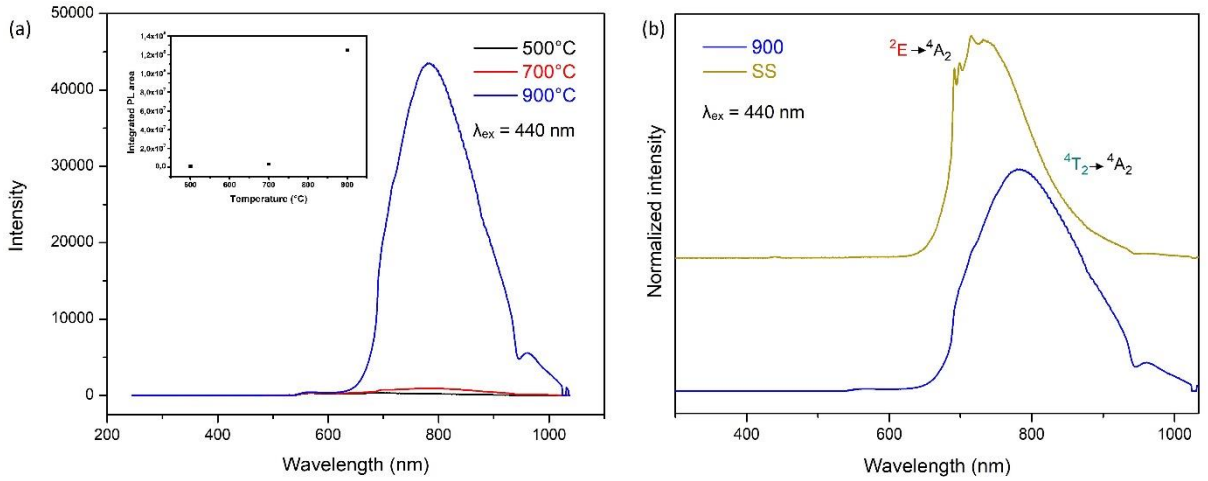

Figure 3.17: (a) PL emission spectra of MSN_7.5 at various temperatures, with constant chromium content fixed at 0.5%. The insight shows the integrated PL areas calculated between 650 nm and 1000 nm. (b): PL normalized spectrum of the sample treated at 900°C, with transitions signed.

Like in the previous analysis on particles of smaller sizes, by increasing the temperature of synthesis, the PL emission increases. Emission at 500°C is barely visible and too weak to be distinguished from the background noise, similarly for the sample treated at 700°C. Instead, at 900 °C, the sample is characterized by a strong emission with a spectral shape quite different

from the typical feature of Cr^{3+} in β-phase. This would further confirm the stabilization of the cubic γ-Ga_2O_3 at 900°C.

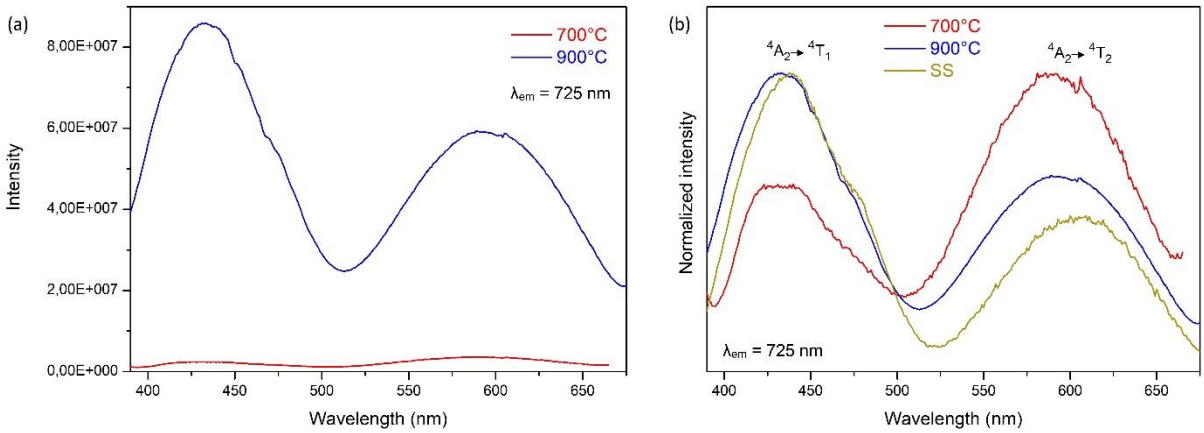

Figure 3.18: (a) PLE spectra of MSN_7.5 at 700°C and 900°C, with chromium content fixed at 0.5%. (b): The previous spectra normalized, with transitions signed.

The difference in terms of absorption is evident also for the particles stabilized at 900°C, coming to differ by more than an order of magnitude: this confirms the considerations made for the effect of temperature on the crystallinity of particles. Figure 3.18 (b) shows a different behaviour with respect to the lower size: between the two bands, always centred at approximately the same wavelength, there is not only a change in the relative intensity ratios, but even an inversion of the excitation maxima: at 700°C the system is optimally excited at the $^4A_2 \rightarrow {}^4T_2$ band while at 900°C the optimal excitation band is the $^4A_2 \rightarrow {}^4T_1$. By raising the temperature from 700°C to 900°C the decreasing trend of the ratio between bands is maintained for Ga_2O_3:Cr^{3+} NCs in both MSN_4.2 (Figure 3.15) and MSN_7.5 (Figure 3.19).

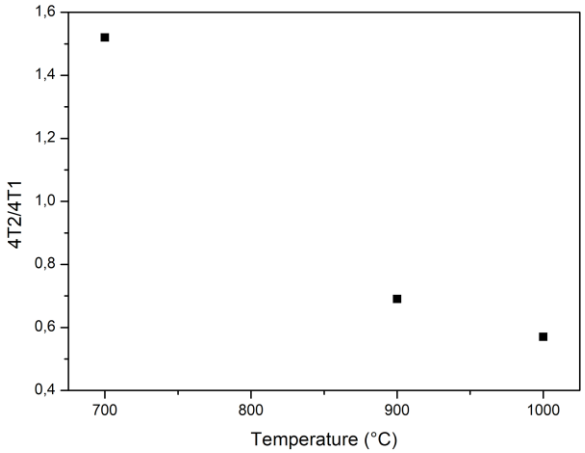

Figure 3.19: ratio ($^4A_2 \rightarrow {}^4T_2$)/($^4A_2 \rightarrow {}^4T_1$) of MSN_7.5 at various temperatures, with chromium content fixed at 0.5% (with reference at 1000°C).

Table 3.6: ratio ($^4A_2 \rightarrow {}^4T_2$)/($^4A_2 \rightarrow {}^4T_1$) of MSN_7.5 at various temperatures, with chromium content fixed at 0.5%.

Temperature	($^4A_2 \rightarrow {}^4T_2$)/($^4A_2 \rightarrow {}^4T_1$)
700	1.52
900	0.69
1000 (SS)	0.57

Table 3.7: *10Dq parameter for NCs@MSN_7.5 at various temperatures, with chromium content fixed at 0.5%.*

Sample (°C)	1000 (SS)	700	900
10*Dq* (cm^{-1})	16611	16920	16835

Firstly, observing the multiplet energy level diagram proposed by Ogasawara [137], which put in relation the multiplet energy levels with the <Ga-O> bond length, and subsequently confirming the hypotheses made in Chapter 3.4 (about the inverse relationship between <Ga-O> bond distance and 10*Dq* value) by considering the information obtained through PL, PLE and the values reported in the literature of the bond distances for the different phases, we can say that we have stabilized the γ-phase.
The estimated binding distance <Ga-O> = 2.060 Å for the γ-phase, greater than the α (1.999 Å) and β (2.012 Å) phases, and the calculated value of 10*Dq* for the two temperatures shown in Table 3.7, agree with the observed shift in the PL spectrum at 900°C (Figure 3.17) which would indicate a lower crystal field strength.

3.6 Effect of chromium in $Ga_2O_3:Cr^{3+}$@MSN_7.5

By considering the optimal temperature of 900°C to optimize the photoluminescence signals, the study of the effects of the chromium content on the PL properties was performed by fixing the same thermal treatment for all the samples.

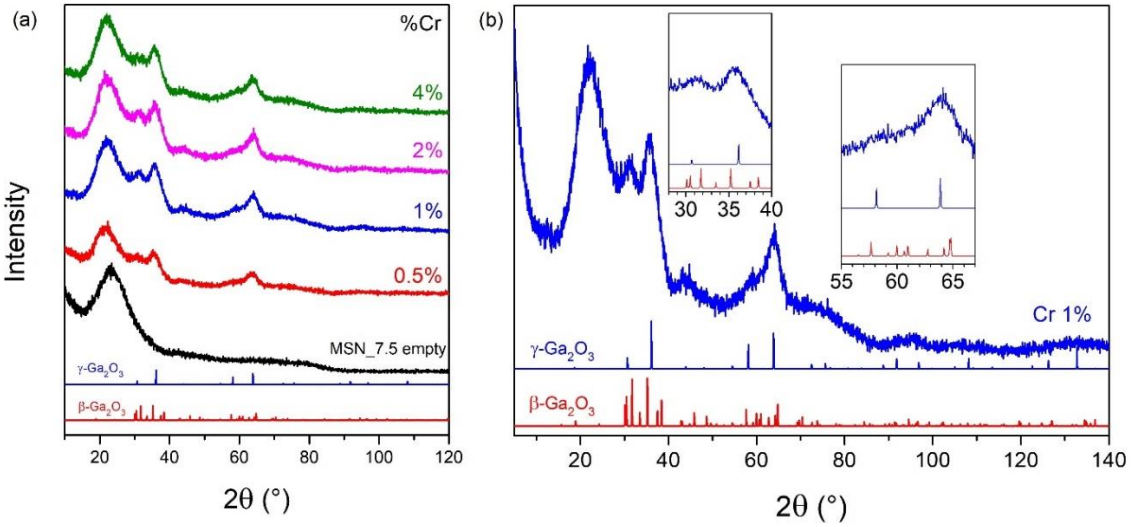

Figure 3.20: (a) XRPD graphs of MSN_7.5 at various Cr^{3+} doping percentages, treated at 900°C. (b): Focus on sample at 1% Cr.

As the percentage composition of chromium varies, all the XRPD patterns remain substantially unchanged. As can be seen in figure 3.20 (b), the comparison with the specific patterns of the β and γ phases seems to suggest the stabilization of the γ-phase. The two insights for the intervals 28°-40° and 55°-67° clearly show the coincidence of the sample peaks with those of the cubic phase.
In addition, the temperature seems to be the most important parameter for the phase stabilization.

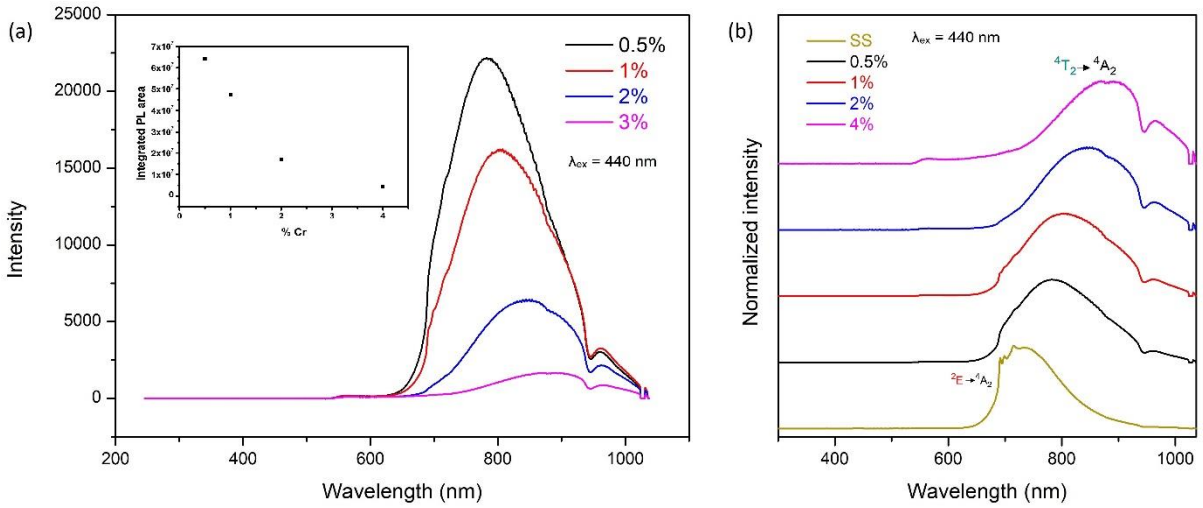

Figure 3.21: (a) PL emission spectra of MSN_7.5 at various Cr^{3+} doping percentages, treated at 900°C. The insight shows the integrated PL areas calculated between 650 nm and 1000 nm. (b): The previous spectra normalized, with transitions signed.

The influence of chromium becomes more evident by observing the PL spectra in Figure 3.21: in addition to the clear concentration quenching, further information that leads to confirm the stabilization of the γ-phase is obtained by observing the normalized PL spectra in Figure 3.21 (b): the variation of the chromium concentration involves an evident progressive shift of the broad band to weaker fields, whose broad band spectral shape clearly cannot be that of the β-phase. The plot of band position is reported in figure 3.22. This behaviour of chromium lead to think of a progressive decrease in the strength of the crystal field. Previous studies had already observed that an increase in Cr^{3+} concentration displaces some signals in the spectra [138, 139], but to the best of our knowledge this is the first time it is observed in the Ga_2O_3 system.

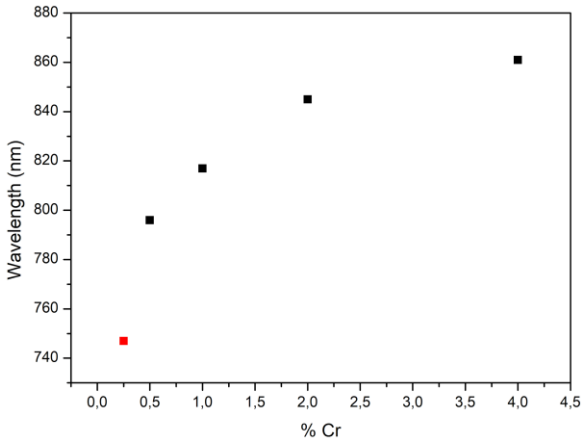

Figure 3.22: $^4T_2 \rightarrow {}^4A_2$ band centre of MSN_7.5 at various Cr^{3+} doping percentages, treated at 900°C. The red point is the SS reference. The centre was measured in the width at half height.

Table 3.8: $^4T_2 \rightarrow {}^4A_2$ band centre of MSN_7.5 at various Cr^{3+} doping percentages, treated at 900°C.

% Cr	Wavelength (nm)
0.25 (SS)	747
0.5	796
1	817
2	845
4	861

It is also noted that the intensity trend for the first two percentages is reversed compared to that observed previously for NCs of smaller size treated at 700°C. To confirm whether this effect is due to size or temperature, a further sample was synthesized with the 1% chromium within MSN_7.5 and treated at 700°C. The results are shown in Figure 3.23.

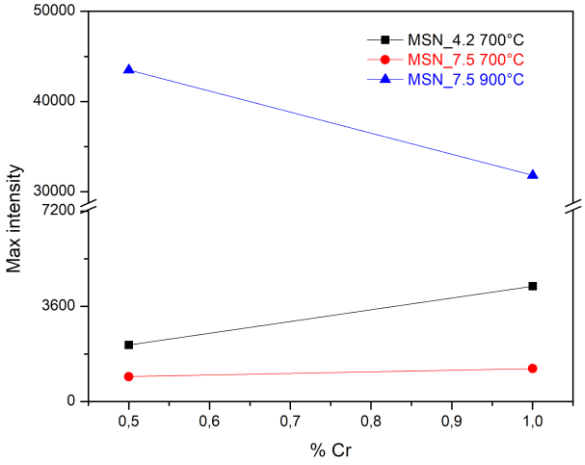

Figure 3.23: Maximum intensity comparison between samples at 0.5% and 1% of Cr at 700°C and 900°C

The graph shows a change in trend due to the temperature: at 700°C the maximum emission is reached at a composition of 1% of dopant; at 900°C the trend changes and the highest emission is at 0.5% of chromium. This characteristic is also consistent with the considerations on the stabilization of the γ-phase at 900°C, where a different crystalline environment changes the dopant's behaviour.

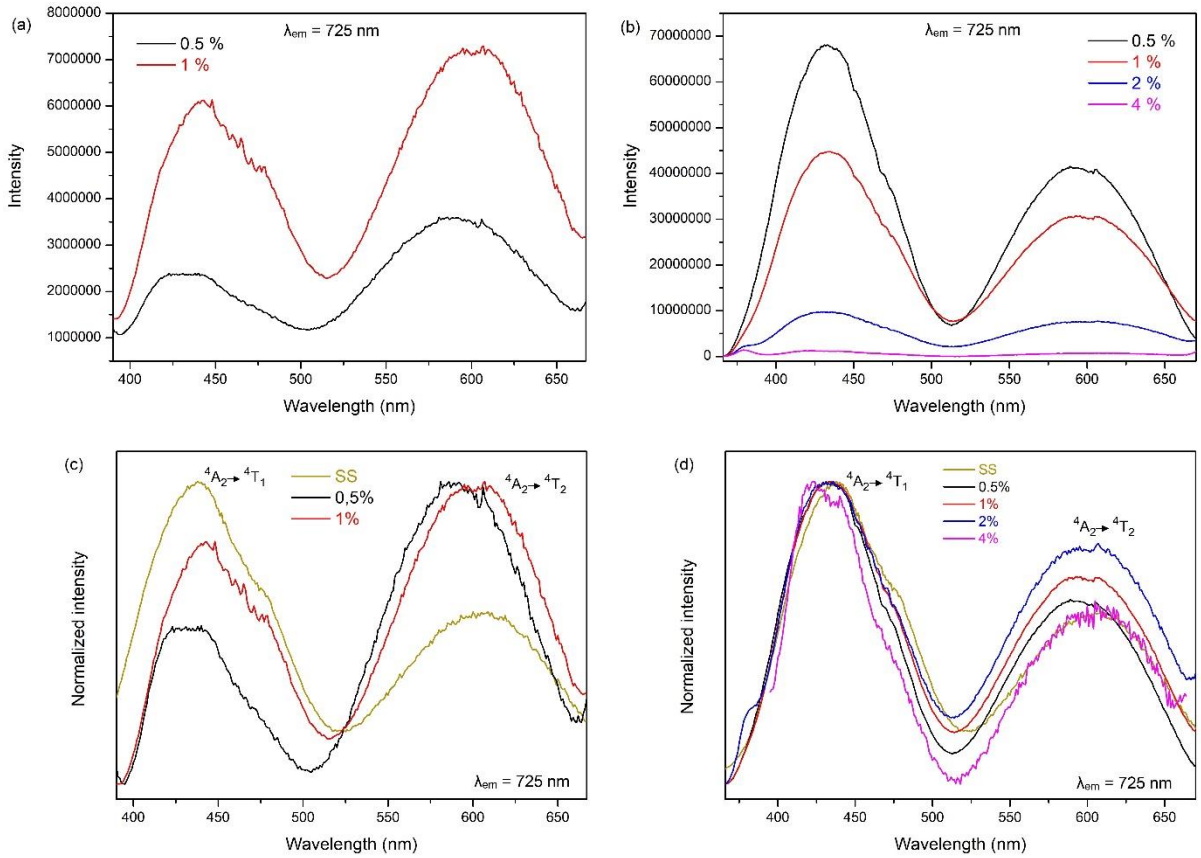

Figure 3.24: (a) PLE spectra of MSN_7.5 at 0.5 and 1% of Cr^{3+}, treated at 700°C. (b): PLE spectra of MSN_7.5 at various Cr^{3+} doping percentages, treated at 900°C. (c) and (d): respectively, the previous spectra normalized, with transitions signed.

From the PLE spectra in figures 3.24 (a) and (b), the decreasing trend of absorption intensity with increasing dopant concentration was confirmed, including the particular reversal behaviour between the percentages 0.5% and 1% at 900°C with respect to the same at 700°C. From the normalized PLE spectra 3.24 (c) and (d), it can be seen how the chromium concentration affects the PLE bands position and intensity ratio. Samples at 700°C show the same behaviour of their counterparts @MSN_4.2 pore size, moving to weaker crystal fields by increasing the chromium content.

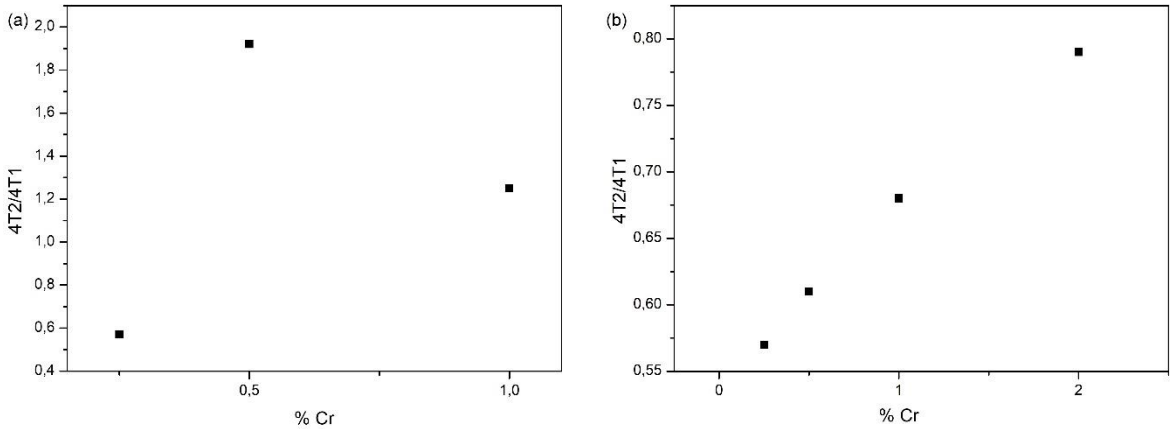

Figure 3.25: (a) ratio ($^4A_2 \rightarrow {}^4T_2$)/($^4A_2 \rightarrow {}^4T_1$) of MSN_7.5 at various Cr^{3+} doping percentages, treated at 700°C with reference at 0.25% Cr. (b): Ratio ($^4A_2 \rightarrow {}^4T_2$)/($^4A_2 \rightarrow {}^4T_1$) of MSN_7.5 at various Cr^{3+} doping percentages, treated at 900°C with reference at 0.25% Cr.

Table 3.9: ratio ($^4A_2 \rightarrow {}^4T_2$)/($^4A_2 \rightarrow {}^4T_1$) of MSN_7.5 at various Cr^{3+} doping percentages, treated at 700°C.

% Cr	($^4A_2 \rightarrow {}^4T_2$)/($^4A_2 \rightarrow {}^4T_1$)
0.25 (SS)	0.57
0.5	1.92
1	1.25

Table 3.10: ratio ($^4A_2 \rightarrow {}^4T_2$)/($^4A_2 \rightarrow {}^4T_1$) of MSN_7.5 at various Cr^{3+} doping percentages, treated at 900°C.

% Cr	($^4A_2 \rightarrow {}^4T_2$)/($^4A_2 \rightarrow {}^4T_1$)
0.25 (SS)	0.57
0.5	0.61
1	0.68
2	0.79

Looking at tables 3.9 and 3.10, the inversal trend induced by the two temperatures can be clearly seen. In the samples treated at 900°C, the relative increase of the PLE intensity of $^4A_2 \rightarrow {}^4T_2$ compared to $^4A_2 \rightarrow {}^4T_1$ is progressive as the chromium content increases. The 4% sample interrupts this trend; however, the low signal did not allow to obtain well-defined spectra due to an almost complete concentration quenching, making the background noise a severe problem for a reliable interpretation. The samples treated at 700°C show an inverse

behaviour: the relative intensity of the $^4A_2 \rightarrow {}^4T_1$ transition increases compared to that of $^4A_2 \rightarrow {}^4T_2$ moving from the lowest to the highest chromium concentration.

Regarding the band shift induced by the Cr content, in the PLE spectra of the NCs treated at 900°C (Figure 3.24 (d)) the band centre of the $^4A_2 \rightarrow {}^4T_2$ transition (i.e. the crystal field strength *Dq*) shifts from 594 nm to 597 nm, 599 nm and 633 nm progressively moving from a chromium content of 0.5% to 4%; so, the 10*Dq* value pass from 16835 cm^{-1} to 16750 cm^{-1}, 16694 cm^{-1} and 16584 cm^{-1} progressively. This trend is shown in Figure 3.26.

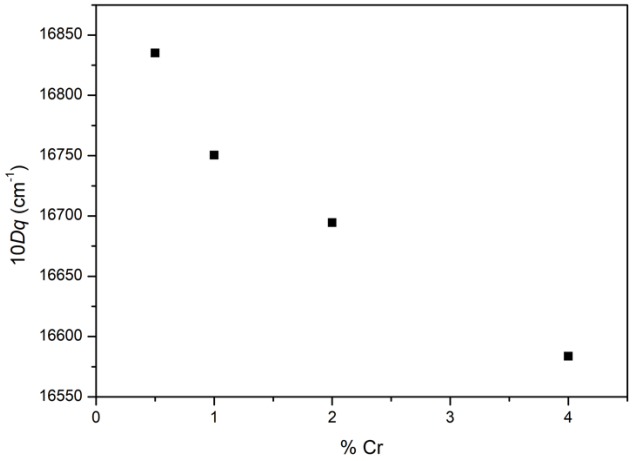

Figure 3.26: 10Dq values of MSN_7.5 at various Cr^{3+} doping percentages, treated at 900°C.

This shift of the $^4A_2 \rightarrow {}^4T_2$ transition (correlated to the strength of the crystal field) indicates a progressive weakening of the field strength perceived by chromium, which may be due to different factors such as (i) chromium distribution effects on different sites [114-B], (ii) the intrinsic presence of defects in the NCs or (iii) the progressive effect of the Cr themself.
Looking at the crystal field strength 10*Dq*, it is evident that the red shift of the PL spectra can be explained with the weakening of the crystal field: as the chromium concentration increases, the crystal field weakens.

Following all the observations made so far, it can be concluded that the key parameter for the phase stabilization is the temperature. Considering the difficulty of obtaining clear XRPD patterns due to the small size of the Ga_2O_3 NCs and the greater quantity of glassy material, the silica, that envelops them, the optical properties of chromium are therefore used as a probe for investigating the structure of gallium oxide.
To further investigate by XRPD the phase, the silica was etched to directly analyse the crystalline small NCs without the glass phase. The etching was carried out by stirring the sample doped with 4% of Cr in a 2M NaOH solution for 2 hours, and analysed after precipitation, washed with water and dried.

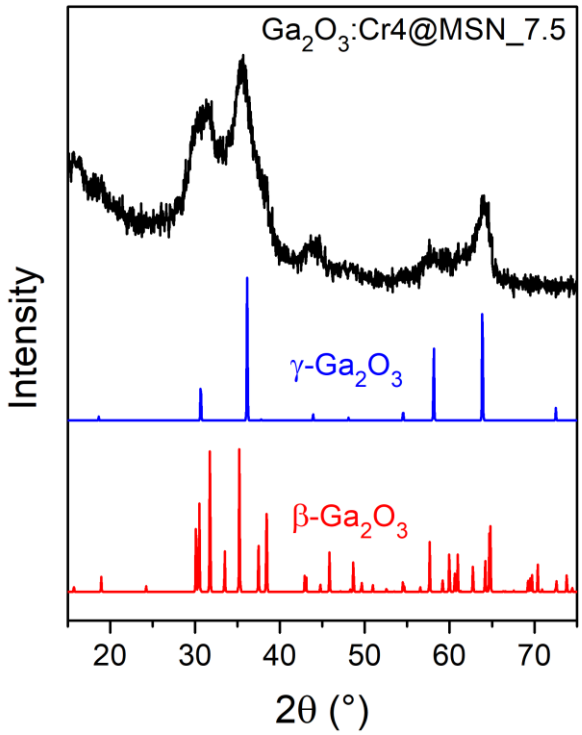

Figure 3.27: Ga_2O_3:Cr4@MSN_7.5 etched

Figure 3.27 further confirms the fact that the gamma phase has been stabilized. Comparing the signal of the sample with the characteristic peaks of the β and γ phases, it seems easier to assign the signals centred at about 31° and 37° with the two peaks of the γ-phase.
From the clear distinction and from the ratio between the signals at about 57° and 64°, they are more easily assigned to the γ-phase; finally, the absence of clearly distinguishable signals around 70° and beyond (characteristic only of the β-phase and which should be comparable with that at 64°) leads to the conclusion that there is no β-phase in the sample.

After this last test, the correlation between the γ-phase and the sample is evident and allows to assign the phase with definitive certainty for this system stabilized at 900°C. The quantum confinement effect into the 7.5 nm pore allows to stabilize the higher symmetric γ-Ga_2O_3 phase, in agreement with the general effect of stabilization of the high symmetry phase already noted on other systems such as $BaTiO_3$ [140], $NaNbO_3$ [141] and ZrO_2 [142].

Summarizing what has been observed so far, it seems that pore sizes of at least 7.5 nm and higher temperatures are required to stabilize the γ-phase rather than the β and α. The confirmation of the γ-phase synthesis took place combining XRPD measurements (in particular on the sample that has undergone a silica etching treatment, Figure 3.27) and PL/PLE analyses, showing patterns and spectral shapes completely different from those of the other phases synthesized in nanometric dimensions and bulk. The β-phase NPs MSN_4.2 show a behaviour change with respect to the same phase obtained through SS-synthesis due to the effects of the size. One of these most evident variations, valid however for all synthesized NPs, is the value of 10*Dq* which is always greater than that reported in the literature [83] suggesting a certain degree of tension into the NPs.

Typical literature examples of PL/PLE spectra are reported in the following graphs to compare them with those of a representative sample chosen from the synthesized NPs.

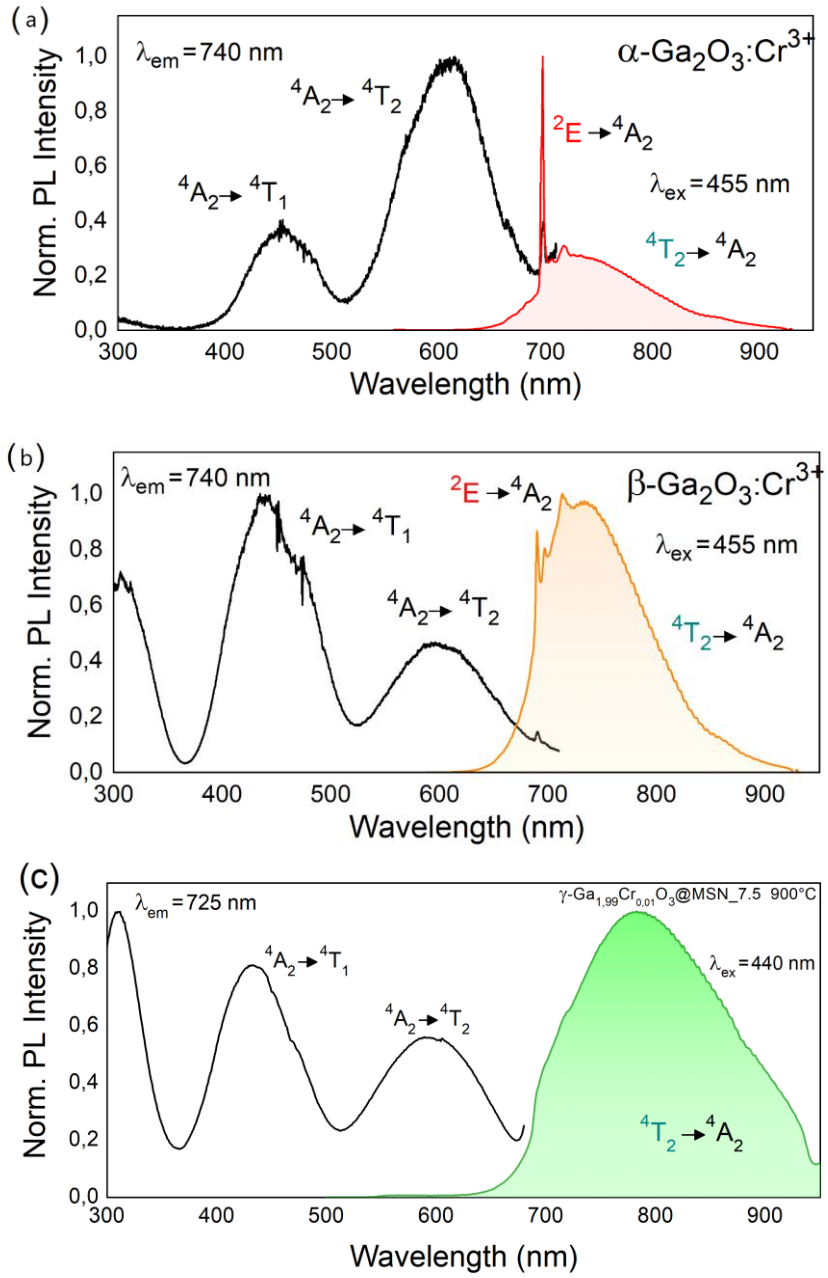

Figure 3.28: PL/PLE spectra of (a) α-Ga_2O_3:Cr^{3+} obtained from SS-synthesis [83]; (b) β-Ga_2O_3:Cr^{3+} obtained from SS-synthesis [83]; (c) γ-Ga_2O_3:Cr^{3+}@MSN_7.5 with 0.5% of chromium content, treated at 900°C.

Table 3.11: Reference values for α and β-phases [83] and values calculated for γ-Ga_2O_3:Cr^{3+}@MSN_7.5 with 0.5% of chromium content, treated at 900°C.

Phase	*B* (cm^{-1})	*C* (cm^{-1})	*Dq/B*	*C/B*	10*Dq* (cm^{-1})	<Ga-O> (Å)
α	552	3382	2.97	6.13	16393	1.999
β	641	3187	2.58	4.97	16529	2.012
γ	*580*	*3317*	*2.90*	*5.72*	*16835*	2.060*

** = value taken from (ICSD #152085).*

The values for γ-Ga_2O_3:Cr^{3+}@MSN_7.5 shown in Table 3.11 must be interpreted carefully: various difficulties have arisen in making reliable measurements on the spectra due to the difficulty of distinguishing any peaks that contribute to $^4A_2 \rightarrow {}^4T_1$ absorption. Here, it was decided to measure the centre of the $^4A_2 \rightarrow {}^4T_1$ band at half height to be used for the calculation of Racah parameter *B*. For the calculation of Racah parameter *C* it was also taken an assumption: as seen in equation (3), the $^4A_2 \rightarrow {}^2E$ energy value is necessary for the count, but this transition is not visible in the γ-Ga_2O_3 spectra. It was found [83] that both α and β phases' $^4A_2 \rightarrow {}^2E$ transition energy is 14343 cm^{-1}; so we decided to assume this value also for the γ-phase NPs.
It is estimated that the greatest error in the calculations is due to the influence of the more uncertain parameter *B* resulting from the ambiguous values of the $^4T_1$ absorptions: carrying out the calculations to obtain the Racah parameter *B* (equation (2)), a small discrepancy in the wavelength value is sufficient to obtain a large difference in the result. In this case, the *C/B* ratio could allow to understand the reliability of the calculations: a too high value compared to the literature references is a clear index of the error due to the measurement of the $^4A_2 \rightarrow {}^4T_1$ band centre, which invalidates all subsequent calculations.

Observing the three graphs in Figure 3.28, the evident differences in the spectral shape of the PL are noted: proceeding from the α-phase towards the γ-phase, the transition $^4T_2 \rightarrow {}^4A_2$ increases in intensity with respect to the $^2E \rightarrow {}^4A_2$ and moves to longer wavelengths, consistently with the weaker crystal field shift hypotheses. As for the PLE, the intensity ratios between the two transitions $^4A_2 \rightarrow {}^4T_2$ and $^4A_2 \rightarrow {}^4T_1$ changes. Regarding the positions of the bands in PLE, better observations can be made by observing Table 3.11. From $^4A_2 \rightarrow {}^4T_2$ we obtain the 10*Dq* value without equivocation, from which it can be noted that the crystal field increases in strength towards the γ-phase. This is counterintuitive: from the bond distances progressively increasing from the α-phase towards the γ-phase, it's more logic to hypothesize the opposite: at greater distances correspond crystal fields of lower intensity. *Dq/B* instead shows a different trend for the three polymorphs, but since *C/B* of the γ-phase is quite different from the value of both the α and β phases, it becomes difficult to make any considerations. Observing the two specific Tanabe-Sugano diagrams for the α and β phases obtained by Back *et al*. [83] reported in Figure 3.29 below, the *C/B* value of the γ-phase should allow us to imagine an intermediate situation between the other two. Therefore, given its *Dq/B* value closer to that of the α-phase, it could be concluded that the γ-phase is at intermediate values of crystal field as a consequence of the effects occurring at nanometric dimensions. However, the considerations regarding everything that affects these values would make the interpretation much more complex, especially considering that our assumptions for the γ-phase regarding the calculation of *B* and *C* are poorly reliable at this stage.

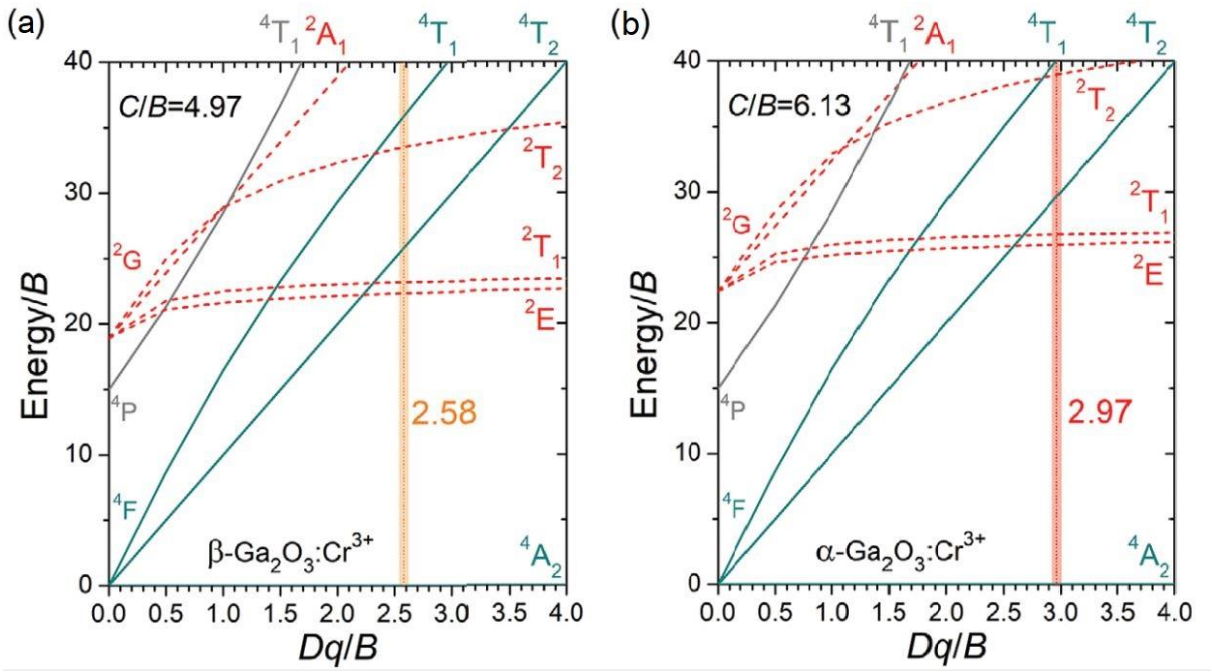

Figure 3.29: Tanabe–Sugano diagrams for Cr^{3+} in β-Ga_2O_3 (a) and α-Ga_2O_3 (b) polymorphs [83].

3.7 Effect of particle size on γ-Ga_2O_3 stabilization

In this section, the effect of the pore size of the MSNs in which Ga_2O_3:Cr^{3+} NCs were synthesized is summarized and discussed. For the smallest NPs employed (MSN_3.1) a new sample was synthesized and treated at 900°C, in order to have comparable conditions. In addition, two new SBA-15 samples with enlarged pores obtained by means of a swelling agent were prepared. These new synthesis were done by adding trimethylbenzene (TMB) before adding TEOS, in weight ratio Pluronic123:TMB = 1:0.3 for sample MSN_13.5 and ratio 1:0.5 for sample MSN_22.4.
All the samples were doped with 0.5% of chromium and treated at 900°C.

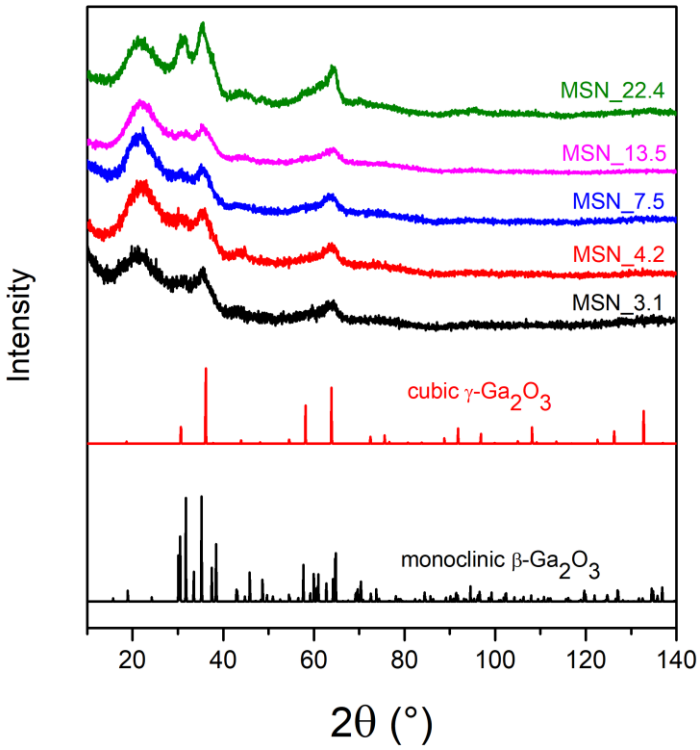

Figure 3.30: XRPD graphs of all particles at various pore sizes, with chromium content fixed to 0.5% and treated at 900°C.

XRPD patterns in Figure 3.30 do not allow to draw conclusions: as in the previous circumstances, they show themselves too similar to each other and so it's difficult to notice clear differences allowing to distinguish the phases. However, the greater intensity in the MSN_22.4 sample of the characteristic peaks of NCs compared to the silica pattern is evident: the large increase in pore volume leads to a greater presence of Ga_2O_3 in silica.

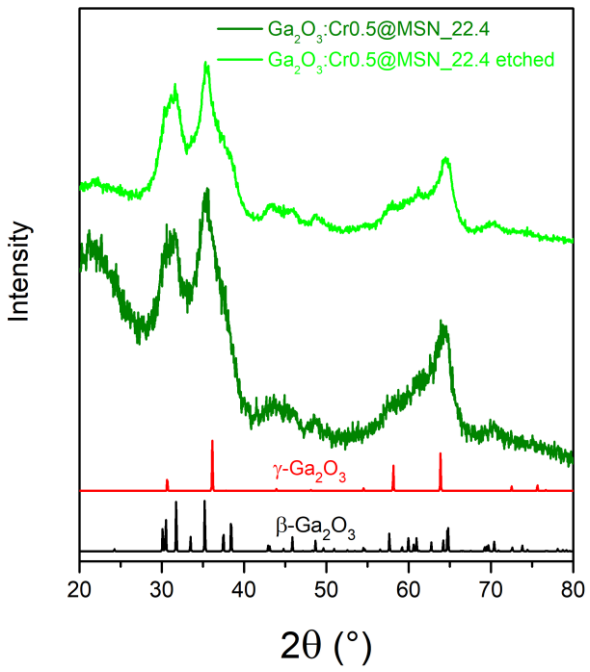

Figure 3.31: Ga_2O_3:Cr0.5@MSN_22.4 etched

At 22 nm of pore size, characteristic peaks of β-phase are again visible in the diffraction spectrum. This is particularly evident observing the pattern obtained after silica etching in Figure 3.31: the shoulder around 39°, peaks at 43°, 46°, 49° and those at 60° and 70° are particularly identifying. Despite this, γ-phase cannot be excluded from the analysis, especially by looking at the higher intensity of the peak at 64° with respect to that of the peak at 58°. At this size, pores are now sufficiently large to no longer allow quantum confinement, so gallia reappears in the most stable phase.

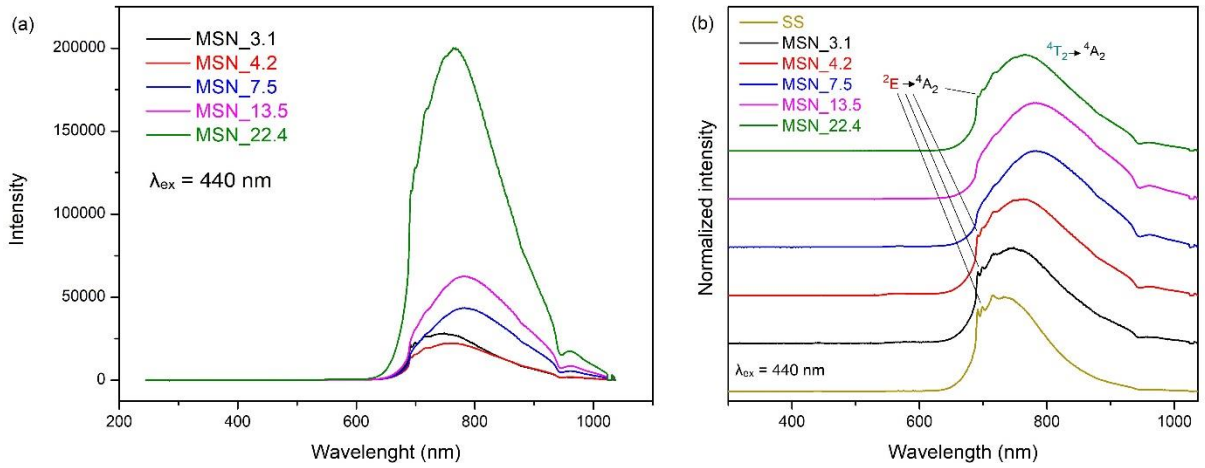

Figure 3.32: (a) PL emission spectra of all particles at various pore sizes, with chromium content fixed to 0.5% and treated at 900°C. (b): The previous spectra normalized, with transition signed.

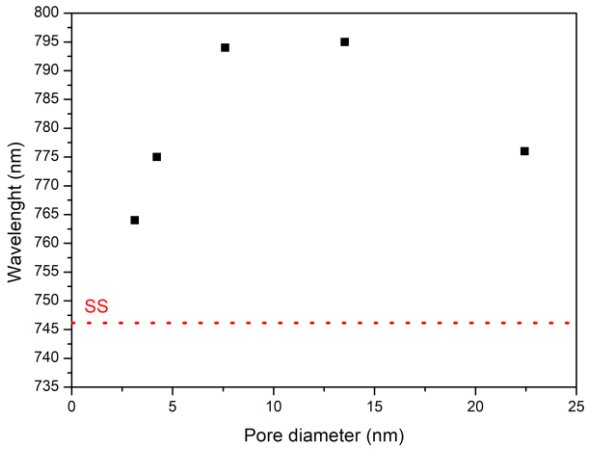

Figure 3.33: $^4T_2 \rightarrow {}^4A_2$ band centre of MSN at various pore sizes, with chromium content fixed at 0.5% and all treated at 900°C. The red dot line is the SS value reference. The centre was measured in the width at half height.

Table 3.12: $^4T_2 \rightarrow {}^4A_2$ band centre of MSN_7.5 at various pore sizes, with chromium content fixed at 0.5% and all treated at 900°C.

Pore size	Wavelength (nm)
SS	747
MSN_3.1	764
MSN_4.2	775
MSN_7.5	794
MSN_13.5	795
MSN_22.4	776

The XRPD patterns discussion is confirmed by the spectroscopic investigation. Comparing the PL spectra in Figure 3.32 (a), the increasing intensity effect due to the size of the NCs remains confirmed, excluding from this comparison the MSN_3.1 particles.
Comparing the spectral shapes with each other (Figure 3.32 (b)), the results already noted in the previous chapters reappear: at 3 nm and 4 nm pore size the spectral shape is typical of the β-phase. The curve for MSN_3.1 appears almost perfectly corresponding to that of the solid state synthesis and this could be a further proof that some crystals have not been confined within the pores. The MSN_4.2 sample shows a shift towards weaker crystal fields and the shape begins to undergo a variation that tends towards that of the γ-phase, and could be a mixed with the β-phase. The MSN_7.5 and MSN_13.5 samples are characterized by a spectral shape completely different from the previous ones, due to the different phase that has been stabilized: the γ-phase. It is interesting to note that the spectral shape of these two samples are exactly matching, giving not only a further proof of the pure γ-phase stabilized, but also indicating how in this size range the system is perfectly within the confinement range for the stabilization of this phase. Their broadband centre is almost at the same wavelength and beyond that, their wavelength is the highest of all samples (Figure 3.33 and Table 3.12): this is in line with the expectations of having stabilized the phase with a larger average <Ga-O> bond length and therefore with weaker crystal field. Finally, the particles with the largest pores show a spectral shape that tends to return to the β-phase, though not being coincident with it. It is possible that at this dimension (about 22 nm) the quantum confinement necessary for the stabilization of the γ-phase alone is lacking and the system appears as a mix between γ and β phases.

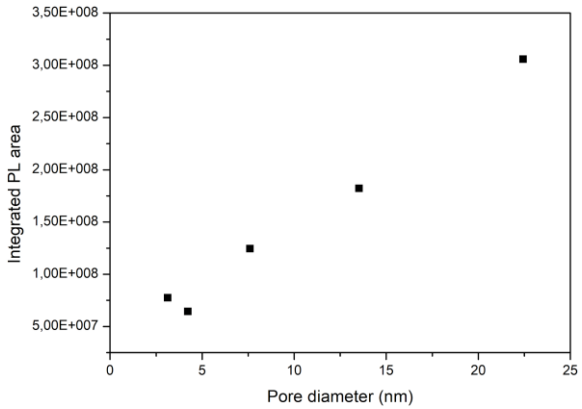

Figure 3.34: PL integrated area graph for various pore sizes, at 0.5% of chromium content and treated at 900°C. To make comparable the value for the last point for the MSN_22.4 sample, it has been divided for 1.8 due to the almost double value of specific pore volume (see Table 3.1): by loading the sample holder of the spectrofluorometer with the same amount of material, the actual quantity of NCs inside the pores is consequently double, resulting in a double intensity in emission (as can be seen in Figure 3.32 (a)).

Plotting the area subtended by the emission curves in Figure 3.34, a trend between size and emitted photons appears to be linear. It's however necessary to remember that the MSN_3.1 sample has probably undergone a partial synthesis outside the silica pores, so it cannot be compared with the other particles. The fact that the photoluminescence intensity is greater than that of the MSN_4.2 sample, which also has a larger pore volume to contain more NCs, is a further confirmation.

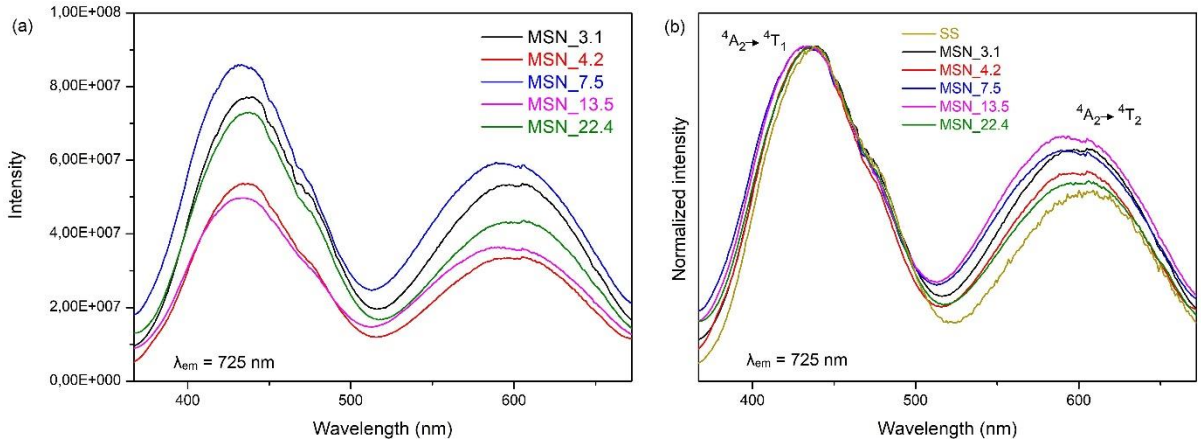

Figure 3.35: (a) PLE spectra of all particles at various pore sizes, with chromium content fixed to 0.5% and treated at 900°C. (b): The previous spectra normalized, with transitions signed.

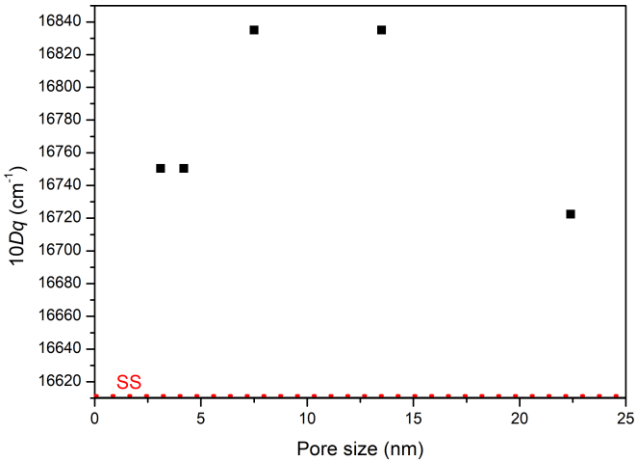

Figure 3.36: 10Dq values of MSN at various pore sizes, with chromium content fixed at 0.5% and all treated at 900°C. The red dot line is the SS value reference.

Table 3.13: $^4A_2 \rightarrow {}^4T_2$ band centre of MSN at various pore sizes and their 10Dq, with chromium content fixed at 0.5% and all treated at 900°C.

Pore size	**Wavelength (nm)**	**10*Dq* (cm^{-1})**
SS	602	16611
MSN_3.1	597	16750
MSN_4.2	597	16750
MSN_7.5	594	16835
MSN_13.5	594	16835
MSN_22.4	598	16722

The 10*Dq* trend (Figure 3.36 and Table 3.13) calculated by the PLE spectra shows an unexpected behaviour of the NPs: MSN_7.5 and MSN_13.5, within which γ-phase has been stabilized, revel the highest crystal field values. This is in contrast with the predictions of having obtained the phase with the greatest bond distances and consequently with the weakest crystal fields; however, in order to better understand the phenomena that influence the photoluminescence of these nanomaterials, further investigations would be necessary to evaluate how the Cr^{3+} is arranged in the different coordination sites and what effect this produces.

EDX analyses implemented in the SEM were carried out to map the distribution of elements in the samples. No samples evidenced the growth of Ga_2O_3 outside the pores but for an unequivocal confirmation TEM analysis are necessary. The maps for the sample MSN_7.5 with 0.5% Cr and treated at 900°C are reported as an example in figures 3.37 and 3.38.

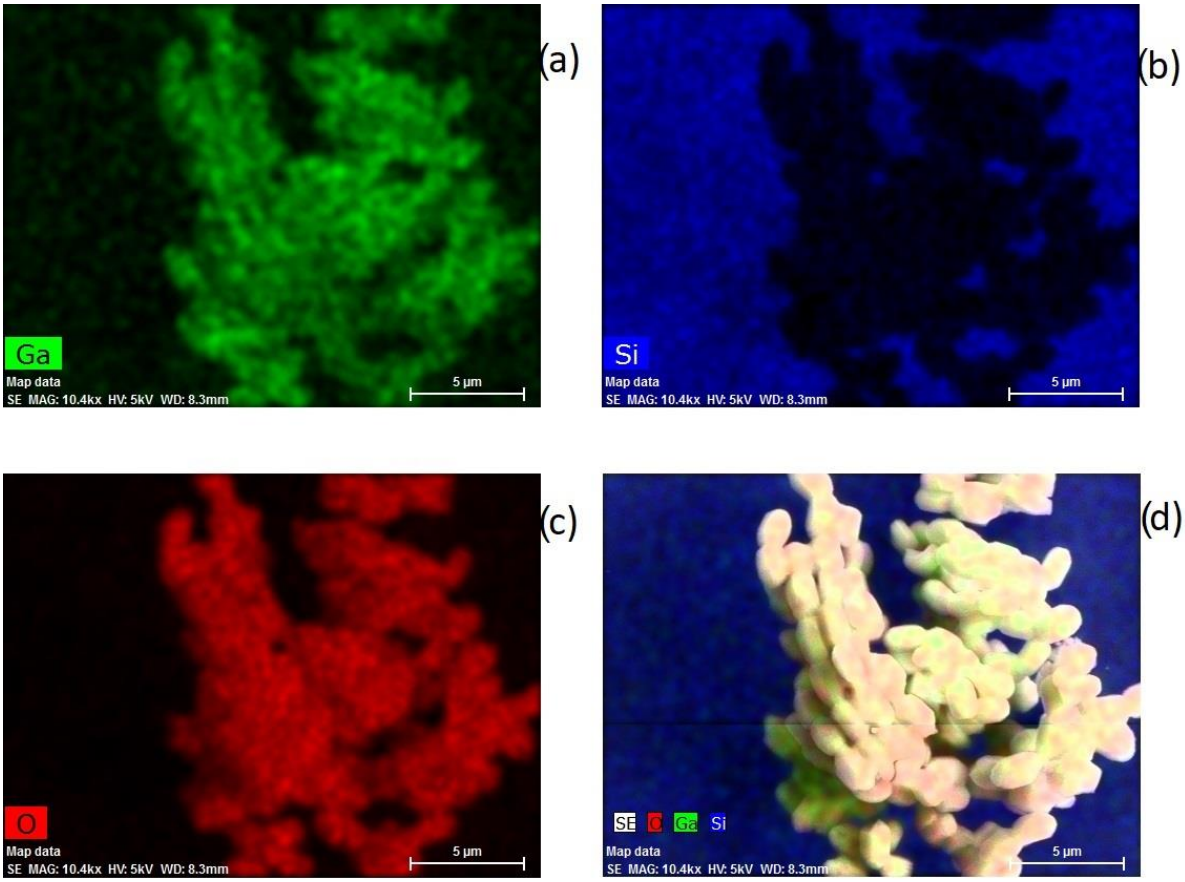

Figure 3.37: EDX image of MSN_7.5 with 0.5% Cr and treated at 900°C showing (a) gallium; (b) silicon (as the stab in which the sample was put is of metallic silicon, the silicon of MSNs is seen by negative due to the relative low concentration in the NPs' area); (c) oxygen and (d) all the elements overlapped.

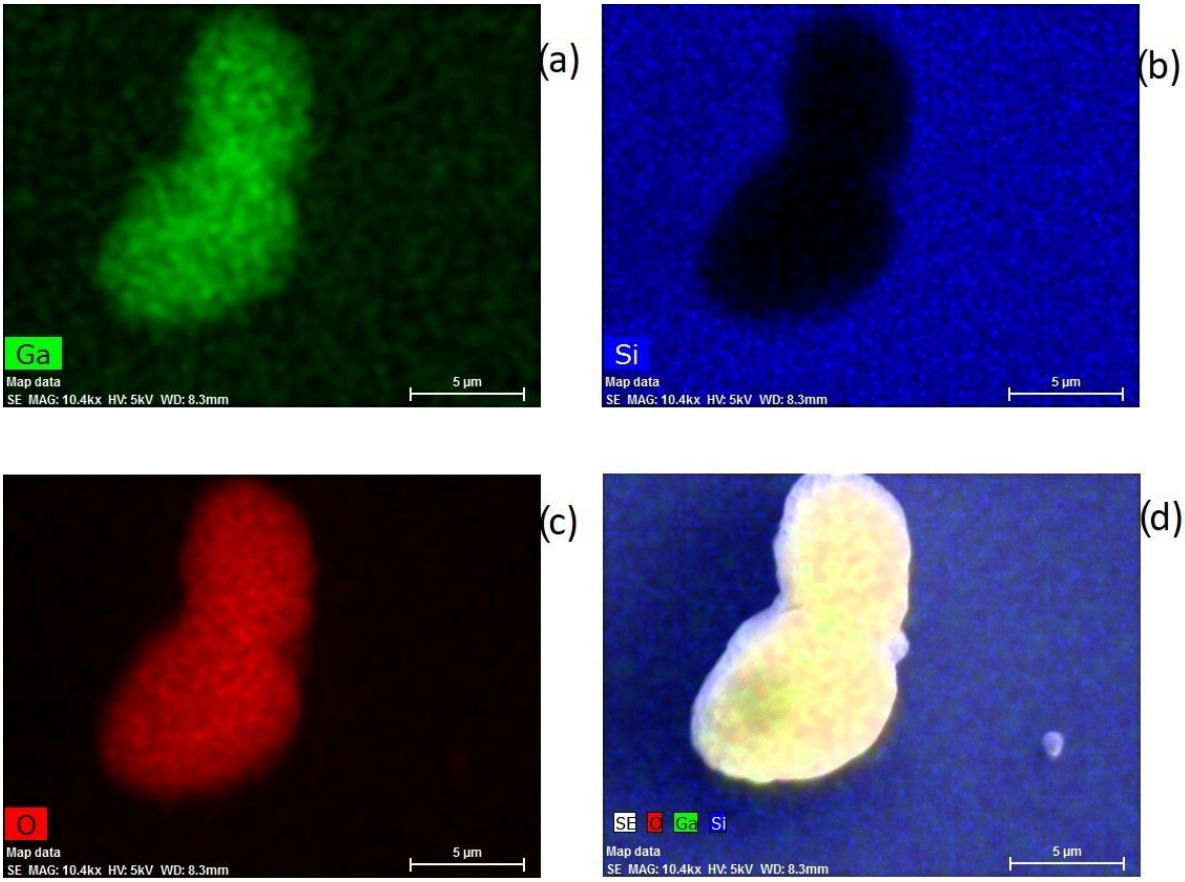

Figure 3.38: EDX image of two isolated particles of MSN_7.5 with 0.5% Cr and treated at 900°C showing (a) gallium; (b) silicon (as the stab in which the sample was put is of metallic silicon, the silicon of MSNs is seen by negative due to the relative low concentration in the NPs' area); (c) oxygen and (d) all the elements overlapped.

All the observations made are summarized in figure 3.39.

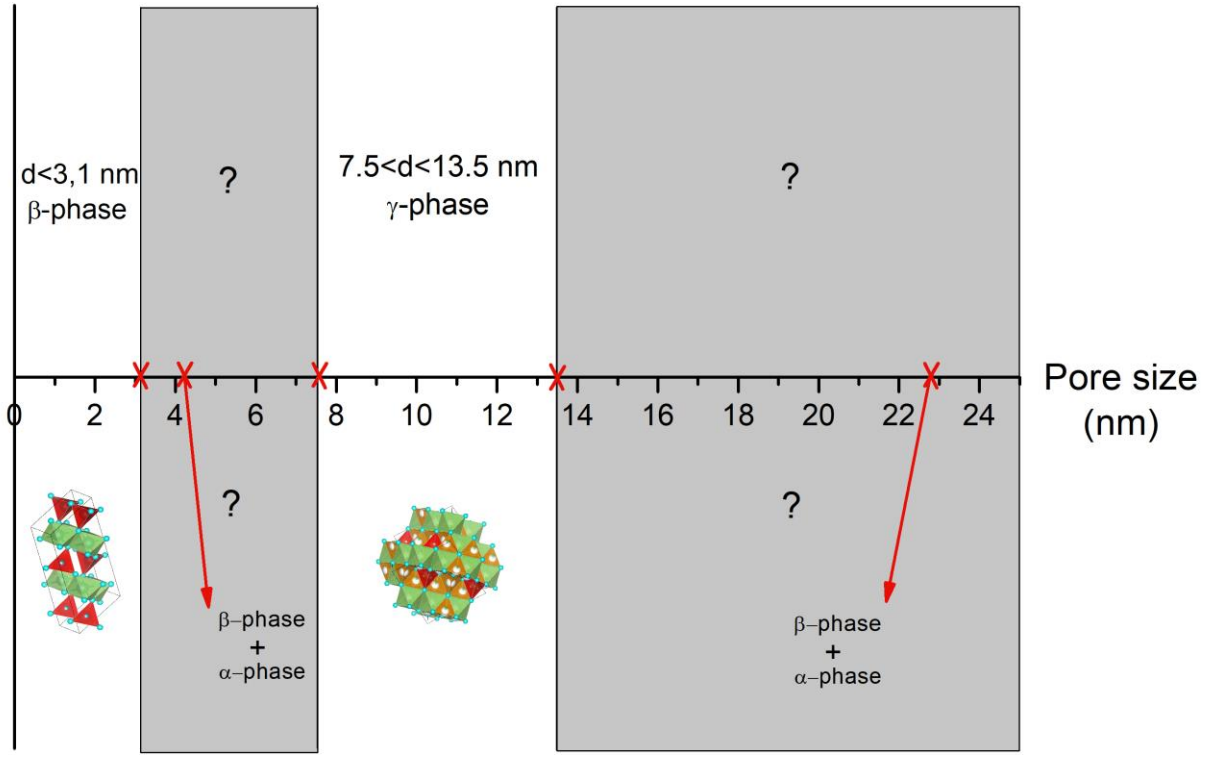

Figure 3.39: Schematic representation of the effects of quantum confinement for particles treated at 900°C.

At this point we can draw some conclusions: for particle size lower than about 22.4 nm, the size confinement allows to stabilize the Ga_2O_3 polymorph with higher symmetry, the γ-phase. This effect was also demonstrated for other systems such as, for example, $BaTiO_3$ [140], $NaNbO_3$ [141] and ZrO_2 [142]. The counterintuitive fact that this confinement effect disappears when a smaller size than about 4.2 nm is reached could be explained in terms of thermal expansion coefficients. In fact, Ga_2O_3 and amorphous SiO_2 are characterized by different thermal expansion coefficients. From the various studies carried out on these compounds [143-146] it emerges that amorphous silica has a thermal expansion coefficient (TEC) definitely lower than that of gallia: Anagnostopoulos [143] and Kaliannan [144] calculated a value of TEC for silica around $0.5*10^{-6}$ K^{-1}; Cheng [145] and Liao [146] found very different value for gallia. Both calculated the TEC for the three cell parameters *a, b* and *c* but while Cheng reported values around $1.7*10^{-6}$ K^{-1}, Liao reported values between $6*10^{-6}$ K^{-1} and $7.8*10^{-6}$ K^{-1}. Despite the discrepancy in values, there is no doubt that the TEC of gallia is higher than that of silica. We hypothesized that in the heating and subsequent cooling steps during the heat treatment of the sample, the small Ga_2O_3 NPs (of about 3.1 nm) undergo a large stress, probably a stretching effect, stimulated by the high surface due to the very different thermal expansion coefficient with respect to the embedding silica. The result could be that the NPs are stretched inside the tubular pores, returning them to a tensioned β-phase supported only by dimensional confinement within the silica walls. One method that could be used to verify this is a TEM analysis before and after etching the silica. In this way it could be verified that, once free from confinement, the particles release the tensions and would re-stabilize in the more symmetrical phase that they would tend to maintain at those dimensions.

3.8 Effect of Ga^{3+} substitution by Al^{3+}

With the aim of investigating the effects of the progressive substitution of gallium with aluminium on the crystal field of the host and, therefore, analysing the effect on the Cr^{3+} electronic state, studies were carried out on synthesized particles by keeping the NPs size (MSN_7.5), chromium concentration fixed to 1% and thermal treatment at 900°C. Four different Al percentages were investigated (5, 25, 50 and 75%) in addition to the sample already studied at 1% of chromium without aluminium, used as a reference.

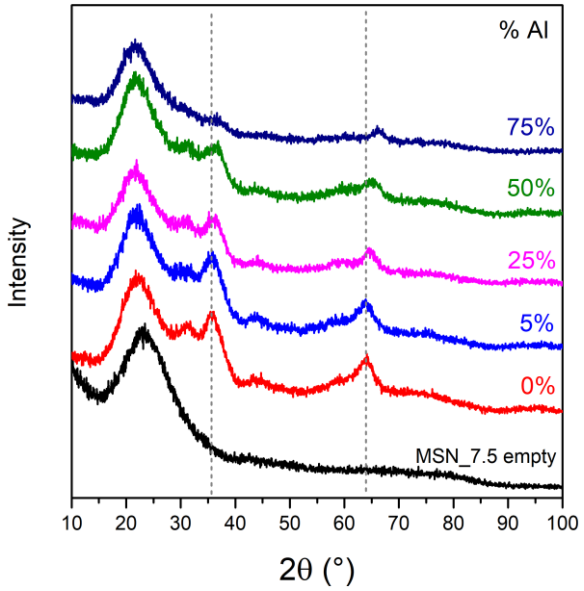

Figure 3.40: XRPD graphs of MSN_7.5 at various Al percentages, with chromium content fixed to 0.5% and treated at 900°C.

The first X-ray observations (Figure 3.40) already reveal a slight but progressive shift of bands at 36° and 64° towards higher angles, as well as a flattening of their intensity. The displacement at greater angles corresponds to a decrease in the cell size, which is consistent with the progressive replacement of gallium with a smaller atom such as aluminium (ionic radius of 0.62 Å for Ga^{3+} and 0.535 Å for Al^{3+} [147]). All systems are still identified as γ-phase. Photoluminescence analysis offers additional information to understand the effects of specific compositions.

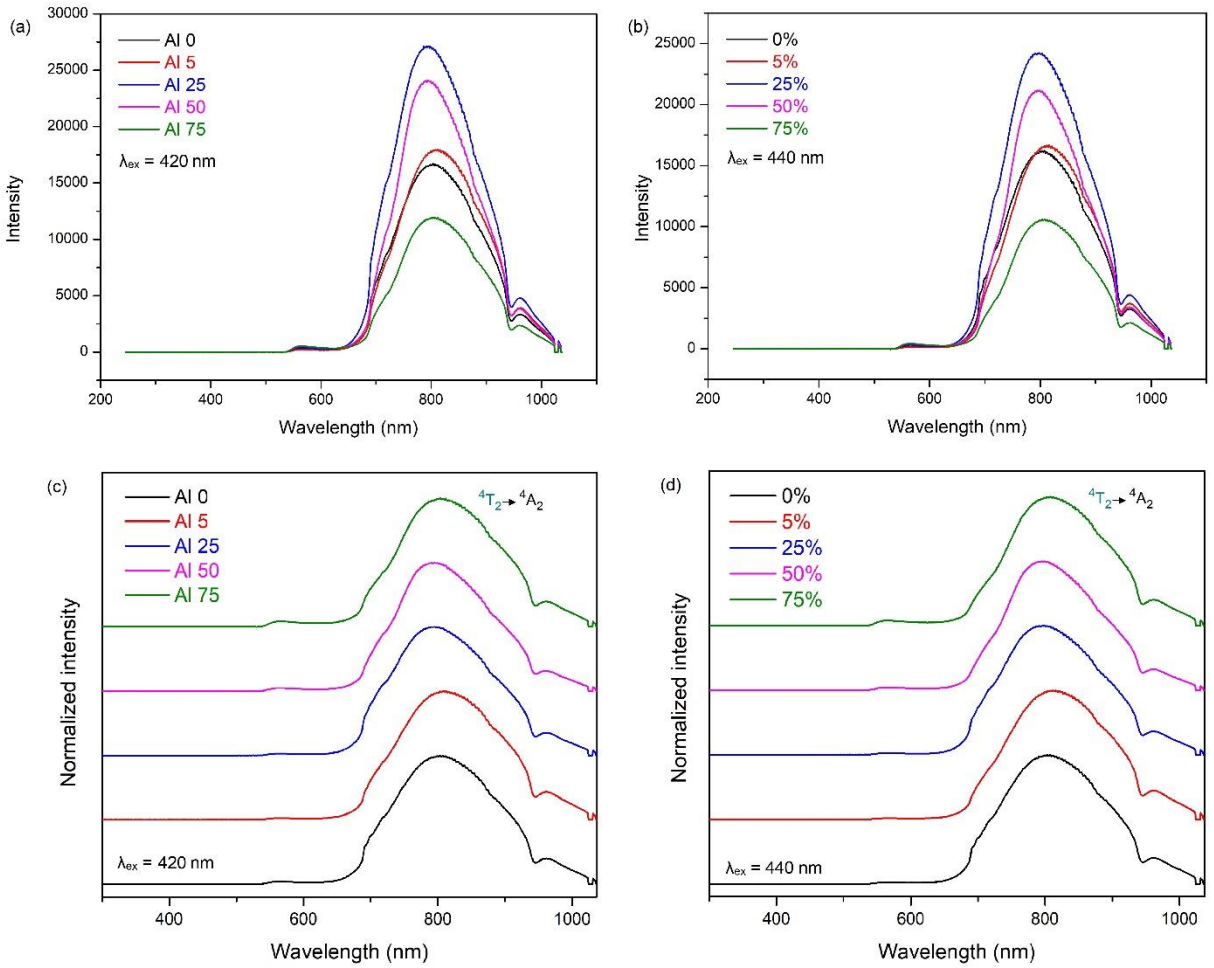

Figure 3.41: PL emission spectra of MSN_7.5 at various Al percentages, with chromium content fixed to 0.5%, treated at 900°C and at (a) λ_{exc} = 420 nm, (b) λ_{exc} = 440 nm. (c) and (d): The previous spectra respectively at λ_{exc} = 420 nm and λ_{exc} = 440 nm, normalized, with transition signed.

For each composition, analyses were carried out by exciting at various wavelengths. In addition to the reference at 440 nm, the graphs relating to the excitation wavelength for which the greatest emission was measured (λ = 420 nm) are shown in Figure 3.41.
From the PLE spectra in Figure 3.43 and the PL integrated areas in figure 3.42, it is evident that by centring this range at 420 nm and 440 nm, the first of the two intervals allows to irradiate the sample with the greatest amount of exciting radiation, which leads to higher PL emission.
In order to better compare the effect of aluminium on the intensity for both emission wavelengths, the plot of the integration areas is shown in Figure 3.42.

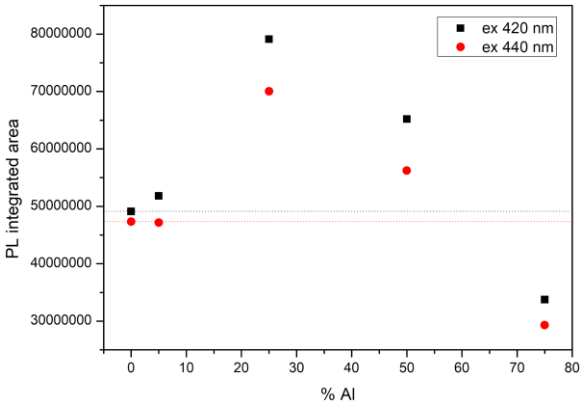

Figure 3.42: PL integrated area graph of MSN_7.5 at various Al percentages, with chromium content fixed to 0.5% and treated at 900°C.

From the PL integrated areas emerges a tendency for aluminium to increase the system's emission. An amount of 5% still does not seem to significantly increase the emission, while the composition at 25% is identified as the best emitting sample. At 50% the intensity emitted already decreases and the minimum is reached at 75% of Al.

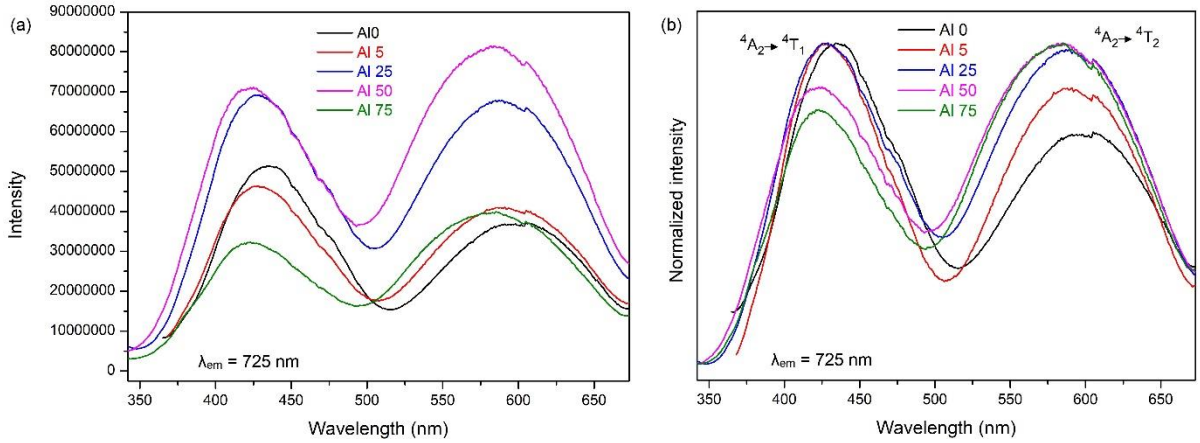

Figure 3.43: (a) PLE spectra of MSN_7.5 at various Al percentages, with chromium content fixed to 0.5% and treated at 900°C. (b): The previous spectra normalized, with transitions signed.

Table 3.14: 10Dq parameter for NCs@MSN_7.5 at various Al percentages, with chromium content fixed to 0.5% and treated at 900°C.

Sample (Al %)	**0**	**5**	**25**	**50**	**75**
10*Dq* (cm^{-1})	16750	16892	17036	17182	17153

From Figure 3.43 it is clear that a progressive change of the $^4A_2 \rightarrow {}^4T_2$ transition position can be observed as the increasing of Al. The values of the crystal field strength (10*Dq*) increase with increasing Al content up to a maximum reached at the composition of 50% of Al, then begin to decrease as shown in Table 3.14 and Figure 3.44.

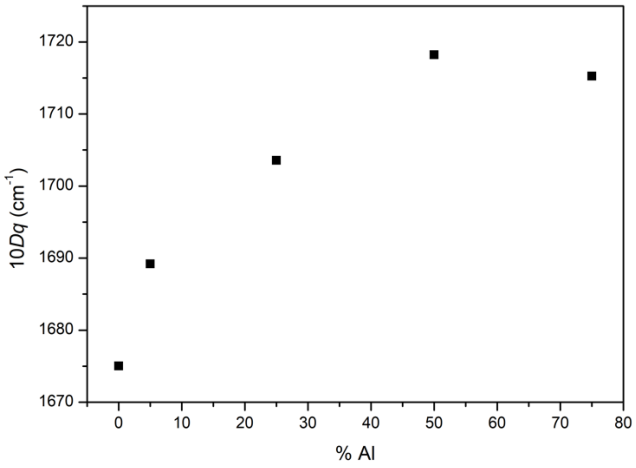

Figure 3.44: 10Dq values vs Al percentage.

As for the different chromium concentrations in Chapter 3.3, the different aluminium concentrations bring a variation in the relative intensity of the absorption bands. There is a regular and progressive trend in the ratio between the intensities of the two transitions: the excitation $^4A_2 \rightarrow {}^4T_2$ increases while the $^4A_2 \rightarrow {}^4T_1$ decreases (Figure 3.43 (b)). As already mentioned for the same effect due to temperature, this change could be linked to the Racah parameter B, regarding the covalent and ionic components of bonds between atoms. A variation of this factor is consistent with the progressive replacement of gallium atoms with aluminium, less electronegative, whose electrons have a different capacity of sharing in bonds with oxygen. Altering in this way the whole crystalline system, sites replaced by chromium are affected too. The plot resulting from the ratio $(^4A_2 \rightarrow {}^4T_2)/(^4A_2 \rightarrow {}^4T_1)$ is shown in Figure 3.45.

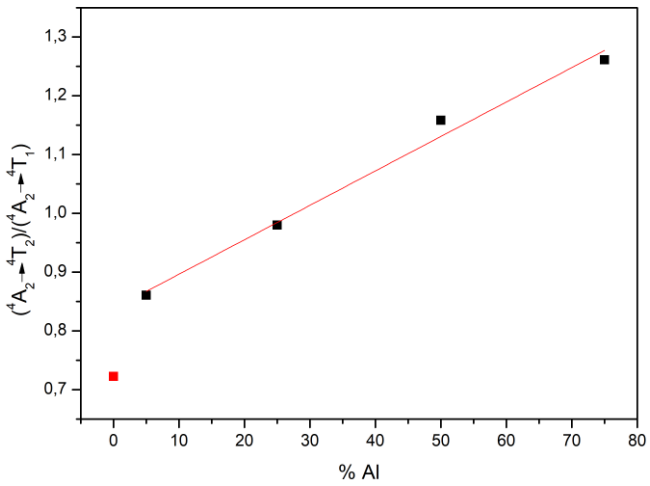

Figure 3.45: ratio $(^4A_2 \rightarrow {}^4T_2)/(^4A_2 \rightarrow {}^4T_1)$ of MSN_7.5 at various Al percentages, treated at 900°C.

Another effect caused by aluminium is to move both the centres of absorption bands and the centre of emission band. These effects are clearly seen in PL and PLE graphs; the consequent bands' energy are shown in figures 3.46 for a direct comparison.

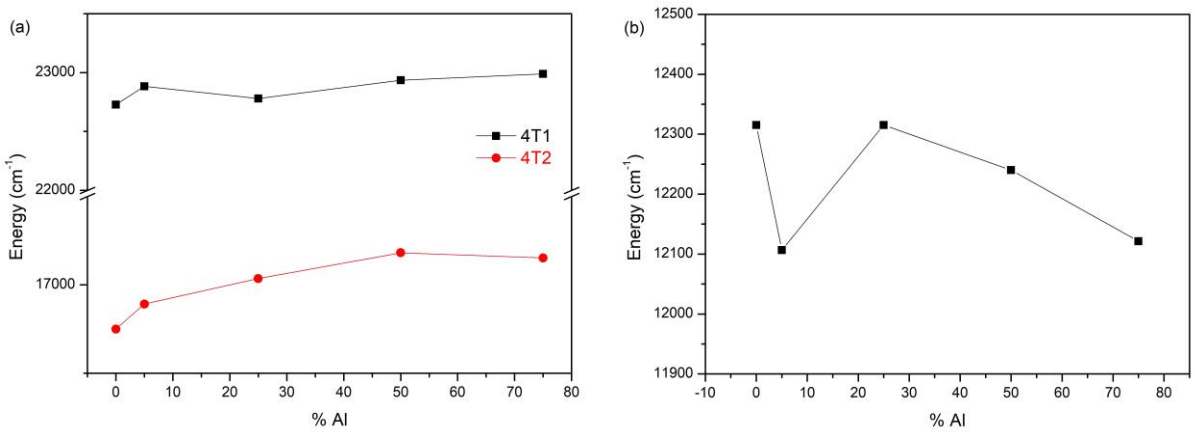

Figure 3.46 (a): $^4A_2 \rightarrow {}^4T_1$ energy and $^4A_2 \rightarrow {}^4T_2$ energy vs Al percentage. (b): $^4T_2 \rightarrow {}^4A_2$ energy vs Al percentage.

Focusing on the trend of the $^4A_2 \rightarrow {}^4T_2$ centre (Figure 3.46 (a)), the system moves towards shorter wavelengths as aluminium increases. In terms of energy this means that the excitation energy for that transition increases and therefore its energy level in the CCD rises. At the same time, considering the three aluminium concentrations 25%, 50% and 75% (excluding by the moment the 5% one), the opposite trend is observed in emission (Figure 3.46 (b)): the $^4T_2 \rightarrow {}^4A_2$ centre moves to longer wavelengths, i.e. the energy emission decreases. This means that in the CCD, simultaneously with an upward shift, the excited level $^4T_2$ shifts to the right along the configurational coordinate Q (Figure 3.47). Consequently, the Stokes shift increases.

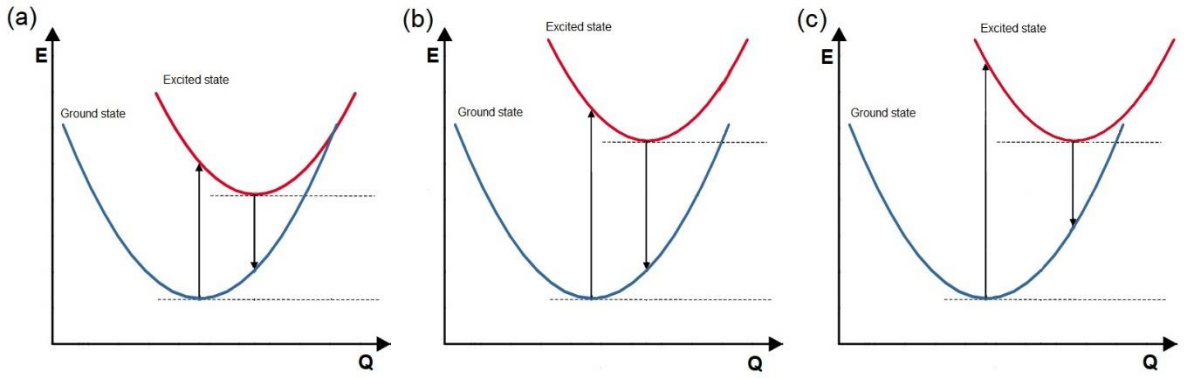

Figure 3.47: Schematic representation with CCDs of Ga-Al system behaviour. (a): The starting situation at 0% of Al. (b) Example of excited state rising in energy: as the excitation energy increase, so does the emission. To have a decrease in energy for the emission while the excitation still increase (with respect to the initial situation (a)), the excited state have to shift on the right (c).

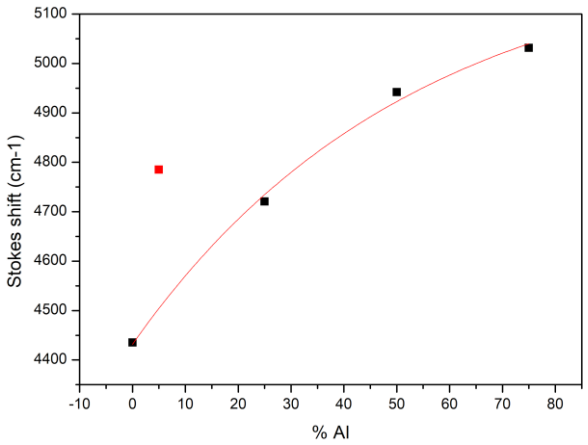

Figure 3.48: Stokes shift vs Al percentage. The red dot represents the value for 5% Al composition.

The importance of this feature is found in thermally activated cross over studies, in which the energy levels proximity facilitates a non-radiative decay process to the ground state due to the effect of temperature [148]. This effect could help explain the progressive lowering of the samples' emission intensity.

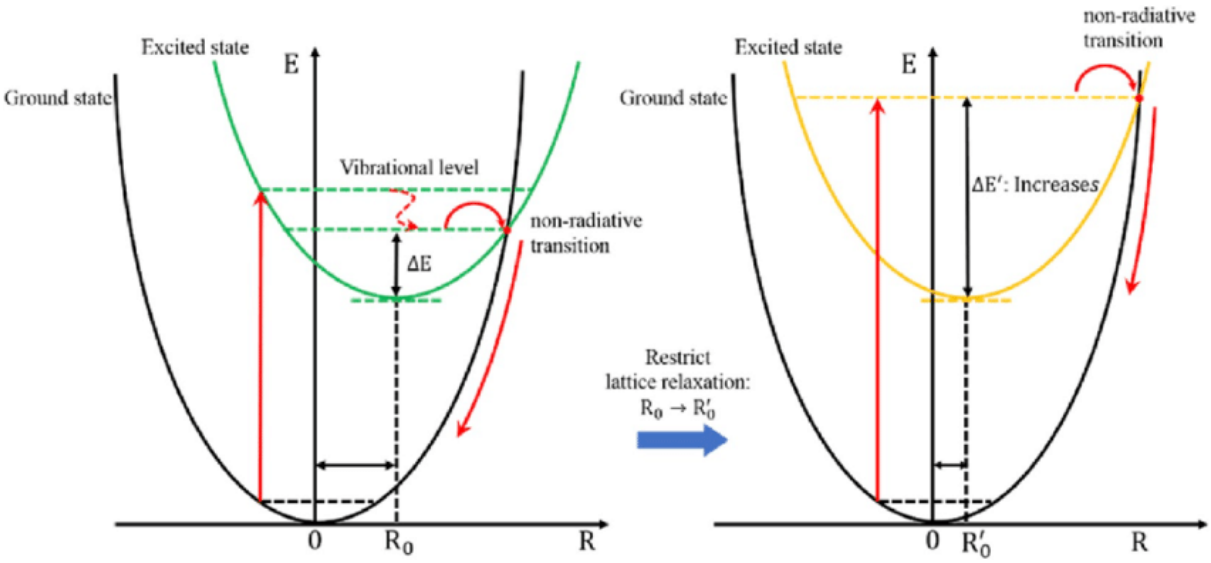

Figure 3.49: Schematic representation of thermal quenching process in CCD [149].

4. Conclusions

The effects of nanoparticles' size, heat treatment temperature and percentage of chromium on the phase stabilization of β and γ-Ga_2O_3 were investigated by means of BET/BJH, SEM, XRPD and PL/PLE analyses.

The results made it possible to ascertain the stabilization of the more symmetrical cubic phase at a temperature in which it is not normally stabilized. The key parameter enabling this is the size of the pores into which Ga_2O_3 is synthesized. Specifically, between 7.5 nm and 13.5 nm only the γ-phase is present, while from 4.2 nm and 22.4 nm it is present in the mix together with the β-phase.

Below 4.2 nm the system counterintuitively re-establishes itself in the β-phase. The hypotheses for which this occurs due to tension and stretching effects must be further investigated through pre and post silica-etching investigations.

The results demonstrated that a ratiometric optical thermometer based on chromium doped gallium oxide in nanometric dimensions between 7.5 and 25 nm was not possible due to the absence of the $^2E \rightarrow {}^4A_2$ transition at room temperature. The systems under 4.2 nm show it, but they should be investigated at low temperatures. Despite this, the usefulness of chromium as a probe for investigating the phase of the Ga_2O_3 system has been verified. As the chromium concentration varied, a linearity was also found in the variation of the intensity ratio $(^4A_2 \rightarrow {}^4T_2)/(^4A_2 \rightarrow {}^4T_1)$.

The crystal field variation was then studied at the progressive substitution of gallium by aluminium.

A linear trend between the intensity ratio of the two excitation bands $(^4A_2 \rightarrow {}^4T_2)/(^4A_2 \rightarrow {}^4T_1)$ and the chemical composition of the mixed oxide Ga-Al was also observed for the $Ga_{2-x}Al_xO_3:Cr^{3+}$ system. This observation is still under investigation.

The $Ga_{2-x}Al_xO_3:Cr^{3+}$ system showed also a relationship between the Stokes-shift and the composition, an interesting effect for further thermally activated cross over studies.

The unprecedent investigation of Cr^{3+} in the cubic γ-Ga_2O_3 phase, even mixed with Al, suggested the potential of this system as phosphor in the field of near-infrared LEDs (NIR-LEDs).

Further investigations in the study of this system should be aimed at exploring the size ranges not investigated and the morphology of the particles through TEM analysis.

5. Bibliography

[1] T. Lanez, I.U. Khand, P.L. Pauson. Ferrocene derivatives. Part 24. Synthesis of dihydro-2-pyrindines and dihydro-3H-2-cyclopent[c]azepines by photolysis of their cyclopentadienyliron derivatives. *J. Chem. Soc. Perkin Trans.*, **1989**, *1*, 2075-2078.

[2] D.R. Vij. *Luminescence of Solid*. Springer-Verlag, **1998**.

[3] S. Kück. Laser-related spectroscopy of ion-doped crystals for tunable solid-state lasers. *Appl. Phys.* B, **2001**, *72*, 515–562.

[4] K.V.R. Murthy, H.S. Virk. Luminescence Phenomena: An Introduction. *Defect and Diffusion Forum* **2014**, *347*, 1-34.

[5] G. Blasse. Fluorescence of Niobium-Activated Antimonates and an Empirical Criterion for the Occurrence of Luminescence. *J. Chem. Phys.*, **1969**, *51*, 3529-353.

[6] J. M. Hollas, *Modern Spectroscopy, 4th edition*. Wiley, **2003**.

[7] G. Racah. Theory of complex spectra II. *Phys. Rev.*, **1942**, *62*, 438-462.

[8] Y. Tanabe, S. Sugano. On the absorption spectra of complex ions I. *J. Phys. Soc. Japan*. **1954**, *9,* 753–766.

[9] Y. Tanabe, S. Sugano. On the absorption spectra of complex ions II. *J. Phys. Soc. Japan*., **1954**, *9*, 766–779.

[10] M. G. Brik, S. J. Camardello, A. M. Srivastava, N. M. Avram, A. Suchocki. Spin-Forbidden Transitions in the Spectra of Transition Metal Ions and Nephelauxetic Effect. *J. Solid State Sci. Technol.*, **2016**, *5*, 3067-3077

[11] P. Atkins, T. Overton, J. Rourke, M. Weller, F. Armstrong, P. Salvador, M. Hagerman, T. Spiro, E. Stiefel. *Shriver & Atkins Inorganic Chemistry* (4th ed.). W.H. Freeman and Company, **2006**.

[12] B.E. Douglas, D.H. McDaniel, J.J. Alexander. *Concepts and Models of Inorganic Chemistry* (3rd ed.). John Wiley & Sons, **1994**.

[13] T.H. Maiman. Stimulated Optical Radiation in Ruby. *Nature*, **1960**, *187*, 493-494.

[14] J. Brübach, C. Pflitsch, A. Dreizler, B. Atakan. On surface temperature measurements with thermographic phosphors: a review. *Prog. Energy Combust*., **2013**, *39*, 37–60.

[15] B. Dong, B.S. Cao, Y.Y. He, Z. Liu, Z.P. Li, Z.Q. Feng. Temperature sensing and in vivo imaging by molybdenum sensitized visible upconversion luminescence of rare-earth oxides, *Adv. Mater*., **2012**, *24*, 1987–1993.

[16] X.Y. Li, G.C. Jiang, S.S. Zhou, X.T. Wei, Y.H. Chen, C.K. Duan, M. Yin. Luminescent properties of chromium(III)-doped lithium aluminate for temperature sensing. *Sens. Actuators B*, **2014**, *202*, 1065–1069.

[17] S. Jiang, P. Zeng, L.Q. Liao, S.F. Tian, H. Guo, Y.H. Chen, C.K. Duan, M. Yin. Optical thermometry based on upconverted luminescence in transparent glass ceramics containing NaYF4:Yb^{3+}/Er^{3+} nanocrystals. *J. Alloys Compd.*, **2014**, *617*, 538–541.

[18] A. Pandey, V.K. Rai, V. Kumar, V. Kumar, H.C. Swart. Upconversion based temperature sensing ability of Er^{3+}-Yb^{3+} codoped $SrWO_4$: an optical heating phosphor. *Sens. Actuators B*, **2015**, *209*, 352–358.

[19] M.K. Mahata, K. Kumar, V.K. Rai. Er^{3+}-Yb^{3+} doped vanadate nanocrystals: a highly sensitive thermographic phosphor and its optical nanoheater behaviour. *Sens. Actuators B*, **2015**, *209*, 775–780.

[20] Z.Y. Zhang, K.T.V. Grattan, A.W. Palmer, V. Fernicola, L. Crovini. Temperature dependence of the YAG: Cr^{3+} fluorescence lifetime over the range 77 to 900 K. *Phys. Rev. B*, **1995**, *51*, 2656.

[21] K.T.V. Grattan, R.K. Selli, A.W. Palmer. Ruby decay-time fluorescence thermometer in a fiber-optic configuration. *Rev. Sci. Instrum*., **1988**, *59*, 1328.

[22] B. Struve, G. Huber. Laser performance of Cr^{3+}:Gd(Sc,Ga) garnet. *J. Appl. Phys*. **1985**, *57*, 45.

[23] P.R. Wamsley, K.L. Bray, J. Lumin. The effect of pressure on the luminescence of Cr^{3+}: YAG. *J. Lumin.*, **1994**, *59*, 11-17.

[24] R. Weissleder. A clearer vision for in vivo imaging. *Nat. Biotechnol.*, **2001**, *19*, 316−317.

[25] K. Welsher, S.P. Sherlock, H.J. Dai. Deep-tissue anatomical imaging of mice using carbon nanotube fluorophores in the second near-infrared window. *Proc. Natl. Acad. Sci. U. S. A.*, **2011**, *108*, 8943− 8948.

[26] B.R. Smith, S.S. Gambhir. Nanomaterials for in vivo imaging. *Chem. Rev*., **2017**, *117*, 901−986.

[27] Y. Dai, D. Yang, D. Yu, C. Cao, Q. Wang, S. Xie, L. Shen, W. Feng, F. Li. Mussel-inspired polydopamine-coated lanthanide nanoparticles for NIR-II/CT dual imaging and photothermal therapy. *ACS Appl. Mater. Interfaces*, **2017**, *9*, 26674−26683.

[28] O.Q. De Clercq, L. I. D. J. Martin, K. Korthout, J. Kusakovskij, H. Vrielinck, D. Poelman. Probing the local structure of the nearinfrared emitting persistent phosphor $LiGa_5O_8$:Cr^{3+}. *J. Mater. Chem. C*, **2017**, *5*, 10861−10868.

[29] S.K. Singh. Red and near infrared persistent luminescence nanoprobes for bioimaging and targeting applications. *RSC Adv*., **2014**, *4*, 58674−58698.

[30] R.C. Weissleder, M.J. Pittet. Imaging in the era of molecular oncology. *Nature*, **2008**, *452*, 580−589.

[31] T. Maldiney, A. Lecointre, B. Viana, A. Bessiere, M. Bessodes, D. Gourier, C. Richard, D. Scherman. Controlling electron trap depth to enhance optical properties of persistent luminescence nanoparticles for in vivo imaging. *J. Am. Chem. Soc*., **2011**, *133*, 11810−11815.

[32] A. Abdukayum, J.T. Chen, Q. Zhao, X.P. Yan. Functional near infrared-emitting Cr^{3+}/Pr^{3+} co-doped zinc gallogermanate persistent luminescent nanoparticles with superlong afterglow for in vivo targeted bioimaging. *J. Am. Chem. Soc.*, **2013**, *135*, 14125−14133.

[33] Y.J. Li, X.P. Yan. Synthesis of functionalized triple-doped zinc gallogermanate nanoparticles with superlong near-infrared persistent luminescence for long-term oral administrated bioimaging. *Nanoscale*, **2016**, *8*, 14965−14970.
[34] B. Zheng, H. Chen, P. Zhao, H. Pan, X. Wu, X. Gong, H. Wang, J. Chang. Persistent luminescent nanocarrier as an accurately tracker in vivo for NIR-remote selectively triggered photothermal therapy. *ACS Appl. Mater. Interfaces*, **2016**, *8*, 21603−21611.
[35] E. Zhao, J.W.Y. Lam, L. Meng, Y. Hong, H. Deng, G. Bai, X. Huang, J. Hao, B.Z. Tang. Poly[(maleic anhydride)-alt-(vinyl acetate)]: A pure oxygenic nonconjugated macromolecule with strong light emission and solvatochromic effect. *Macromolecules*, **2015**, *48*, 64−71.
[36] Z. Yi, X. Li, Z. Xue, X. Liang, W. Lu, H. Peng, H. Liu, S. Zeng, J. Hao. Remarkable NIR enhancement of multifunctional nanoprobes for in vivo trimodal bioimaging and upconversion optical/T2-weighted MRI-guided small tumor diagnosis. *Adv. Funct. Mater*., **2015**, *25*, 7119−7129.
[37] Z. Yi, S. Zeng, W. Lu, H. Wang, L. Rao, H. Liu, J. Hao. Synergistic dual-modality in vivo upconversion luminescence/X-ray imaging and tracking of amine-functionalized $NaYbF_4$:Er nanoprobes. *ACS Appl. Mater. Interfaces*, **2014**, *6*, 3839−3847.
[38] A. Bessiere, S. Jacquart, K. Priolkar, A. Lecointre, B. Viana, D. Gourier. $ZnGa_2O_4:Cr^{3+}$: a new red long-lasting phosphor with high brightness. *Opt. Express*, **2011**, *19*, 10131−10137.
[39] W.B. Dai, Y.F. Lei, S. Ye, E.H. Song, Z. Chen, Q.Y. Zhang. Mesoporous nanoparticles Gd_2O_3@$mSiO_2$/$ZnGa_2O_4:Cr^{3+},Bi^{3+}$ as multifunctional probes for bioimaging. *J. Mater. Chem. B*, **2016**, *4*, 1842−1852.
[40] Y. Li, S. Zhou, Y. Li, K. Sharafudeen, Z. Ma, G. Dong, M. Peng, J. Qiu. Long persistent and photo-stimulated luminescence in Cr^{3+}-doped Zn−Ga−Sn−O phosphors for deep and reproducible tissue. *J. Mater. Chem. C*, **2014**, *2*, 2657−2663.
[41] T. Maldiney, A. Bessiere, J. Seguin, E. Teston, S.K. Sharma, B. Viana, A.J.J. Bos, P. Dorenbos, M. Bessodes, D. Gourier, D. Scherman, C. Richard. The in vivo activation of persistent nanophosphors for optical imaging of vascularization, tumours. *Nat. Mater*., **2014**, *13*, 418−426.
[42] T. Matsuzawa, Y. Aoki, N. Takeuchi, Y. Murayama. A New Long Phosphorescent Phosphor with High Brightness, $SrAl_2O_4:Eu^{2+},Dy^{3+}$. *J. Electrochem. Soc*., **1996**, *143*, 2670.
[43] R. Weissleder, M.J. Pittet. Imaging in the era of molecular oncology. *Nature*, **2008**, *452*, 580.
[44] T. Maldiney, A. Bessière, J. Seguin, E. Teston, S.K. Sharma, B. Viana, C. Richard. The *in vivo* activation of persistent nanophosphors for optical imaging of vascularization, tumours and grafted cells. *Nat. Mater*., **2014**, *13*, 418.
[45] C. Boyer, M.R. Whittaker, V. Bulmus, J. Liu, T.P. Davis. The design and utility of polymer-stabilized iron-oxide nanoparticles for nanomedicine applications. *NPG Asia Mater*., **2010**, *2*, 23.
[46] Y. Liu, D. Tu, H. Zhu, X. Chen. Lanthanide-doped luminescent nanoprobes: controlled synthesis, optical spectroscopy, and bioapplications. *Chem. Soc. Rev*., **2013**, *42*, 6924.
[47] Y. Li, S. Zhou, Y. Li, K. Sharafudeen, Z. Ma, G. Dong, J. Qiu. Long persistent and photo-stimulated luminescence in Cr^{3+}-doped Zn–Ga–Sn–O phosphors for deep and reproducible tissue imaging. *J. Mater. Chem. C*, **2014**, *2*, 2657.
[48] T. Paik, T.R. Gordon, A.M. Prantner, H. Yun, C.B. Murray. Designing tripodal and triangular gadolinium oxide nanoplates and self-assembled nanofibrils as potential multimodal bioimaging probes. *ACS Nano*, **2013**, 7, 2850.
[49] R.Weissleder, C.H.Tung, U.Mahmood, A.Bogdanov. In vivo imaging of tumors with protease-activated near-infrared fluorescent probes. *Nat. Biotechnol*., **1999**, *17*, 375.
[50] J. Ueda, K. Kuroishi, S. Tanabe. Bright persistent ceramic phosphors of Ce^{3+}-Cr^{3+}-codoped garnet able to store by blue light. *Appl. Phys. Lett.*, **2014**, *104*, 101904.
[51] Z.Y. Zhang, K.T.V. Grattan, A.W. Palmer. Temperature dependences of fluorescence lifetimes in Cr^{3+}-doped insulating crystals. *Phys. Rev. B*, **1993**, *48*, 7772–7778.
[52] Y.L. Hu, Z.Y. Zhang, K.T.V. Grattan, A.W. Palmer, B.T. Meggitt. Ruby-based decay-time thermometry: effect of probe size on extended measurement range (77–800K). *Sens. Actuators A*, **1997**, *63*, 85–90.
[53] W.H. Fonger, C.W. Struck, Temperature dependences of Cr^{3+} radiative and nonradiative transitions in ruby and emerald. *Phys. Rev. B*, **1975**, *11*, 3251.
[54] E. Broussell, L. Fortina, S. Kulyuk, A. Popov, R. Anedda, Corpino. *J. Appl. Phys*., **1998**, *84*, 531.
[55] M. Yamaga, P.I. Macfarlane, B.K. Holliday, K. Henderson, Y. Inoue. A study of exchange interaction in-doped. *J. Phys. Condens. Matter*, **1997**, *9*, 1575.
[56] T. Ohtake, N. Sonoyama, T. Sakata. Electrochemical luminescence of $ZnGa_2O_4$ semiconductor electrodes activated with Cr and Co. *Chem. Phys. Lett*., **2000**, *318*, 517.
[57] W. Ryba-Romanowski, S. Gołab, W.A. Pisarski, G. Dominiak-Dzik, M.N. Palatnikov, N.V. Sidorov, V.T. Kalinnikov. Influence of temperature on the optical properties of $LiTaO_3$:Cr. *Appl. Phys. Lett*., **1997,** *70*, 2505.
[58] A. Abdukayum, J.T. Chen, Q. Zhao, X.P. Yan. Functional Near Infrared-Emitting Cr^{3+}/Pr^{3+} Co-Doped Zinc Gallogermanate Persistent Luminescent Nanoparticles with Superlong Afterglow for *in Vivo* Targeted Bioimaging. *J. Am. Chem. Soc*., **2013**, *135*, 14125.
[59] Z. Pan, Y.Y. Lu, F. Liu. Sunlight-activated long-persistent luminescence in the near-infrared from Cr^{3+}-doped zinc gallogermanates. *Nat. Mater*., **2012**, *11*, 58.
[60] Y. Li, S. Zhou, Y. Li, K. Sharafudeen, Z. Ma, G. Dong, J. Qiu. Long persistent and photo-stimulated luminescence in Cr^{3+}-doped Zn–Ga–Sn–O phosphors for deep and reproducible tissue imaging. *J. Mater. Chem. C*, **2014**, *2*, 2657.

[61] H. Saalfeld, H. Jagodzinski. Kationenverteilung und Strukturbeziehungen in Mg-Al-Spinellen. *Z. Kristallogr*., **1958**, *110*, 197.
[62] D.L. Wood, G.F. Imbush, R.M. MacFarlane, P. Kisiiuk, D.M. Larkin. Optical spectrum of Cr3+ ions in spinels. *J. Chem. Phys*., **1968**, *48*, 5255.
[63] H. Van den Boom, A.J.J. Van Dijsseidonk, J.C.M. Henning. Determination of exchange parameters of Cr^{3+} pairs in $MgAl_2O_4$ by optical measurements. *J. Chem. Phys*., **1977**, *66*, 2368.
[64] W. Mikenda, A. Preisinger, J. Lumin. N-lines in the luminescence spectra of Cr^{3+}-doped spinels (I) identification of N-lines. *J. Lumin.*, **1981**, *26*, 53.
[65] J.C.M. Henning, H. Van den Boom. ESR Investigations of Nearest-Neighbor Cr^{3+}-Cr^{3+} Interactions in Cr-Doped Spinel $MgAl_2O_4$. *Phys. Rev. B*, **1973**, *8*, 2255.
[66] J. Yang, Y. Liu, D. Yan, H. Zhu, C. Liu, C. Xu, L. Ma, X. Wang. A vacuum-annealing strategy for improving near-infrared super long Crystal Growth & Design. *Cryst. Growth Des*., **2018**, *18*, 3178−3186.
[67] F. Liu, W. Yan, Y.J. Chuang, Z. Zhen, J. Xie, Z. Pan. Photostimulated near-infrared persistent luminescence as a new optical read-out from Cr^{3+}-doped $LiGa_5O_8$. *Sci. Rep*., **2013**, *3*, 1554−1562.
[68] V. Singh, R.P.S. Chakradhar, J.L. Rao, J.-J. Zhu. Studies on red-emitting Cr^{3+} doped barium aluminate phosphor obtained by combustion process. *Mater. Chem. Phys.*, **2008**, *111*, 143–148.
[69] Y.B. Band. *Light and Matter*, Wiley, **2006**.
[70] R. Martín-Rodríguez, R. Valiente, F. Rodríguez, M. Bettinelli. Temperature and pressure dependence of the optical properties of Cr^{3+}-doped $Gd_3Ga_5O_{12}$ nanoparticles. *Nanotechnology*, **2011**, *22*, 265707.
[71] M.N. Sanz-Ortiz, F. Rodríguez, I. Hernández, R. Valiente, S. Kück. Origin of the $^2E \leftrightarrow {}^4T_2$ Fano resonance in Cr^{3+}-doped $LiCaAlF_6$: pressure-induced excited-state crossover *Phys. Rev. B*, **2010**, *81***,** 045114.
[72] Y.R. Shen, K.L. Bray. Effectofpressureand temperature on the lifetime of Cr^{3+} in yttrium aluminum garnet *Phys. Rev. B*, **1997**, *56***,** 10882–91.
[73] B. Henderson, G.F. Imbusch. *Optical Spectroscopy of Inorganic Solids*. Oxford University Press, **1989**.
[74] C.D.S. Brites, P.P. Lima, N.J.O.. Silva, A. Millan, V.S. Amaral, F. Palacio, L.D. Carlos. Thermometry at the Nanoscale. *Nanoscale*, **2012**, *4*, 4799−4829.
[75] E.J. McLaurin, L.R. Bradshaw, D.R. Gamelin. Dual-Emitting Nanoscale Temperature Sensors. *Chem. Mater*., **2013**, *25*, 1283−1292.
[76] L.H. Fischer, G.H. Harms, O.S. Wolfbeis. Upconverting Nanoparticles for Nanoscale Thermometry. *Angew. Chem., Int. Ed.*, **2011**, *50*, 4546−4551.
[77] D. Jaque, F. Vetrone. Luminescence Nanothermometry. *Nanoscale*, **2012**, *4*, 4301−4326.
[78] E.C. Ximendes, W.Q. Santos, U. Rocha, U.K. Kagola, F. SanzRodríguez, N. Fernandez, A.S. Gouveia-Neto, D. Bravo, A.M. Domingo, B. del Rosal, C.D.S. Brites, L.D. Carlos, D. Jaque, C. Jacinto. Unveiling in Vivo Subcutaneous Thermal Dynamics by Infrared Luminescent Nanothermometers. *Nano Lett*., **2016**, *16*, 1695− 1703.
[79] J. Ueda, M. Back, M.G. Brik, Y. Zhuang, M. Grinberg, S. Tanabe. Ratiometric optical thermometry using deep red luminescence from $^4T2$ and ^2E states of Cr^{3+} in $ZnGa_2O_4$ host. *Opt. Mater.*, **2018**, *85*, 510–516.
[80] M. Back, E. Trave, J. Ueda, S. Tanabe. Ratiometric Optical Thermometer Based on Dual Near-Infrared Emission in Cr^{3+}-Doped Bismuth-Based Gallate Host*. Chem. Mater.,* **2016**, *28*, 8347-8356.
[81] M. Back, E. Casagrande, C.A. Brondin, E. Ambrosi, D. Cristofori, J. Ueda, S. Tanabe, E. Trave, P. Riello. Lanthanide-Doped Bi_2SiO_5@SiO_2 Core-Shell Upconverting Nanoparticles for Stable Ratiometric Optical Thermometry. *ACS Appl. Nano Mater., **2020**, 3*, 2594-2604.
[82] E. Casagrande, M. Back, D. Cristofori, J. Ueda, S. Tanabe, S. Palazzolo, F. Rizzolio, V. Canzonieri, E. Trave, P. Riello. Upconversion-mediated Boltzmann thermometry in double-layered Bi_2SiO_5:Yb^{3+},Tm^{3+}@SiO_2 hollow nanoparticles. *J. Mater. Chem. C, **2020**, 8*, 7828-7836.
[83] M. Back, J. Ueda, H. Nambu, M. Fujita, A. Yamamoto, H. Yoshida, H. Tanaka, M.G. Brik, S. Tanabe. Boltzmann Thermometry in Cr^{3+}-Doped Ga_2O_3 Polymorphs: The Structure Matters!. *Adv. Optical Mater*., **2021**, 2100033.
[84] M. Back, J. Ueda, J. Xu, K. Asami, M.G. Brik, S.Tanabe. Effective Ratiometric Luminescent Thermal Sensor by Cr^{3+}-Doped Mullite $Bi_2Al_4O_9$ with Robust and Reliable Performances. *Adv. Optical Mater*., **2020**, *8*, 2000124.
[85] M. Back, J. Ueda, M.G. Brik, T. Lesniewski, M. Grinberg, S. Tanabe. Revisiting Cr^{3+}-Doped $Bi_2Ga_4O_9$ Spectroscopy: Crystal Field Effect and Optical Thermometric Behavior of Near-Infrared-Emitting Singly-Activated Phosphors. *ACS Appl. Mater. Interfaces*, **2018,** *10*, 41512-41524.
[86] M. Back, J. Ueda, M.G. Brik, S.Tanabe. Pushing the Limit of Boltzmann Distribution in Cr^{3+}-Doped $CaHfO_3$ for Cryogenic Thermometry. *ACS Appl. Mater. Interfaces*, **2020,** *12*, 38325-38332.
[87] E. Ejder. Methods of Representing Emission, Excitation, and Photoconductivity Spectra. *J. Opt. Soc. Am.* **1969**, *59*, 223−224.
[88] W. Stöber, A. Fink, E. Bohn. Controlled growth of monodisperse silica spheres in the micron size range. *J. Colloid Interface Sci*., **1968**, *26*, 62-69.
[89] Y. Shi, M. L. Miller, A. J. Di Pasqua. Biocompatibility of mesoporous silica nanoparticles?. *Comments Inorg. Chem.,* **2016**, *36*, 61-80.
[90] L. Ding, B. Su. An electrochemistry assisted approach for fast, low-cost and gram-scale synthesis of mesoporous silica nanoparticles. *RSC Adv.*, **2015**, *5,* 65922-65926.
[91] Z. Hou, C. Li, P. Ma, Z. Cheng, X. Li, X. Zhang, Y. Dai, D. Yang, H. Lian, J. Lin. Up-conversion luminescent and porous $NaYF_4$:Yb^{3+}, Er^{3+}@SiO_2 nanocomposite fibers for anti-cancer drug delivery and cell imaging. *Adv. Funct. Mater*., **2012**, *22*, 2713.
[92]: Y. Wang, Q. Zhao, N. Han, L. Bai, J. Li, J. Liu, E. Che, L. Hu, Q. Zhang, T. Jiang. Mesoporous silica nanoparticles in drug delivery and biomedical applications. *Nanomed. Nanotechnol. Biol. Med*., **2015**, *11*, 313-327.

[93] F. Jiao, H. Frei. Nanostructured cobalt oxide clusters in mesoporous silica as efficient oxygen-evolving catalysts. *Angew. Chem., Int. Ed*., **2009**, *48*, 1841.
[94] M. Jang, J. K. Park, E. W. Shin. Lanthanum functionalized highly ordered mesoporous media: implications of arsenate removal. *Micropor.. Mesopor. Mat.,* **2004**, *75*, 159-168.
[95] J. Kim, J. E. Lee, J. Lee, J. H. Yu, B. C. Kim, K. An, Y. Hwang, C. Shin, J. Park, J. Kim, T. Hyeon. Magnetic fluorescent delivery vehicle using uniform mesoporous silica spheres embedded with monodisperse magnetic and semiconductor nanocrystals. *J. Am. Chem. Soc*., **2006**, *128*, 688-689.
[96] R. Narayan, U. Y. Nayak, A. M. Raichur, S. Garg. Mesoporous silica nanoparticles: a comprehensive review on synthesis and recent advances. *Pharmaceutics, **2018**, 10,* 118*.*
[97] M. Grün, I. Lauer, K. K. Unger. The synthesis of micrometer- and submicrometer-size spheres of ordered mesoporous oxide MCM-41. *Adv. Mater*., **1997**, *9*, 254-257.
[98] Z. A. Qiao, L. Zhang, M. Guo, Y. Liu, Q. Huo. Synthesis of mesoporous silica nanoparticles via controlled hydrolysis and condensation of silicon alkoxide*. Chem. Mater*., **2009**, *21*, 3823-3829.
[99] S. Wu, C. Mou, H.P. Lin. Synthesis of mesoporous silica nanoparticles. *Chem. Soc. Rev.,* **2013**, *42*, 3862.
[100] J. Kim, J. E. Lee, J. Lee, J. H. Yu, B.C. Kim, K. An, Y. Hwang, C. Shin, J. Park, J. Kim, T. Hyeon. Magnetic fluorescent delivery vehicle using uniform mesoporous silica spheres embedded with monodisperse magnetic and semiconductor nanocrystals. *J. Am. Chem. Soc*., **2006**, *128*, 688-689.
[101] L. Sierra, B. Lopez J. L. Guth. Preparation of mesoporous silica particles with controlled morphology from sodium silicate solutions and a non-ionic surfactant at pH values between 2 and 6. *Micropor. Mesopor. Mater*., **2000***, 39*, 519-527.
[102] L. Han, C. Gao, X. Wu, Q. Chen, P. Shu, Z. Ding, S. Che. Anionic surfactants templating route for synthesizing silica hollow spheres with different shell porosity. *Solid State Sci.,* **2011**, *13*, 721-728.
[103] Z. Gao, I. Zharov. Large pore mesoporous silica nanoparticles by templating with a nonsurfactant molecule, tannic acid. *Chem. Mater.,* **2014**, *26*, 2030-2037.
[104] Y. Han, J.Y. Ying. Generalized fluorocarbon-surfactant-mediated synthesis of nanoparticles with various mesoporous structures. *Angew. Chem. Int. Ed.,* **2005**, *44*, 288-292.
[105] D. Zhao, J. Feng, Q. Huo, N. Melosh, G.H. Fredrickson, B.F. Chmelka, G.D. Stucky, triblock copolymer syntheses of mesoporous silica with periodic 50 to 300 angstrom pores, *Science,* **1998**, *279*, 548-552.
[106] F. Kleitz, D. Liu, M. A. Gopinathan, I.S. Park, L.A. Solovyov, A.N. Shmakov, R. Ryoo. Large cage face-centered-cubic *Fm3m* mesoporous silica: synthesis and structure. *J. Phys. Chem. B,* **2003**, *107*, 14296-14300.
[107] S. Penner, C. Zhuo, R. Thalinger, M. Grünbacher, C. Hejny, S. Vanicek, M. Noisternig. Physico-chemical properties of unusual Ga_2O_3 polymorphs. *Monatsh Chem*, **2016**, *300*, 147-289.
[108] S.C. Vanithakumari, K.K. Nanda. A One-Step Method for the Growth of Ga_2O_3-Nanorod-Based White-Light-Emitting Phosphors. *AdV. Mater*., **2009**, *21*, 3581-3584.
[109] S.P. Arnold, S.M. Prokes, F.K. Perkins, M.E. Zaghloul. Design and performance of a simple, room-temperature Ga_2O_3 nanowire gas sensor. *Appl. Phys. Lett*., **2009**, *95*, 103102.
[110] V.I. Nikolaev, A.V. Chikiryaka, L.I. Guzilova, A.I. Pechnikov. Microhardness and Crack Resistance of Gallium Oxide. *Tech. Phys. Lett.*, **2019**, *45*, 1114-1117.
[111] S.-D. Guo, H.-M. Du. Piezoelectric properties of Ga_2O_3: a first-principle study. *Eur. Phys. J. B*, **2020**, *93*, 7.
[112] G.D. Meitzner, E. Iglesia, J.E. Baumgartner, E.S. Huang. The Chemical State of Gallium in Working Alkane Dehydrocyclodimerization Catalysts. In situ Gallium K-Edge X-Ray Absorption Spectroscopy. *J. Cat.*, **1993**, *140*, 209-225.
[113] H. Yang, R. Shi, J. Yu, R. Liu, R. Zhang, H. Zhao, L. Zhang, H. Zheng. Surface Structures of Black Phosphorus Investigated with Scanning Tunneling Microscopy. *J. Phys. Chem. C*, **2009**, *113*, 21548.
[114-A] H.Y. Playford, A.C. Hannon, E.R. Barney, R.I. Walton. Structures of uncharacterised polymorphs of gallium oxide from total neutron diffraction. *Chem. Eur. J.*, **2013**, *19*, 2803.
[114-B] H.Y. Playford, A.C. Hannon, M.G. Tucker, D.M. Dawson, S.E. Ashbrook, R.J. Kastiban, J. Sloan, R.I. Walton. Characterization of Structural Disorder in γ-Ga2O3. *J. Phys. Chem. C*, **2014**, *118*, 16188−16198.
[115] R. Roy, V.G. Hill, E.F. Osborn. Polymorphism of Ga_2O_3 and the System Ga_2O_3-H_2O. *J. Am. Chem. Soc.*, **1952**, *74*, 719–722.
[116] K. Momma and F. Izumi. VESTA 3 for three-dimensional visualization of crystal, volumetric and morphology data. *J. Appl. Crystallogr*., **2011**, *44*, 1272-1276.
[117] B.A. Prakasam, M. Lahtinen, M. Muruganandham, M. Sillanpää. Synthesis of self-assembled α-GaOOH microrods and 3D hierarchical architectures with flower like morphology and their conversion to α-Ga_2O_3. *Mater. Lett.*, **2015**, *158*, 370–372.
[118] M. Zinkevich, F. Aldinger. Thermodynamic Assessment of the Gallium-Oxygen System. *J. Am. Ceram. Soc*. **2004**, *87*, 683–691.
[119] A. Segura, L. Artus, R. Cuscò, R. Goldhahn, M. Feneberg. Band gap of corundumlike α-Ga_2O_3 determined by absorption and ellipsometry. *Phys. Rev. Mater.*, **2017**, *1*, 024604.
[120] A.V. Rodrigues, N.L. Sabino. Synthesis of photoluminescent β-Ga_2O_3 nanostructures using electrospinning method, and control of length-diameter ratio by calcination heating rates. *J. Mater. Sci. Mater. Electron.*, **2019**, *30*, 16910–16916.
[121] K. Sasaki, M. Higashiwaki, A. Kuramata, T. Masui, S. Yamakoshi. MBE grown Ga_2O_3 and its power device applications. *J. Cryst. Growth*, **2013**, *378*, 591–595.
[122] S.S. Farvid, T. Wang, P.V. Radovanovic. Colloidal Gallium Indium Oxide Nanocrystals: A Multifunctional Light-Emitting Phosphor Broadly Tunable by Alloy Composition. *J. Am. Chem. Soc.*, **2011**, *133*, 6711–6719.

[123] D.S. Cook, R.J. Kashtiban, K. Krambrock, G.M. De Lima, H.O. Stumpf, L.R.S. Lara, J.D. Ardisson, R.I. Walton. Nanocrystalline transition-metal gallium oxide spinels from acetylacetonate precursors via solvothermal synthesis. *Materials*, **2019**, *12*, 838.
[124] T. Wang, S.S. Farvid, M. Abulikemu, P.V. Radovanovic. Size-Tunable Phosphorescence in Colloidal Metastable γ-Ga2O3 Nanocrystals. *J. Am. Chem. Soc*., **2010**, *132*, 9250–9252.
[125] G. Paglia. *Determination of the Structure of γ-Alumina using Empirical and First Principles Calculations Combined with Supporting Experiments*. Curtin University of Technology, Perth, **2004**.
[126] T. Oshima, T. Okuno, N. Arai, Y. Kobayashi, S. Fujita. β-$Al_{2x}Ga_{2-2x}O_3$ Thin Film Growth by Molecular Beam Epitaxy. *Jpn. J. Appl. Phys*., **2009**, *48*, 070202.
[127] V.G. Hill, R. Roy, E.F. Osborn. The System Alumina-Gallia-Water. *J. Am. Ceram. Soc*., **1952**, *35*, 135-142.
[128] H. Ito, K. Kaneko, S. Fujita. Growth and Band Gap Control of Corundum-Structured α-$(AlGa)_2O_3$ Thin Films on Sapphire by Spray-Assisted Mist Chemical Vapor Deposition. *Jpn. J. Appl. Phys*., **2012**, *51*, 100207
[129] H. Woo, K. Hyunseok, K. Yong-Chae, C. Sung, B. Cho. Heterostructural phase diagram of Ga_2O_3–based solid solution with Al_2O_3. *Eur. J. Chem.*, **2021**, *41*, 611-616.
[130] S. Ma, Y. Wang, Y. Zhu. A simple room temperature synthesis of mesoporous silica nanoparticles for drug storage and pressure pulsed delivery. *J. Porous. Mater.*, **2011**, *18*, 233–239.
[131] D. Zhao, Q. Huo, J.Feng, B.F. Chmelka, G.D. Stucky. Nonionic Triblock and Star Diblock Copolymer and Oligomeric Surfactant Syntheses of Highly Ordered, Hydrothermally Stable, Mesoporous Silica Structures. *J. Am. Chem. Soc*., **1998**, *120*, 6024-6036.
[132] L. Cao, T. Man, M. Kruk; Synthesis of Ultra-Large-Pore SBA-15 Silica with Two-Dimensional Hexagonal Structure Using Triisopropylbenzene As Micelle Expander. *Chem. Mater.*, **2009**, *21*, 1144–1153.
[133] S. Sugano, Y. Tanabe. Absorption Spectra of Cr^{3+} in Al_2O_3, Part A. Theoretical Studies of the Absorption Bands and Lines. *J. Phys. Soc. Jpn.*, **1958**, *13*, 880–899.
[134] D. M. Dodd, D. L. Wood, R. L. Barns. Spectrophotometric Determination of Chromium Concentration in Ruby. *J. Appl. Phys.*, **1964**, *35*, 1183–1186.
[135] C.P. Poole Jr.. The Optical Spectra and Color of Chromium Containing Solids. *J. Phys. Chem. Solids*, **1964**, *25*, 1169–1182.
[136] F. Rouquerol, J. Rouquerol, K. Sing. *Adsorption by powder & porous solids: Principles, methodology and applications*. Academic Press, London, **1999**.
[137] O. Kazuyoshi, A. Fatimah, N. Hikari. Multiplet Energy Level Diagrams for Cr^{3+} and Mn^{4+} in Oxides with O_h Site Symmetry Based on First-Principles Calculations. *ECS J. Solid State Sci. Technol.*, **2016**, *10*, 1149.
[138] T.T. Loan, N.A. Bang, V.H. Huong, N.N. Long. Effect of Cr^{3+} concentration on structural and optical properties of TiO_2:Cr^{3+} anatase and rutile phases. *Opt. Mater.*, **2017**, *69*, 30-37.
[139] P.C. Patel, S. Ghosh, P.C. Srivastava. Unusual Ferromagnetic to Paramagnetic Change and Bandgap Shift in ZnS:Cr Nanoparticles. *J. Electron. Mater.*, **2019**, *48*, 7031-7039.
[140] T. Yan, Z.-G. Shen, W.-W. Zhang, J. Chen. Size dependence on the ferroelectric transition of nanosized $BaTiO_3$ particles. *Mater. Chem. Phys.*, **2006**, *98*, 450–455.
[141] Y. Shiratori, A. Magrez, J. Dornseiffer, F.-H. Haegel, C. Pithan, R. Waser. Polymorphism in Micro-, Submicro-, and Nanocrystalline $NaNbO_3$. *J. Phys. Chem. B*, **2005**, *109*, 20122-20130.
[142] W. Li, H. Huang, H. Li, W. Zhang, H. Liu. Facile Synthesis of Pure Monoclinic and Tetragonal Zirconia Nanoparticles and Their Phase Effects on the Behavior of Supported Molybdena Catalysts for Methanol-Selective Oxidation. *Langmuir*, **2008**, *24*, 8358-8366.
[143] A. Anagnostopoulos, A. Alexiadis, Y. Ding. Simplified force field for molecular dynamics simulations of amorphous SiO_2 for solar applications. *Int. J. ther. Sci.*, **2021**, *160*, 106647.
[144] N.K. Kaliannan, K. Krishnamurthy, S.K. Sreerama, A.M. Ronson, J.J. Rathnam. Monte Carlo simulations of bulk and nano amorphous silica (a-SiO_2) melts. *Comput. Mater. Sci.*, **2018**, *146*, 90–101.
[145] Z. Cheng, M. Hanke, Z. Galazka, A. Trampert. Thermal expansion of single-crystalline β-Ga_2O_3 from RT to 1200 K studied by synchrotron-based high resolution x-ray diffraction; *App. Phys. Lett.*, **2018**, *113*, 182102.
[146] M.E. Liao, C. Li, H.M. Yu, E. Rosker, M.J. Tadjer, K.D. Hobart, M.S. Goorsky. Coefficients of thermal expansion of single crystalline β-Ga_2O_3 and in-plane thermal strain calculations of various materials combinations with β-Ga_2O_3. *APL Mater*., **2019**, *7*, 022517.
[147] R.D. Shannon, Revised Effective Ionic Radii and Systematic Studies of Interatomic Distances in Halides and Chalcogenides. *Acta Cryst.*, **1976**, *A32*, 751-767.
[148] J. Ueda, P. Dorenbos, A.J.J. Bos, A. Meijerink, S. Tanabe. Insight into the Thermal Quenching Mechanism for $Y_3Al_5O_{12}$:Ce^{3+} through Thermoluminescence Excitation Spectroscopy. *J. Phys. Chem. C*, **2015**, *119*, 25003−25008.
[149] X. Li, Y. Liu, D. Peng. Suppression of thermal quenching in fast-responding pressure-sensitive paint by restricting lattice relaxation of luminescent molecules. *J. Lumin.*, **2020**, *217*, 116803.